

ADVANCES IN SINTERING OF POWDER METALLURGY STEELS

ADVANCES IN SINTERING OF POWDER METALLURGY STEELS

BY: NILUSHI C. KARIYAWASAM, B.ENG.

A Thesis Submitted to the School of Graduate Studies in Partial Fulfillment of the Requirements
for the Degree: Master of Applied Science

McMaster University © Copyright by Nilushi C. Kariyawasam, August 24 2017

Master of Applied Science (2017) McMaster University
(Materials Science and Engineering) Hamilton, Ontario

TITLE: Advances in Sintering of Powder Metallurgy Steels

AUTHOR: Nilushi C. Kariyawasam, B.Eng., (McMaster University)

SUPERVISOR: Dr. Dmitri V. Malakhov

NUMBER OF PAGES: xiii, 123

Abstract

In comparison to traditionally fabricated steels that can undergo extensive processing to produce a complex-shaped component, the powder metallurgy (PM) technique can provide a more efficient approach as it is capable of producing intricately-shaped components that require little to no additional processing and machining [1], [2]. A key factor in being able to do so pertains to quenching and utilizing an appropriate quenching agent that can provide dimensional stability to the part being quenched [3], [4]. To ensure that a PM component can perform equally well when being quenched by a quenchant of reduced cooling capability, the PM component should be if not more, then just as hardenable. Steel hardenability can inevitably be improved with the increase of overall alloying content [5], however, if overall alloying content is to be kept at a minimum, the concept of lean PM steel design is one worth investigating; where a lean steel entails that each and every alloying addition is utilized to its maximum potential.

This study evaluates the homogenization behaviour of alloying elements in PM steels during sintering as well as the efficiency of wide-spread industrial practices involving the use of various master alloys and ferroalloys, and investigates the realm of liquid phase sintering to understand and optimize the homogenization behaviour of alloying elements and mechanical properties of PM steels. In the context of this work, multi-component master alloys contain at least three of non-ferrous metals as alloying elements and ferroalloys are master alloys containing iron in addition to typically a maximum of two other non-ferrous alloying additions.

Part one of this study discusses a combination of thermodynamic software (DICTRA and Thermo-Calc), incremental sintering experiments and scanning electron microscopy (SEM) - wavelength dispersive spectroscopy (WDS) that were used in order to form a deeper understanding of the homogenization behaviour of alloying elements within PM steel during sintering. Electron microscopy analyses on partially and industrially sintered components provide elemental maps to track the evolution of alloying elements as they relax to homogeneity. Electron microscopy analyses for this portion of the study were conducted on an industry-produced automotive component that was sectioned and sintered industrially as well as experimentally at 1280°C for 30 minutes and 13.4 hours.

DICTRA simulations carried out for this research provide a 1-D insight into the evolution of concentration profiles and phases throughout various sintering times for systems involving Cr, Mn, C and Fe. DICTRA simulation results of alloying sources were studied alongside alloying element profiles obtained by compiling point quantification from wavelength dispersive spectroscopy maps for the sintered automotive component. Computational results provided conservative, semi-quantitative recommendations on optimal alloy addition forms that lead to an improvement in homogenization.

Part two of this study involves the approach of fabricating and testing multi-component master alloy additions. As these materials are widely employed in PM and are typically fabricated by solidification, their states are non-equilibrium and therefore have regions containing phases precipitating in the beginning of freezing which have higher melting temperatures than regions with phases forming later on. During heating, it is hypothesized that Scheil's solidification path backtracks and as a result, a fraction of liquid in the ferroalloy can be estimated at sintering temperature. If the fraction is significant, the utilization of this ferroalloy implies liquid phase sintering. Through a combination of Thermo-Calc and Fortran softwares, multi-component ferroalloys with promising compositions were discovered in Fe-C-Cr-Mn, Fe-C-Cr-Mn-Ni, Fe-C-Mn-Mo, Fe-C-Mn-Mo-Ni and Fe-C-Cr-Mn-Mo-Ni systems for low temperature liquid phase sintering. Those of the Fe-C-Cr-Mn-Mo, Fe-C-Cr-Mn-Mo-Ni and Fe-Mn-Mo-Ni system were fabricated and tried in practice. Compositional maps and mechanical properties of PM steels made with variations of this specially tailored multi-component master alloys were compared with those for which traditional alloy additions were used.

Acknowledgements

This thesis acknowledges the engineering community immersed in the realm of powder metallurgy and each individual that I have crossed paths with on my two-year journey throughout this master's degree.

Firstly I must thank my supervisor Dr. Dmitri V. Malakhov; who opened the door to this research opportunity for me. Thank you for your remarkable insight, patience and curiosity which undoubtedly shaped the discoveries made in this investigation. What I have learnt from our collaboration extends far beyond the field of powder metallurgy and has enabled me to become much more than a better researcher.

To my industry contact Roger Lawcock and colleagues at Stackpole International and Western University (EPMA Lab), thank you for your insights and cordial efforts in assisting with experiments and analyses. It was a pleasure to work and share this research opportunity with all of you.

To my family and husband Franklyn. I am eternally grateful for your endless love, support and encouragement. For all of the kind, confident gestures and words that you'd effortlessly share when I needed it the most; you have been a tremendous source in helping me move forward in my work.

To all of the wonderful individuals and friends that I have met and have supported me throughout my time a graduate student; within Hamilton and in Turkey; thank you for being an essential part of my journey.

To the GTA-Hamilton community of salsaeros and bachateros, thank you for never failing to provide such unparalleled inspiration and energy in so many much-needed times - something for which words cannot truly express but only dance.

Finally, to my many mentors that I would not have otherwise met or grown to know so early on in my life if it wasn't for working through to this point of this 2-year master's degree:

Les Brown | Anthony Robbins | Robin Sharma | Hal Elrod | Grant Cardone | Tim Bilyeu | Joel Osteen | Marie Forleo | Lewis Howes | Conor McGregor | Gerry Robert | Jack Ma | Lisa Nichols |

Without the passion, service and work you all have shared with myself and the rest of the world, the completion of this thesis would not have been possible from my end. Thank you for opening my eyes and thoughts to the endless potential and possibilities that exist within this world and in the human mind.

This research was undertaken with the financial support of Stackpole International and the Ontario Centre of Excellence to whom special thanks are accorded.

Table of Contents

Part I: Introduction to Powder Metallurgy (PM) and PM Design.....	1
Chapter 1: Literature Review.....	1
Introduction to PM.....	1
Brief History.....	2
PM Process Summary.....	2
Powder Metal Production.....	3
Powder Mixing.....	4
Alloying Element Additions.....	5
PM Steel Porosity and Effect on Properties.....	7
Compaction.....	9
Sintering.....	10
Diffusion During Sintering Processes.....	12
Major Mass Transport and Sintering Phenomena.....	16
Importance of Wettability and Solubility for Alloy Design.....	20
Master Alloy Design and The Scheil-Gulliver Paradigm.....	23
Electron Microscopy.....	25
Computational Thermodynamics and Previous Work.....	28
Previous Experimental Work.....	30
Chapter 2: Scope and Objectives.....	33
Part II: An Experimental and Computational Approach to Understanding the Homogenization Behaviour of Alloying Elements During the Sintering of PM Steel.....	35
Chapter 3: Sintering Experiments.....	36
Sintering Experiments.....	36
Chapter 4: Electron Microscopy: EDS and WDS Investigations.....	38
Chapter 5: DICTRA Simulations.....	43
Simulation for sintering Cr Master Alloy (Cr MA).....	47
Simulation for Sintering Mn Master Alloy (Mn MA).....	49
Simulation for Sintering Cr in Pure vs. Master Alloy (MA) Form.....	52
Simulation for Sintering Multi-component Sources.....	53
Part III: Multi-Component Master Alloys for Low-Temperature Liquid Phase Sintering.....	58
Chapter 6: Computational Algorithm for Selection of Multi-Component Master Alloys for Liquid Phase Sintering (LPS).....	58
Master alloys: equilibrium and as-solidified states.....	58

Example 1: Cr-rich master alloy	59
Example 2: Mn-rich master alloy.....	60
Development of partially or fully melted multi-component master alloys	62
Thermo-Calc and Fortran Algorithm	62
Selection Criterion and Results.....	65
Chapter 7: Powder and Test Bar Fabrication	71
Powder Production.....	71
Calorimetric examination.....	73
Test Bar Fabrication.....	75
Chapter 8: Characterization by Microscopy	76
Scanning Electron Microscopy (SEM) - Wavelength Dispersive X-Ray Spectroscopy (WDS)	76
Mechanical properties	82
Chapter 9: Additional Master Alloys	83
Characteristics of Additional Master Alloys (M1, M2 and M3).....	83
Calorimetric Examination	85
Overall Compositions for Additional Alloy Blends.....	89
Electron Microscopy - WDS Maps and Quantification.....	91
Mechanical Properties.....	104
Chapter 10: Conclusions and Future Work.....	106
References.....	108
Appendix A: DICTRA	111
Appendix B: Thermo-Calc Diffusivities.....	120

List of Figures

Figure 1: Powder Metal Processing Route Summary	3
Figure 2: Ideal Diameter (D.I.) as a Function of Carbon Content and ASTM Grain Size[5]	6
Figure 3: D.I. Multiplying Factor of Various Alloying Elements [5]	6
Figure 4: Effect of PM Density on Various Properties	8
Figure 5: Porosity for a 7.0 g/cc sintered PM steel	8
Figure 6: Common Compaction Methods[3]	10
Figure 7: Continuous Sintering Furnace With 5 Zones: I) Dewaxing, II) Preheating, III) Heating, IV) Precooling, V) Final Cooling [3]	11
Figure 8a) Diffusion Occurring In Same Direction As Concentration Gradient and b) Against Concentration Gradient [17]	13
Figure 9: Schematic of Grain boundary Diffusion (J_g : flux due to grain boundary diffusion, J_l : flux due to lattice diffusion)	17
Figure 10: Surface Transport Mechanisms (E-C: Evaporation-Condensation, SD: Surface Diffusion, VD: Volume Diffusion [4])	18
Figure 11: Bulk Transport Mechanisms (PF: Plastic Flow, GB: Grain Boundary Diffusion, VD: Volume Diffusion [4], X: width of neck, D: particle diameter, ΔL : <i>change in particle diameter</i>)	18
Figure 12: Liquid Phase Sintering (LPS) Phenomena Depicting Melting and Redistribution of Grains By Melting of "Master Alloy" Particles [3]	19
Figure 13: Wettability Schematic (γ_{sv} : solid surface free energy, γ_{sl} : solid/liquid interfacial free energy, γ_{lv} : liquid surface free energy, θ : contact angle)[31]	21
Figure 14: Contact angle evolution for a Cu alloy on an Fe substrate in a reducing (N_2-10H_2) and inert (Ar) Atmosphere [32]	22
Figure 15: Contact angle evolution for an Fe-Mn-Si alloy on an Fe substrate in a reducing (N_2-10H_2) and inert (Ar) Atmosphere [32]	22
Figure 16: Cu LPS-Activating Alloy (Low-Dissolutive)[33]	23
Figure 17: Ni-4Cu-12Si LPS-Activating Alloy (High-Dissolutive) [33]	23
Figure 18: Solidification ranges for Equilibrium and Scheil-Gulliver Solidification For Composition X_{o24}	
Figure 19: Scheil Solidification Schematic	25
Figure 20: a) Signals given off in an Electron Microscope [39]and b) Sample Interaction Volume	26
Figure 21: X-Ray refraction with Analytical Crystal[41], (S_o and S_1 : incoming and diffracted X-rays respectively)	27
Figure 22: Rowland Circle With Specimen, Analytical Crystal and Detector [39] (S_o and S_1 : incoming and diffracted X-rays respectively, \emptyset : take-off angle of X-rays)	28
Figure 23: General MA-Fe System Schematic Set-Up for DICTRA Simulation [34]	29
Figure 24: Fe-MA DICTRA System Set-Up to Study Diffusion of Mn from Fe-40wt%Mn-10wt%Si-1wt%C Master Alloy into FCC Iron [44]	29
Figure 25: Analysis of Improving Cr, Si and Ni Homogeneity By Increasing Sintering Temperature - Detected by EDS [49]	31
Figure 26: a) Low Dissolutive Master Alloy Behaviour and b) High Dissolutive Master Alloy Behaviour[51]	32
Figure 27: Experimental Summary	37
Figure 28: SEM of PM Green Body (Example 1)	38

Figure 29: SEM of PM Green Body (Example 2).....	38
Figure 30: BSE and WDS elemental maps of industrial automotive component (Large grains outlined by white boxes).....	40
Figure 31: a) Cr Profiles obtained from DICTRA and (b) WDS Point Quantification	48
Figure 32: Mn Profiles obtained from DICTRA and (b) WDS Point Quantification	50
Figure 33: Cr Profiles from (a) Pure Cr FeC and (b) Cr MA Fe DICTRA Simulation (all time values are in seconds and sintering T = 1280°C). Simulation details: (c) Pure Cr FeC DICTRA set-up (d) Cr MA Fe DICTRA set-up.....	52
Figure 34: Composition Details for DICTRA Simulation of Cr,Mn MA FeC Cr, Mn MA.....	53
Figure 35: Composition Details for DICTRA Simulation of Cr MA FeC Mn MA	53
Figure 36: Compositions after being sintered for 30 minutes at 1280°C for a) MMA and b) SMAs sandwiching an Fe-C particle.....	54
Figure 37: Compositions after being sintered for 2.5 hours at 1280°C for a) MMA and b) SMAs sandwiching an Fe-C particle.....	55
Figure 38: Compositions after being sintered for 13.4 hours at 1280°C for a) MMA and b) SMAs sandwiching an FeC particle.....	56
Figure 39: Solidification Path of the Fe-61 wt% Cr - 8.7 wt% C melt	60
Figure 40: Solidification path of the Fe-76wt% Mn 6.8wt% C melt	61
Figure 41: Schematic for Thermo-Calc - Fortran Program.....	62
Figure 42: MMA Powder Production: a) arc-melting set-up, b) arc-melted ingot, c) impact-broken ingot, d) particles after preliminary ball milling and e) fine powder after final ball milling	72
Figure 43: NK, 30°C/min.....	73
Figure 44: DM, 30°C/min	74
Figure 45: Sample TRS (Transverse Rupture Strength) PM Test Bar.....	75
Figure 46: BSE Images and WDS Elemental Maps for NK-S and NK-T (Large grains outlined by a white square).....	78
Figure 47: BSE Images and WDS Elemental Maps for DM-S and DM-T (Large grains outlined by a white square).....	79
Figure 48: WDS Point Quantification Plots For NK-S, NK-T, DM-S and DM-T	80
Figure 49: Thermo-Calc Scheil Simulation of M1: 3.5C-52Mn-8Mo-4Ni-8Cr-24.5Fe	84
Figure 50: Thermo-Calc Scheil Simulation of M2: 3.5C-36Mn-10Mo-8Ni-22Cr-20.5Fe	84
Figure 51: Thermo-Calc Scheil Simulation of M3: 4C-58Mn-8Mo-10Ni-20Fe	85
Figure 52 a): DSC Curve for M1(Calorimetric signal: $\mu\text{V}/\text{mg}$)	86
Figure 53 a): DSC Curve for M2(Calorimetric signal: $\mu\text{V}/\text{mg}$)	87
Figure 54 a) DSC Curve for M3(Calorimetric signal: $\mu\text{V}/\text{mg}$).....	88
Figure 55: a) BSE image of MA1, b) BSE image of SA1, c) Cr WDS Map of MA1, d)Cr WDS Map of SA1, e)Mn WDS Map of MA1, f) Mn WDS Map of SA1, g) Mo WDS map of MA1, h) Mo WDS map of SA1, i) Ni WDS map of MA1, j) Ni WDS map of SA1(A Large Grain in MA1 is Outlined in a White Square).....	93
Figure 56: WDS Quantification Plots for a) MA1 - Line S1, b) MA1 - Line S2, c) SA1 - Line S1, d) SA1 - Line S2, e) SA1 - Line S3, f) SA1 - Line S4	95
Figure 57: a) BSE image of MA2, b) BSE image of SA2, c) Cr WDS Map of MA2, d)Cr WDS Map of SA2, e)Mn WDS Map of MA2, f) Mn WDS Map of SA2, g) Mo WDS map of MA2, h) Mo WDS map of SA2, i) Ni WDS map of MA2, j) Ni WDS map of SA2.....	97

Figure 58: WDS Quantification Plots for a) MA2 - Line S1, b) SA2 - Line S1, c) SA2 - Line S2, d) SA2 - Line S3, e) SA1 - Line S4.....	99
Figure 59: a) BSE image of MA3, b) BSE image of SA3, c) Mn WDS Map of MA3, d)Mn WDS Map of SA3, e) Mo WDS Map of MA3, f) Mo WDS Map of SA3, g) Ni WDS map of MA3, h) Ni WDS map of SA3	101
Figure 60: WDS Quantification Plots for a) MA3 - Line S1, b) MA3 - Line S2, c) SA3 - Line S1,d) SA3 - Line S2 and e) SA3 - Line S3.....	102
Figure 61: DICTRA Grid Types	112
Figure 62: DICTRA Schematic Example	114
Figure 63: Mn Diffusivity in FCC-Fe.....	120
Figure 64: Cr Diffusivity in FCC-Fe.....	121
Figure 65: Mo Diffusivity in FCC-Fe.....	122
Figure 66: Ni Diffusivity in FCC-Fe.....	123

List of Tables

Table 1: Commonly Used Powder Production Techniques and Respective Applications [8].....	4
Table 2: Alloying Elements and Their Effects on Various Steel Mechanical Properties [12], [13], [14]	6
Table 3: Industrial Automotive Component Composition.....	36
Table 4: Compositions (wt%) and d50 (μm) of Cr Master alloy and Mn Master alloy used in automotive component.....	36
Table 5: Summary of General DICTRA Simulation Details	45
Table 6: Initial Compositions for DICTRA Simulation for Cr MA Fe Case	47
Table 7: Overall Compositions (wt%) at T= 1280°C for Cr MA-Fe Case for DICTRA Simulation	48
Table 8: Initial Compositions (wt%) for DICTRA Simulation for Mn MA Fe Case.....	50
Table 9: Overall Composition (wt%) at T= 1280°C for Mn MA Fe Case for DICTRA Simulation.....	50
Table 10: Melting points of selected elements.....	68
Table 11: Solidification behavior of selected master alloys	69
Table 12: Properties of MMAs used in this work	71
Table 13: Chemical compositions of PM steels produced in traditional and specialized manners.....	75
Table 14: Mechanical properties and densities of PM steels produced in traditional and specialized manners	82
Table 15: Master Alloy Characteristics (Compositions, Liquidus Temperature and Weight Percent of Liquid at Various Sintering Temperatures)	83
Table 16: Calculated Overall Compositions To Achieve a D.I. of 4.0 inches	90
Table 17: D.I and Overall Compositions As Detected via ICP Chemical Analysis	90
Table 18: Green Strength and TRS for A1, A2 and A3 Alloy Sets	104

List of symbols

Symbol	Definition
$D.I.$	Ideal Diameter
MF_i	Multiplying factor of element i
ρ	Density
n_i	Moles of element i
J_i	Flux of element i
V_i	Drift velocity of element i
C_i	Concentration of element i
M_i	Mobility of element i
μ_i	Chemical potential of element i
G	Gibbs free energy
D	Diffusion coefficient
\tilde{D}	Interdiffusion coefficient
D_0	Pre-exponential term in the Arrhenius expression for the diffusion coefficient
X_i	Mole fraction of element i
x	Distance
t	time
T	Temperature
k	Boltzmann constant
R	Gas constant
g	Geometric parameter
ΔG_v^f	Gibbs free energy of formation of a vacancy
ΔG_s^m	Gibbs free energy of motion for the solute
γ	Surface energy
λ	Wavelength

Part I: Introduction to Powder Metallurgy (PM) and PM Design

Chapter 1: Literature Review

Introduction to PM

A multitude of different production techniques exists for the fabrication of steel parts, whether for the automotive industry, aerospace sector, a biomedical component or for an environmental application. Large-scale steel production techniques primarily encompass traditional approaches and processes including but not limited to casting, forging, stamping and machining [3]. This approach is typically associated with the concept of subtractive manufacturing. Although additive manufacturing continues to gain exposure and popularity, particularly 3-D printing, in the field of ferrous parts production, it is not yet suitable to be used for the mass-production of steel components and instead dominates in prototyping. When confronted with the task of producing large quantities of complex-shaped components, powder metallurgy (PM) poses as one worth looking into [1]. Powder metallurgy offers significant advantages over traditional wrought steel techniques in this arena of work. A few of these advantages include the ability to produce near-net shaped components for complex-shaped parts with overall reduced energy consumption and in certain circumstances, little-to-no post-processing operations including heat-treating and final machining [1], [2].

Brief History

Powder metallurgy technologies can be dated back thousands of years [6] where the heating or sintering, of ceramic powders has been used for several millenniums. Some of the oldest sintered metal artefacts made of gold, silver and copper from the Middle East can be dated back to 3000 B.C [7] . Other ancient findings that have been discovered to be produced by sintering include tools created by Inca and Egyptian civilizations as well as ancient Chinese and European porcelains. However, although ceramic and metal powders have been used for thousands of years, the modern sintering era can be attributed to Coolidge's development of a durable lamp filament made of tungsten powder, one that would later be used by Edison. For PM materials, the beginning of the 20th century included the fabrication of tungsten alloys, electrical contacts and ferrous structural alloys. Today, PM applications continue to expand in diversity and can be found in just about any industry. This includes power-train components for the automotive sector, rocket nozzles for aerospace applications, dental implants and even sports applications for the production of golf clubs[4].

PM Process Summary

As for the realm of ferrous materials, the production of a steel component via a traditional powder metallurgy process entails four basic steps that include powder metal production, powder blending, compaction and sintering [3], [4]. Although densified and much stronger than its as-compacted state (commonly referred to as the green body), in many cases, the sintered product still requires post-sintering treatments to further improve mechanical properties such as tensile strength and hardenability. Post-sintering treatments include austenitization, quenching in liquids

or gases and tempering. A summary of the production of a typical PM component can be seen in Figure 1.

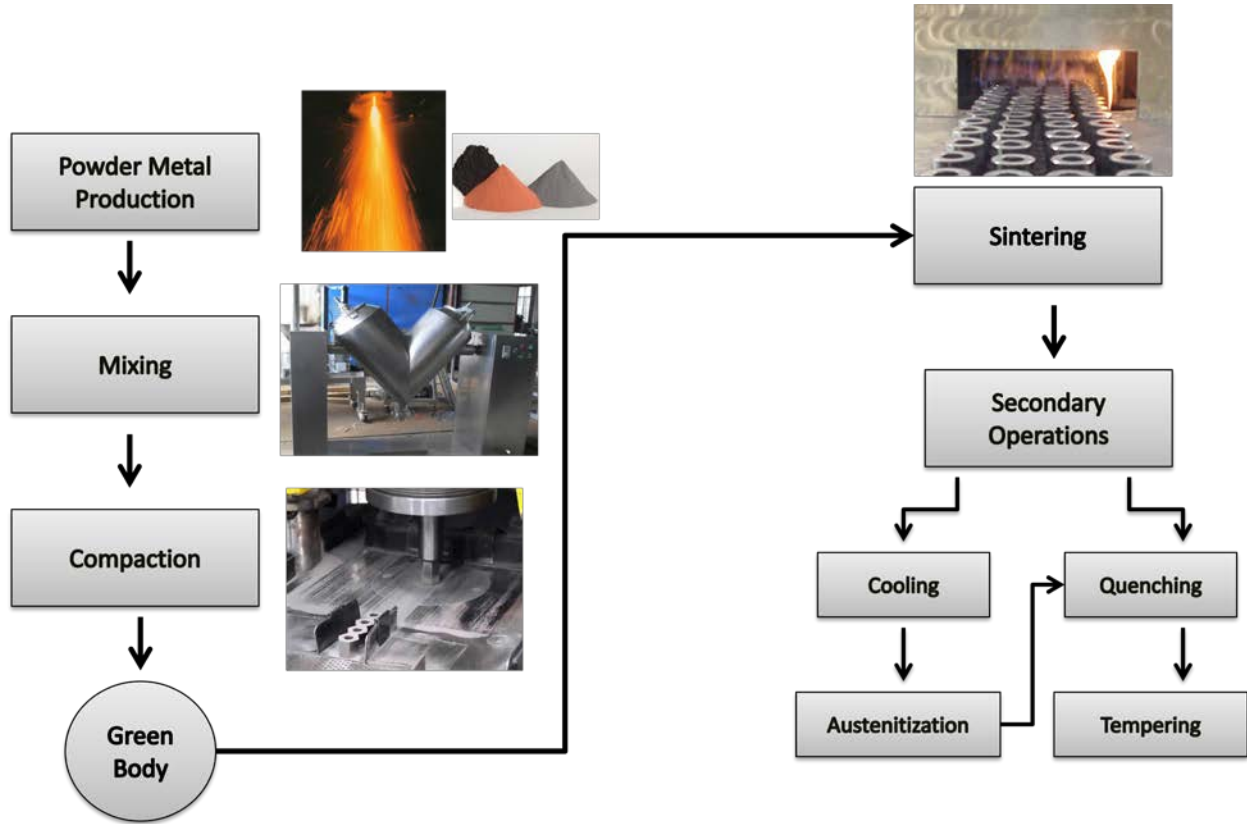


Figure 1: Powder Metal Processing Route Summary

Powder Metal Production

As for powder metal production, a variety of methods can be used to create metal powders. The selected method depends on the properties which the final powder should possess. Pure iron powder can be fabricated via carbon and hydrogen reduction or atomization while non-ferrous powders can be produced via electrolysis, melting and milling as well as other variations of atomization including plasma, centrifugal and close-coupled techniques. To produce iron particles that already contain alloying element additions, prealloying or diffusion alloying

techniques may be used [8], [9]. Table 1 summarizes commonly used powder production techniques and properties that are associated with powders fabricated by the particular method.

Table 1: Commonly Used Powder Production Techniques and Respective Applications [8]

	Water Atomized Iron	Hydrogen Reduced Base Iron	Carbon Reduced Base Iron	Prealloyed Base Irons	Diffusion Alloyed Base Irons
Application	High density applications: <ul style="list-style-type: none"> • Sprockets • Bearing caps 	Specialty applications: <ul style="list-style-type: none"> • Semi-metallic break pads • Oxygen absorbers 	Low density applications: <ul style="list-style-type: none"> • Bearings • Bushings • Shock absorbers 	High performance applications: <ul style="list-style-type: none"> • Gears • Sprockets 	High performance applications: <ul style="list-style-type: none"> • Synchro- hubs • Lawn and garden transmissions
Alloying Additions	None	None	None	Yes - added in melt stage	Yes - added to finished iron powder and annealed

Powder Mixing

As for powder mixing, devices of various geometries can be used to blend powders together and can be mixed on different axes. This can range from cylindrical mixers, double-cone and cube mixers that vary upon their rotational axes. During the blending stage of ferrous component blends, iron base powder is typically mixed with graphite powder, lubricant powder as well as alloying additions [3]. Lubricant powder such as Kenolube™ is necessary to reduce the wear and damage of production tools such as punches and dies that are used for compaction practices. Alloying element additions can be incorporated at this stage into the powder blend in the form of pure metal powders or master alloys.

Alloying Element Additions

Alloying element addition in the context of PM component production is a crucial aspect of the design stage and its effects are evident in the mechanical properties of the final component. As done in the wrought steel realm, alloying additions in the PM industry are chosen strategically based on the properties that they can help to create and improve, whether corrosion-related or associated with mechanical performance. Table 2 summarizes alloying elements and their effects on various steel properties.

As for improving hardenability, elements to look at when designing for a hardenable steel include carbon, molybdenum, chromium and manganese [10], [11], [12]. Hardenability is the property which reflects the depth that hardening, or formation of martensite, will occur in a given section during quenching. It is affected by both austenitic grain size and steel composition. Here it is also worth introducing the concept of ideal diameter (D.I.) which measures the largest diameter of a component, 50% of which forms martensite [5]. D.I. can be calculated as follows:

$$D.I. \text{ (inches)} = D_{IC} \times MF_{Mn} \times MF_{Cr} \times MF_{Mo} \times MF_{Ni} \quad (1.1)$$

In equation 1.1, D_{IC} represents the ideal diameter for the system's base carbon content while $MF_{\text{Alloying Element}}$ represents the multiplying factor of the different alloying elements that are included in a given steel system [5]. Figure 2 shows the correlation between ASTM grain size and carbon content in regards to D.I., while Figure 3 shows the multiplying factors of different alloying elements.

Table 2: Alloying Elements and Their Effects on Various Steel Mechanical Properties [12], [13], [14]

	Carbon	Chromium	Nickel	Manganese	Molybdenum
Effect	<ul style="list-style-type: none"> • Increase in hardness and hardenability • Increase in wear resistance • Brittleness and reduction in toughness if added in excessive amounts 	<ul style="list-style-type: none"> • Increases toughness and wear resistance • Increases hardenability 	<ul style="list-style-type: none"> • Increases ferrite strength • Increases toughness and hardenability in low-alloy steels 	<ul style="list-style-type: none"> • Slightly increases ferrite strength • Increases hardenability 	<ul style="list-style-type: none"> • Increases hardenability • Increases tensile strength

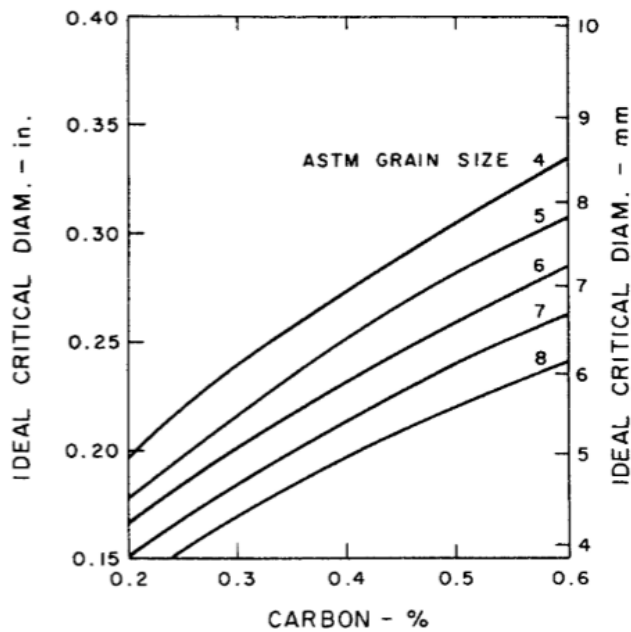


Figure 2: Ideal Diameter (D.I.) as a Function of Carbon Content and ASTM Grain Size[5]

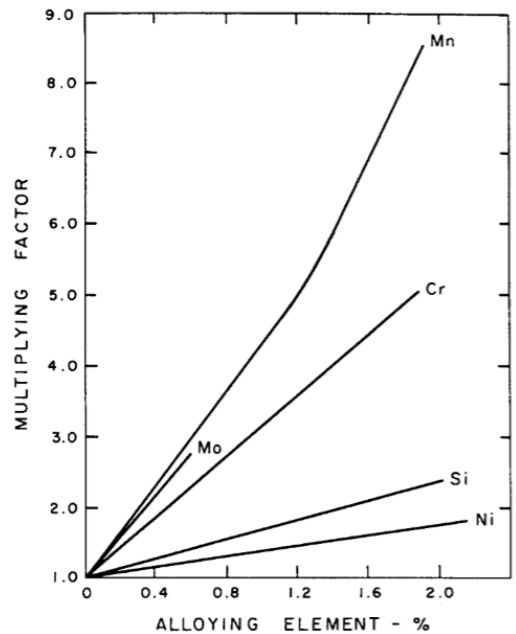


Figure 3: D.I. Multiplying Factor of Various Alloying Elements [5]

PM Steel Porosity and Effect on Properties

Mechanical properties of a PM steel vary with density. Evidently, the greater the porosity in a PM component, the lower the density and in many cases, the lower the value of the property being analyzed. Equation (1.2) provides a means to estimate the performance of a porous PM steel in comparison to a full-density part such as a wrought steel of the same composition.

$$\frac{P}{P_o} = \left(\frac{\rho}{\rho_o}\right)^m \quad (1.2)$$

Here, P represents the property of interest for the PM material, P_o pertains to the property of the pore-free material, ρ is the density of the PM material, ρ_o is that of the pore-free material and m is an exponent value related to the property of interest (ie. thermal conductivity, elastic moduli, fatigue strength and unnotched impact energy). Figure 4 provides an estimation of m for these various properties as well as $\frac{P}{P_o}$ values in relation to relative density ratios. It is worth emphasizing that $\frac{P}{P_o}$ values approaching 0 are more characteristic of foams than PM steels. A PM steel of density 7.0 g/cc can be associated with approximately 10% porosity in a single micrograph (as detected by ImageJ software [15]), an example of which can be seen in Figure 5.

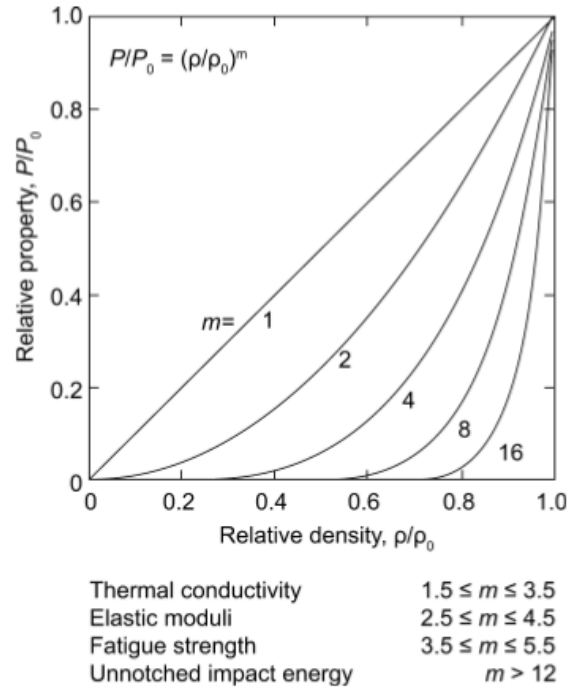


Figure 4: Effect of PM Density on Various Properties

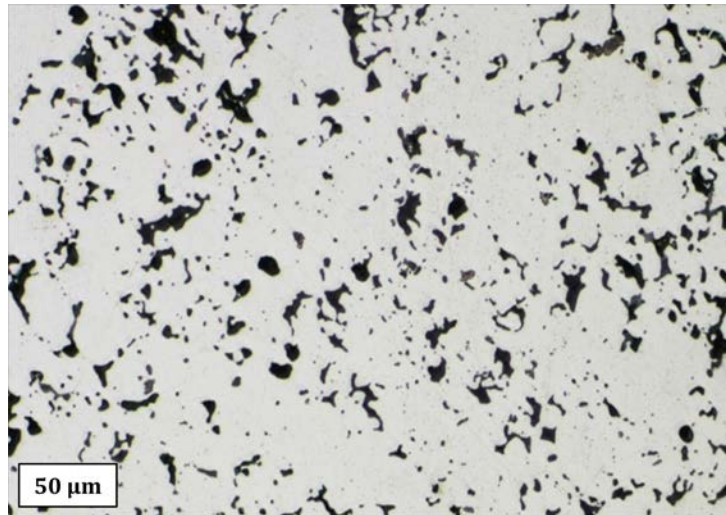


Figure 5: Porosity for a 7.0 g/cc sintered PM steel

Compaction

Once powder blending with appropriate alloying elements and lubricant is complete, one can proceed to the compaction step. Basic tools that are used for compaction include a punch and a die. The most common compaction methods include a) uniaxial compaction, b) double-action compaction, c) compaction with a floating die and d) stripped die compaction method as seen in Figure 6. Uniaxial and compaction involves movement of the punch a single direction while double-action compaction involves pressure being applied from the top and bottom of where the powder is filled. Compaction with a floating die includes a die being suspended on springs. The stripped die method involves the die being stripped by the lower piston such that the powder metal compact is then released [3]. Here it is worth noting that compaction can be done cold, warm or hot. Progressing through the processes (from cold to hot) results in the green body having a higher density. After a die has been filled with powder and compacted, the resulting product is a loosely-held together base component known as a green body. As the green body's mechanical properties are insufficient to withstand large loads, it must be heat treated to improve in strength. The first heat treatment in the PM production process is known as sintering.

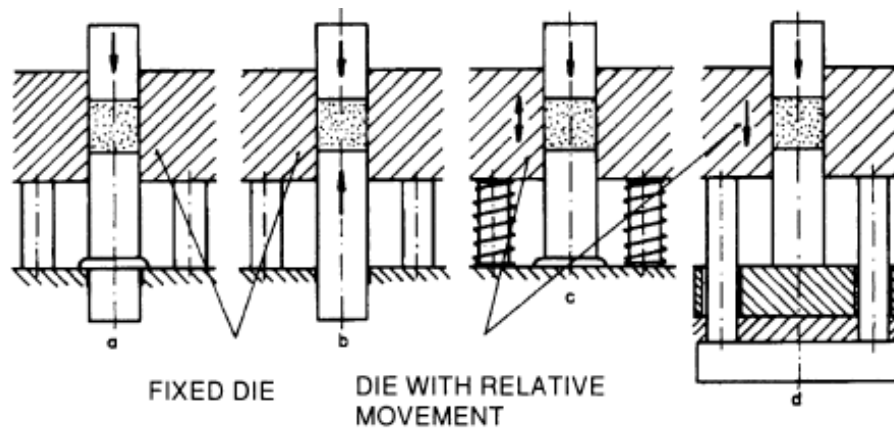


Figure 6: Common Compaction Methods[3]

Sintering

The sintering heat treatment takes place within a sintering furnace - of which there are many types. Sintering furnaces can range from a chamber set-up, vacuum or continuous sintering furnace, the latter of which is the most commonly found in large-scale PM component production. The purpose of the sintering atmosphere within the continuous sintering furnace is to remove lubricant, ensure that carbon decarburization does not occur and reduce surface oxide films that form on either the surfaces of individual particles or the entire part. A typical continuous sintering furnace has 5 zones: 1) dewaxing, 2) preheating, 3) heating, 4) precooling and 5) final cooling as seen in Figure 7.

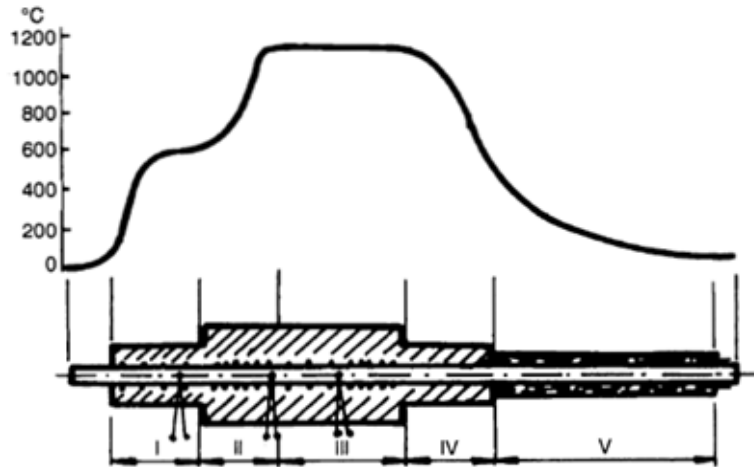


Figure 7: Continuous Sintering Furnace With 5 Zones: I) Dewaxing, II) Preheating, III) Heating, IV) Precooling, V) Final Cooling [3]

The purpose of the first zone is for dewaxing, otherwise known as removal of lubricant. It is essential that any lubricant which is added in during the blending stage is removed prior to sintering. For this very reason, the dewaxing zone is set at a temperature typically between 425°C to 650°C. This temperature range is high enough to break down and vaporize the lubricant such that it leaves the green body as an off-gas, but low enough such that any sintering-related activities are not yet activated. If lubricant is burnt out at temperatures which are used for sintering, diffusion-related processes that take place during sintering activate and can eventually lead to sooting and micro-cracking in the PM component. The preheating zone which is typically set anywhere between 650°C to 1150°C serves as a region to increase the furnace temperature to the sintering temperature such that once it reaches the high-temperature zone, the green body can remain at the sintering temperature for the longest amount of time. Once in the high-temperature heating zone which is set anywhere between 1050°C to approximately 1150°C (or even higher for high-temperature sintering activities), all sintering-related diffusion processes are activated. Unless rapid cooling is required immediately after, such as for a sinter-hardening process, a

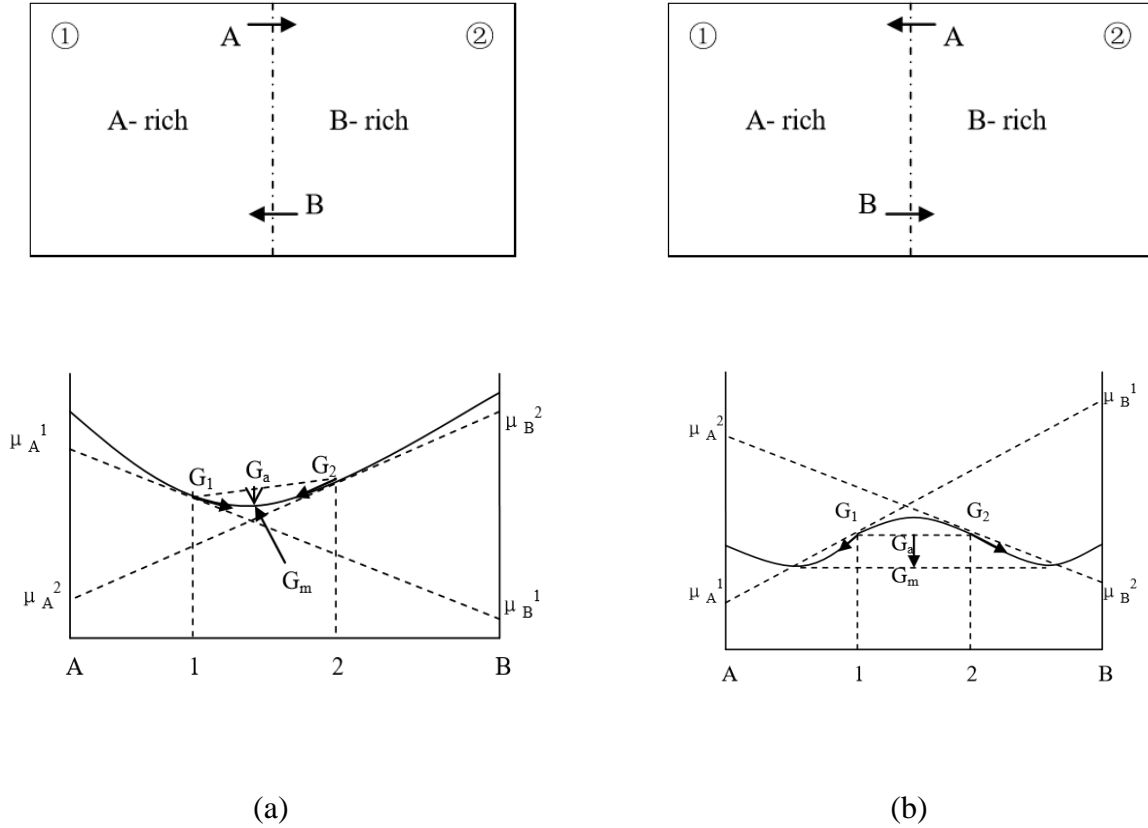
precooling zone exists where the sintered products are slow cooled and then directed to a final cooling zone where rapid cooling takes place.

Diffusion During Sintering Processes

Homogenization during sintering depends on diffusion-related mechanisms that take place at this stage. It is important to keep in mind that diffusional processes are driven by more than just a concentration gradient. A given material will strive toward equilibrium and as a result, diffusion can occur due to concentration, electrical fields, thermal fields and mechanical stresses. Diffusion is therefore driven by the Gibbs free energy gradient and will occur until it is at a minimum as seen in Figure 8a) and b). This entails that in certain cases, diffusion may occur against a concentration gradient. Here it is worth defining the chemical potential, μ , which is known as the partial molar Gibbs free energy [16]:

$$\mu_i = \left(\frac{\partial G}{\partial n_i}\right)_{T,P,n_j}$$

Where μ_i is the chemical potential of species i , G is the Gibbs free energy, n_i represents the number of moles of species i , T and P represent the constant temperature and pressure and n_j represents the number of moles of every species other than the i th species.



Both scenarios seen in Figure 8a) and b) show that A and B atoms diffuse from regions of high chemical potential to regions of a low chemical potential. Here, Fick's first law, which is representative of a non time-dependent net flow of atoms, can be written as [18]:

$$J_A = v_A C_A \quad (1.3)$$

where the flux of A atoms, J_A is related to concentration C_A and drift velocity v_A which takes into account atomic mobility M_A and the chemical potential gradient $\partial\mu_A$:

$$v_A = -M_A \frac{\partial\mu_A}{\partial x}$$

Therefore [19],

$$J = -M_A C_A \frac{\partial \mu_A}{\partial x} \quad (1.4)$$

or

$$J = -D_A \frac{\partial C_A}{\partial x} \quad (1.5)$$

Here, $\frac{\partial \mu_A}{\partial x}$ is the chemical potential gradient for A atoms. If $\frac{\partial \mu_A}{\partial x_A} > 0$, then the diffusion coefficient $D_A > 0$ and gradient of the chemical potential will be in the same direction of the concentration gradient however, if $\frac{\partial \mu_A}{\partial x_A} < 0$, then $D_A < 0$ and diffusion will occur against the concentration gradient. Equation 1.5 is the more commonly seen equation for Fick's first law - which helps one to understand diffusion from both a steady-state and non-steady state perspective [18]. $\frac{dC}{dx}$ is the concentration gradient and in all cases, D is the diffusion coefficient which will be elaborated upon after discussing Fick's second law. As previously highlighted, flux is proportional to the chemical potential gradient of a component which is related to the activity gradient of a component.

Fick's second law provides one with an understanding of non-steady state diffusion, where concentration is a function of both time and position. In its most general form, respective of various geometries, it can be written as:

$$\frac{\partial C}{\partial t} = -\frac{J}{\partial z} \quad (1.6)$$

$$\frac{\partial C}{\partial t} = \frac{1}{z^n} \frac{\partial}{\partial z} \left(z^n D \frac{\partial C}{\partial z} \right)$$

Provided that the diffusion coefficient is constant, the above equation can be written as:

$$\frac{\partial C}{\partial t} = D \left(\frac{n}{z} \frac{\partial C}{\partial z} + \frac{\partial^2 C}{\partial z^2} \right) \quad (1.7)$$

Here, C and z represent concentration and distance respectively, while t represents time, the value of n represents the dimension and D is once again the diffusion coefficient which takes various forms depending on the system of analysis.

In its intrinsic form, D is dependent on D_o , the pre-exponential term in the Arrhenius expression for the diffusion coefficient [18], temperature (T), the universal gas constant (R), and activation energy (Q).

$$D = D_o e^{\frac{-Q}{RT}} \quad (1.8)$$

The diffusion coefficient of two or more species can be related by an interdiffusion coefficient (\tilde{D}), a weighted average of D_A and D_B [18]. This is relevant for diffusion within substitutional alloys at higher solute concentrations.

$$\tilde{D} = X_A D_B + X_B D_A \quad (1.9)$$

Where X_A and X_B represent the mole fractions of species A and B while D_A and D_B represent the diffusion coefficients of each species within the alloy [18].

As for a substitutional solute characterizing diffusion in a dilute solution, the diffusion coefficient (D_s) can be characterized as follows [18]:

$$D_s = gva^2 \exp\left(-\frac{\Delta G_v^f + \Delta G_s^m}{kT}\right) \quad (1.10)$$

Where g is the geometric parameter representing the range of possible directions in which an atom can jump (typically $g \approx \frac{1}{6}$), a is the lattice spacing, ν is vibration frequency, ΔG_v^f is the Gibbs free energy of formation of a vacancy and ΔG_s^m is the Gibbs free energy of motion for the solute.

Major Mass Transport and Sintering Phenomena

The two main mass transport mechanisms that take place during sintering include surface and bulk transport [4]. Bulk transport mechanisms include volume diffusion, grain boundary diffusion and plastic flow whereas surface transport mechanisms include evaporation-condensation and surface diffusion in addition to volume diffusion. Each mass transport mechanism can contribute to the overall flux of atoms differently. Grain boundary diffusion will be used as an example to show its contribution to the previously discussed "lattice" flux. As grain boundaries provide a convenient path for atoms to travel through, this mass transport mechanism can significantly improve the homogeneity of a PM compact. A schematic of this mass transport phenomena can be seen in Figure 9 where δ represents the grain boundary width and d represents the width of a grain (of course, simplified into planar geometry in the schematic).

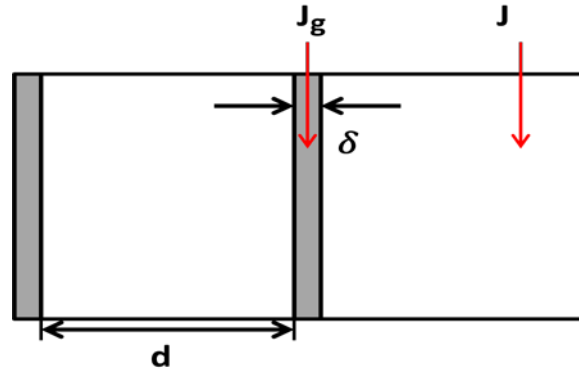


Figure 9: Schematic of Grain boundary Diffusion (J_g : flux due to grain boundary diffusion, J_l : flux due to lattice diffusion)

Grain boundary diffusion can be incorporated into flux as such [20]:

$$J_g = -D_g \frac{dC}{dx} \quad (1.11)$$

Where recall that lattice diffusion can be written as:

$$J_l = -D_l \frac{dC}{dx}$$

Therefore, the effective flux can be written as:

$$J_{\text{eff}} = \frac{dJ_l + \delta J_g}{d + \delta} \approx -(D_l + \frac{\delta}{d} D_g) \frac{dC}{dx} = -D_{\text{eff}} \frac{dC}{dx} \quad (1.12)$$

or

$$D_{\text{eff}} = (1-g)D_l + gD_g \quad (1.13)$$

As grain boundaries are not yet properly formed upon the onset of sintering, grain boundary diffusion is more dominant in the later stages of sintering. In this case, surface diffusion can

help enhance chemical homogeneity during the early stages of sintering where grain boundaries do not abundantly exist as it allows atoms to effectively travel along the surfaces of particles. Evaporation-controlled sintering is prevalent when materials of high vapor pressures are within a green body. Diffusion processes in evaporation-controlled sintering can be characterized by gas diffusion in a solid – an example of which entails Mn vapor diffusing throughout Fe particles in a PM body. A summary of all bulk and surface transport mechanisms can be seen in Figures 9 and 10. Finally, although not discussed in great detail, should an interested reader want to learn about multi-component diffusion, it is recommended to review the work of N. Garimela [21].

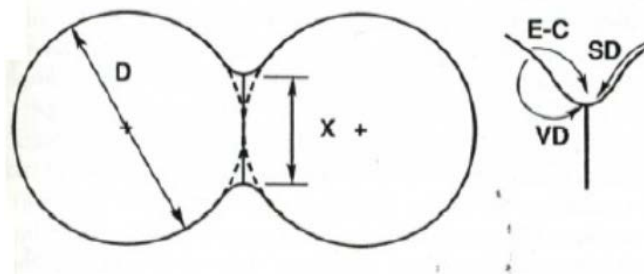


Figure 10: Surface Transport Mechanisms (E-C: Evaporation-Condensation, SD: Surface Diffusion, VD: Volume Diffusion [4])

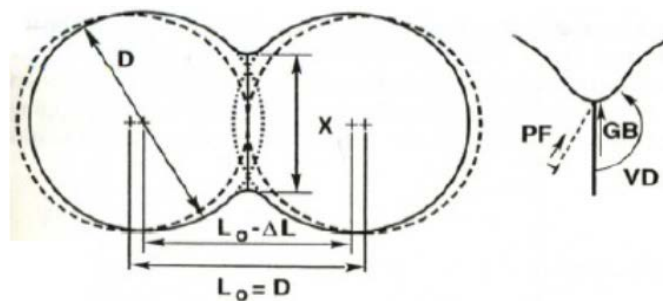


Figure 11: Bulk Transport Mechanisms (PF: Plastic Flow, GB: Grain Boundary Diffusion, VD: Volume Diffusion [4], X: width of neck, D: particle diameter, ΔL : change in particle diameter)

Solid-state transport mechanisms are of course slower than liquid and gas-processes but still do contribute to other sintering phenomenon including necking and densification of the green body. Surface transport mechanisms contribute to neck growth while bulk transport mechanisms are known to contribute to neck growth and shrinkage due to densification as seen in Figure 10 [4].

Necking and densification entail the process by which solid-solid interfaces replace initial particle-pore interfaces. It is important to understand that although complete densification seems advantageous as mechanical properties would approach those of a wrought steel with the exact same composition, it is not always a desired feature. Although this indeed would mean the dismissal of any issues related to porosity, a significant degree of densification can result in the dimensional change of the PM component from green body to final part. Therefore, in the case that complete densification is desired, a different compaction technique is recommended such as hot iso-static pressing such that when a green body produced via such a compaction technique is then sent to be sintered, the final and fully-treated component can be fully-densified [4], [3].

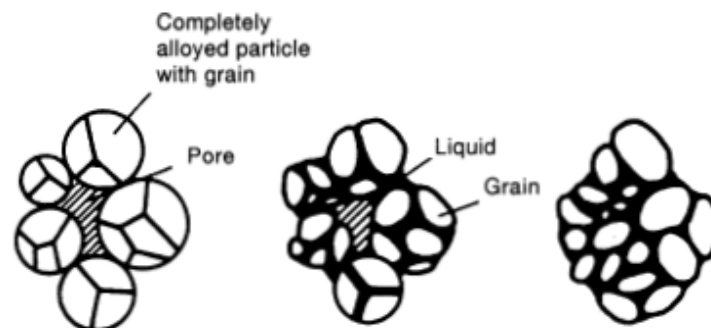


Figure 12: Liquid Phase Sintering (LPS) Phenomena Depicting Melting and Redistribution of Grains By Melting of "Master Alloy" Particles [3]

Liquid phase sintering, a schematic of which is depicted in Figure 12, is known to enhance homogenization processes as the liquid phase can serve as a carrier to distribute alloying elements in a more effective manner [3], [22], [23]. The improved homogenization that is observed due to this phenomena has also been correlated with superior mechanical properties and performance for a given PM component [24], [25]. Copper is a popularly used element for many ferrous alloys that are to exhibit liquid phase sintering [26] as it can assist with strength and microhardness of a PM component [27, 28], however when added in excess, can actually deteriorate mechanical properties due to segregation to grain boundaries [29]. The advantage of improved homogeneity as seen from liquid phase sintering does however come at the expense of swelling [30]. If an alloy particle forms a liquid phase during sintering, swelling can occur and can further increase if the liquid dissolves atoms from the matrix.

Importance of Wettability and Solubility for Alloy Design

Wettability can be characterized by the contact angle evolution of the liquid master alloy on a solid iron substrate, a schematic of which can be seen in Figure 13 along with Young's equation (1.14) governing it.

$$\gamma^{sv} = \gamma^{sl} + \gamma^{lv} \cos \theta \quad (1.14)$$

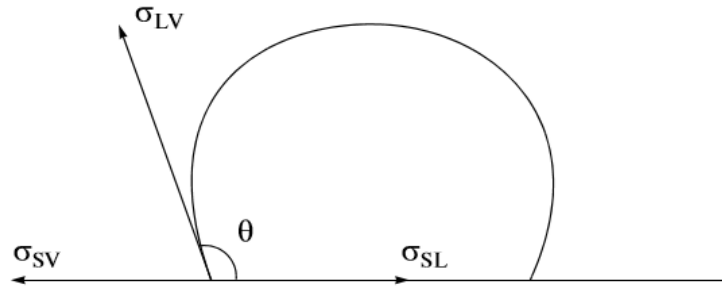


Figure 13: Wettability Schematic (γ^{sv} : solid surface free energy, γ^{sl} : solid/liquid interfacial free energy, γ^{lv} : liquid surface free energy, θ : contact angle)[31]

Good wetting behaviour associated with a low wetting angle, promotes the distribution of the liquid along the surface of solid particles. It is worth highlighting that the presence of surface oxides can impede good wettability [32]. In the presence of a reducing atmosphere, wettability improves as evidently, any existent surface oxides get reduced. In the absence of a reducing atmosphere however, wettability is still seen to improve in the presence of a master alloy with elements of a high oxygen-affinity [32]. An example of both scenarios can be seen in Figure 14 and Figure 15

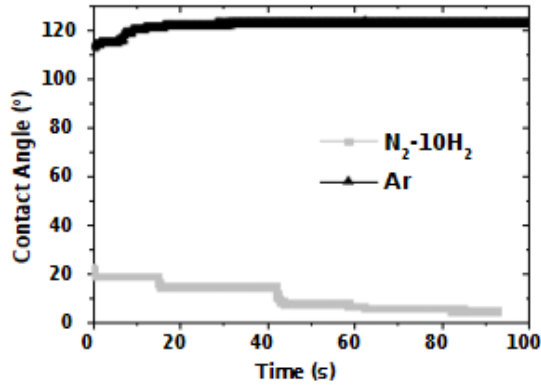


Figure 14: Contact angle evolution for a Cu alloy on an Fe substrate in a reducing (N_2-10H_2) and inert (Ar) Atmosphere [32]

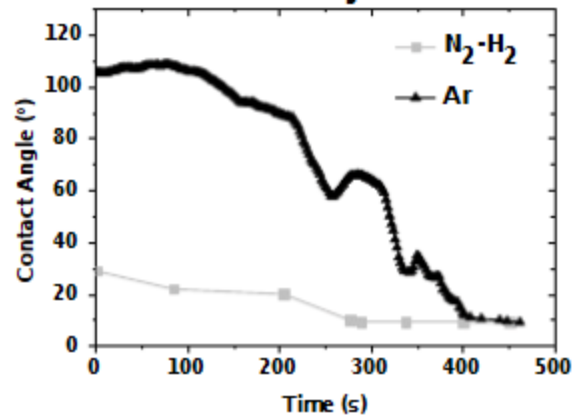


Figure 15: Contact angle evolution for an Fe-Mn-Si alloy on an Fe substrate in a reducing (N_2-H_2) and inert (Ar) Atmosphere [32]

The liquid's ability to penetrate and distribute throughout a PM component, otherwise known as infiltration, can be characterized by the solubility of the solid in the liquid for a given temperature as seen on a phase diagram [33]. Figures 15 and 16 display the pseudo-binary phase diagram of a master alloy of either Cu or Ni-4wt%Cu-12w%Si. Figure 15 shows a low dissolutive master alloy characterized by the master alloy being able to engulf a small amount of the Fe solid substrate. and Figure 16 shows a high dissolutive master alloy, characterized by the liquid master alloy being able to engulf a significant amount of the Fe solid substrate.

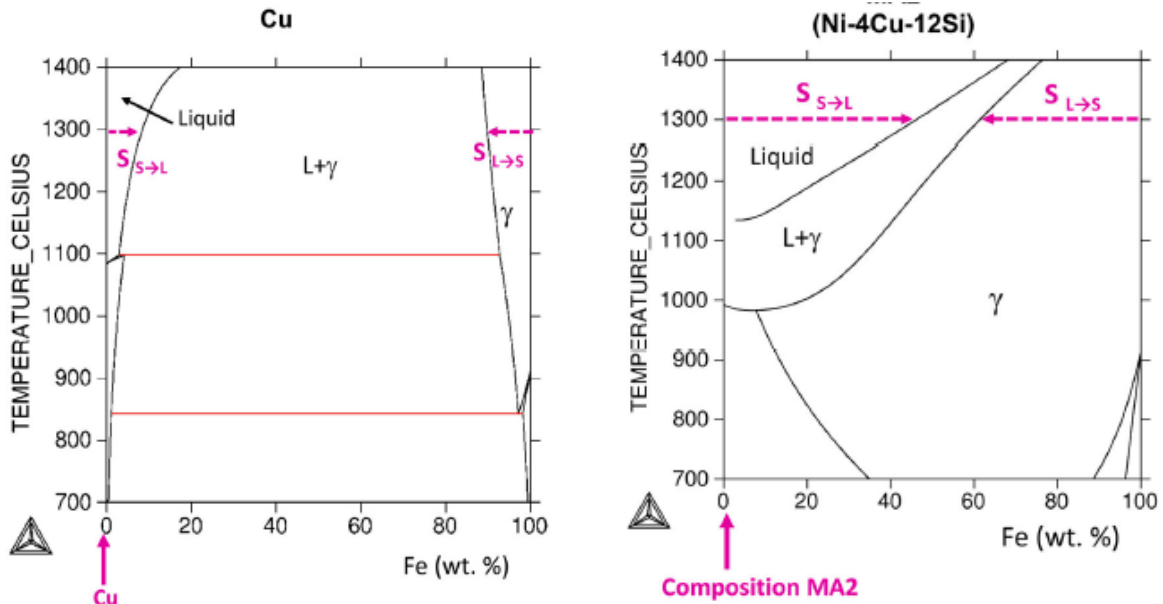


Figure 16: Cu LPS-Activating Alloy (Low-Dissolutive)[33]

Figure 17: Ni-4Cu-12Si LPS-Activating Alloy (High-Dissolutive) [33]

Master Alloy Design and The Scheil-Gulliver Paradigm

Approaches to implementing LPS in the alloy design context has been heavily associated with analyzing equilibrium solidification range [34], [35], [36], rather than taking a look at the Scheil-Gulliver paradigm. Alloy particles designed for LPS include master alloys: particles that contain multiple alloying elements and contribute to a significant portion of the particle's overall composition. Designing these master alloys by considering the equilibrium solidification range closes off the possibility of lower-temperature liquid phase sintering for many different compositions merely due to the narrower solidification range that is available to an equilibrium-based analysis. An example of this is seen in Figure 17, where if one would like to conduct low-temperature sintering for an alloy with composition X_o , it simply would not be possible for the

selected composition as the sintering temperature is located below the solidus temperature. The Scheil-Gulliver model assumes that no diffusion takes place in the solid phase and that there is fast mixing in the liquid [37]. The solidification range can be extended from the liquidus temperature to the eutectic temperature and is much more likely to encompass the sintering temperature [38].

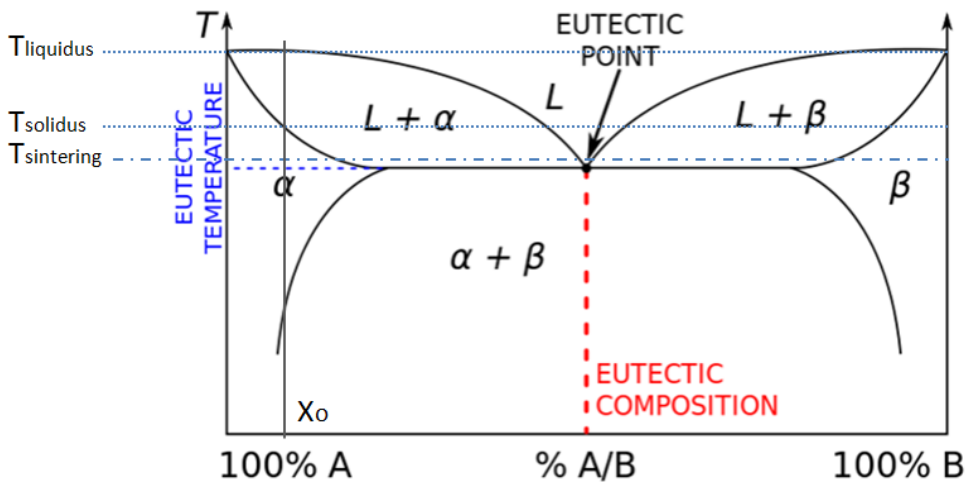


Figure 18: Solidification ranges for Equilibrium and Scheil-Gulliver Solidification For Composition X_0

Since many master alloys are produced through a solidification approach, their microstructures thereby inherit a non-equilibrium make-up. When this solidification path is back-tracked, a particular fraction of liquid can be calculated for a particular sintering temperature. Figure 19 shows a Scheil solidification schematic accompanied by appropriate equations. C_0 represents the overall composition whereas C_L is the composition of the liquid and c_S is the composition of the solid. Fractions of the liquid and solid are v_L and v_S respectively.

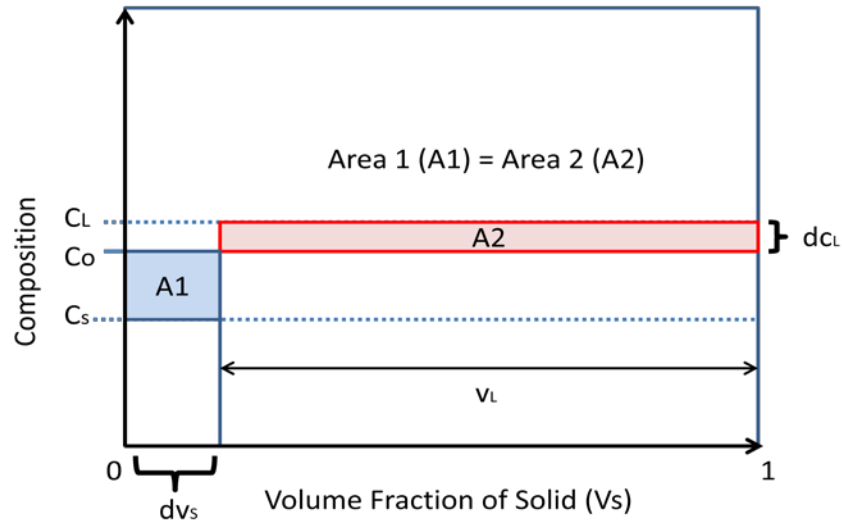


Figure 19: Scheil Solidification Schematic

$$dc_L(v_L) = dv_s(C_L - C_S) \quad (1.15)$$

where $v_S + v_L = 1$ and $C_S = kC_L$

$$C_L = C_o(1 - v_s)^{(1-k)} \quad (1.16)$$

$$C_S = kC_o(1 - v_s)^{(k-1)} \quad (1.17)$$

Electron Microscopy

A wealth of information can be extracted from the various signals that are detected within a scanning electron microscope (SEM). Signals that can be given off and detected in an SEM include Auger electrons, back-scattered electrons, secondary electrons, X-rays and cathodoluminescence [39], [40] as seen in Figure 20. Signals that have been found most useful in

the context of homogenization studies in PM include backscattered electrons and X-rays that are incorporated into energy dispersive X-ray spectroscopy (EDS) and primarily wavelength dispersive X-ray spectroscopy (WDS) analyses. Due to their close interactions with an atom's nucleus, back-scattered electron (BSE) can be used to identify chemical inhomogeneities by displaying different grey-scales based upon average atomic differences between two elements. X-rays can be used to determine exact elements and can be analyzed by both EDS and WDS, the latter technique being much more precise - particularly for trace elements.

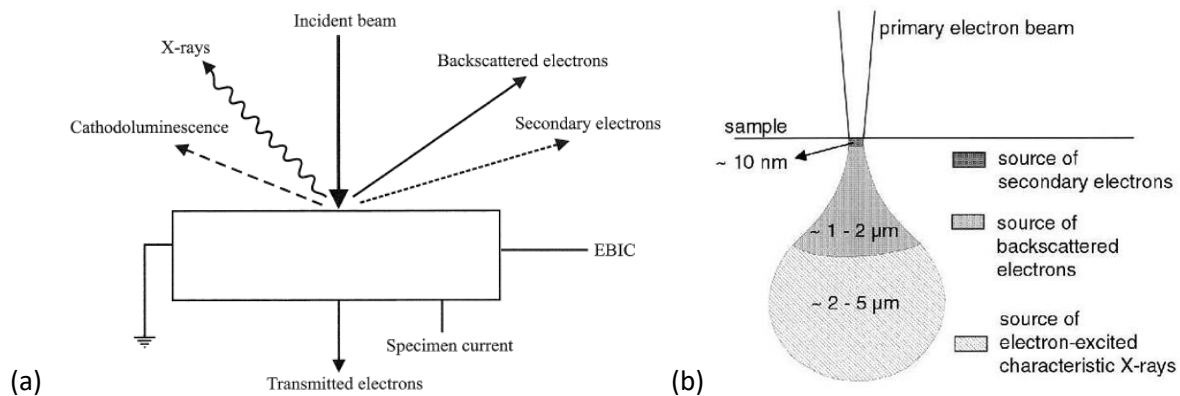


Figure 20: a) Signals given off in an Electron Microscope [39] and b) Sample Interaction Volume

After electrons that are emitted and shot down from an SEM gun in the form of an electron beam, the electrons bombard the specimen under examination and various types of electron scattering take place. Inelastic scattering takes place and involves the ejection of an electron from an inner orbital of an element. An electron from an orbital outside this shell will then drop to an inner shell, resulting in the emission of an X-ray characteristic of the element it was released from. As for EDS, X-rays of all elements simultaneously enter into a detector where

they are converted to voltage signals that are then processed and converted by an analyzer which displays the quantity of an element present depending on the amount of X-rays received.

As for WDS, characteristic X-rays that satisfy Bragg's law as seen in Figure 21, are the only ones that get reflected by an analytical crystal with specific lattice spacing (d) which is part of the WDS set-up.

$$n\lambda = 2d\sin(\theta) \quad (1.18)$$

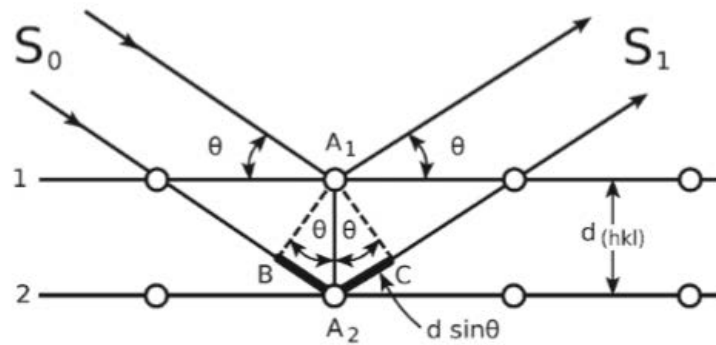


Figure 21: X-Ray refraction with Analytical Crystal[41], (S_0 and S_1 : incoming and diffracted X-rays respectively)

In order to detect a X-ray of different wavelength which is representative of a different element, the analytical crystal will change position by rotating along the Rowland's circle as seen in Figure 22 . As the angle (θ) between the sample and the crystal are now different, a different wavelength (λ) of X-ray and therefore different element can now be analyzed.

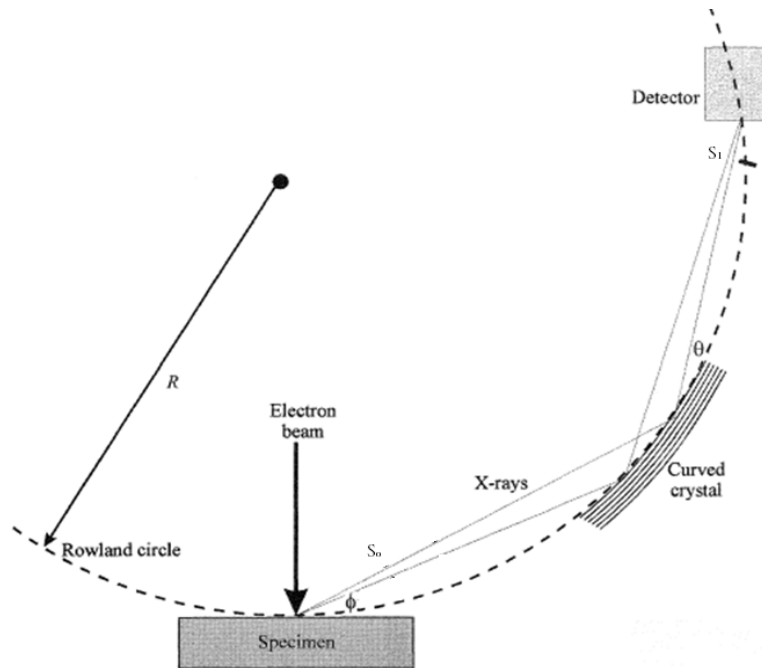


Figure 22: Rowland Circle With Specimen, Analytical Crystal and Detector [39] (S_0 and S_1 : incoming and diffracted X-rays respectively, ϕ : take-off angle of X-rays)

Computational Thermodynamics and Previous Work

Computational thermodynamics includes the application of computers and software to simulate and solve thermodynamic-related problems in materials science. Software packages, including Thermo-Calc and DICTRA can be used specifically not only to create phase diagrams, but also to predict the formation of phases that form as a result of diffusion in binary as well as multi-component systems [42].

In PM literature, DICTRA is cited as a valuable computation tool that has already been used for modelling various ferrous PM-related processes including sintering. *Oro et al.* and *Bernardo et al.* utilized DICTRA in order to simulate master alloy systems for LPS (liquid phase sintering) and transient LPS of PM steels. Master alloy systems of interest analyzed in these studies

involved Fe-Mn-Si in addition to Cu-based Ni-Si and Ni-based Cu-Si as demonstrated in Figure 23 [43], [34]. As seen in Figure 24, Shykula *et al.* used DICTRA to study Mn diffusion into ASC 100.29 iron where Mn was introduced in the form of a MA containing Fe-40wt%Mn-10wt%Si-1wt%C [44].

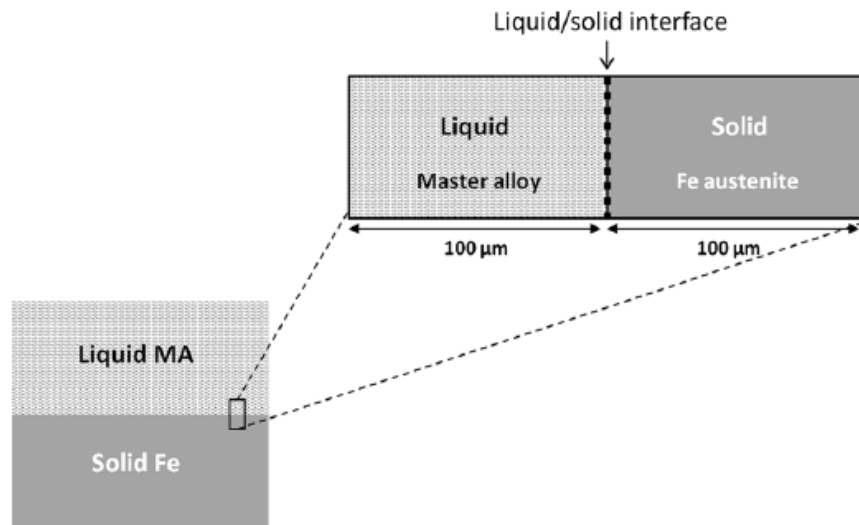


Figure 23: General MA-Fe System Schematic Set-Up for DICTRA Simulation [34]

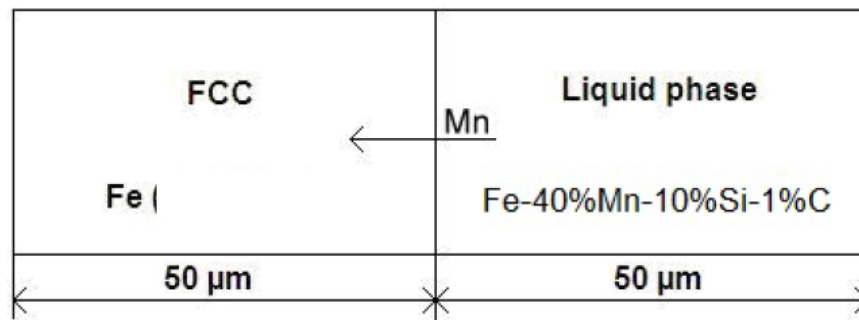


Figure 24: Fe-MA DICTRA System Set-Up to Study Diffusion of Mn from Fe-40wt%Mn-10wt%Si-1wt%C Master Alloy into FCC Iron [44]

Other research involving the study of alloying element diffusion, particularly for solid-state-sintering studies of ferrous PM materials, include modelling diffusion in components produced via HIP (hot-isostatic pressing) [45] and MIM (metal-injected moulding) processes [46]. These studies investigated alloying element diffusion profiles as well as phase evolution. However, it should be emphasized that ferrous PM materials produced via HIP and MIM processes have a much lower porosity fraction and are thereby more comparable to wrought-steel components in terms of microstructural characteristics than traditionally sintered components.

Previous Experimental Work

With an emphasis on lean powder metal component production, several studies have been made to investigate the most efficient use of each and every alloying element addition in PM (powder metallurgy) steels. Such efforts include optimizing final product chemical homogeneity which can enhance overall mechanical properties [47]. A variety of approaches have tried to improve overall chemical homogeneity of alloying elements in PM steels as they undergo sintering, some of which include altering alloying element size and starting chemical composition [47], [48]. Other approaches include increasing sintering temperature and time as seen in Figure 25, [49] where in particular, temperature has a dominant effect on improving homogeneity as diffusivity is exponentially related to it [4]. In the industrial realm however, an increase in sintering time translates into lower sintering furnace belt speeds which can limit production capabilities while furnaces with higher heating capabilities are expensive.

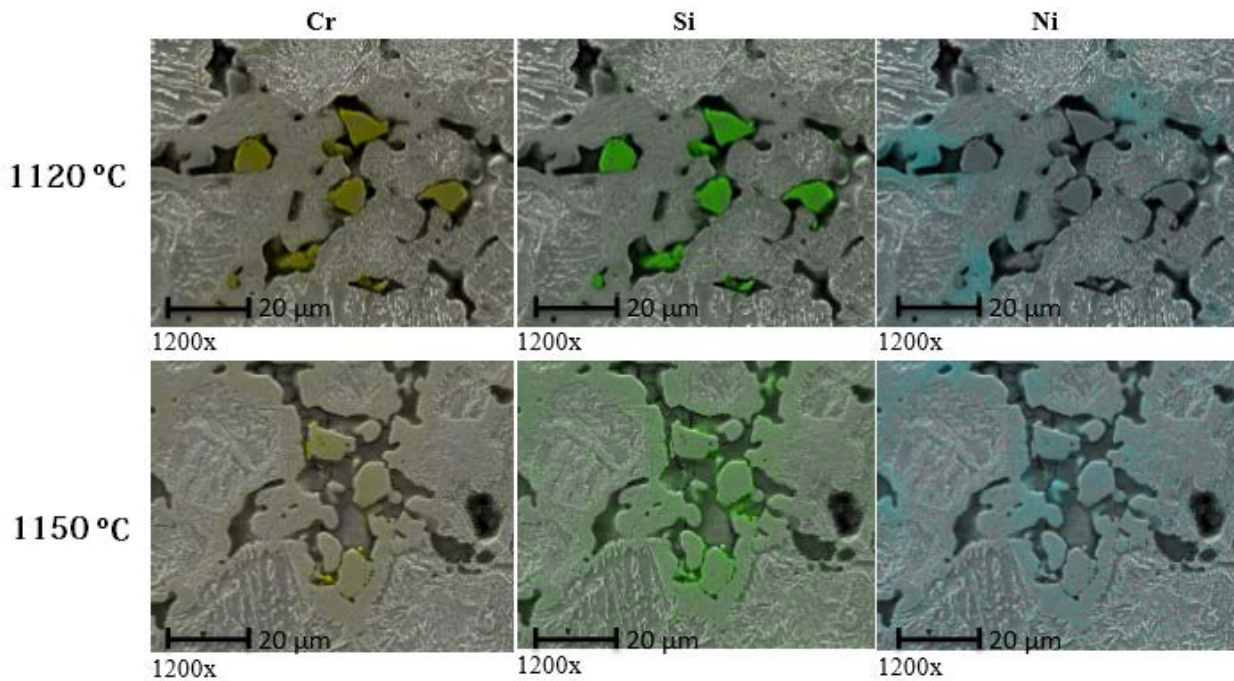


Figure 25: Analysis of Improving Cr, Si and Ni Homogeneity By Increasing Sintering Temperature - Detected by EDS [49]

As for LPS, in addition to previous findings that were mentioned in terms of improving homogenization via the master alloy route, a multitude of different compositions have been investigated for ferrous systems. Examples include the work of *Oro et al.*, where Fe-Mn-Si, Fe-Mn-Si-C, Fe-Mn-Si-C-Cr-Ni systems were analyzed [23], [50] and Si-Mn-Ni-C master alloys as investigated by *Demetrio et al* [25]. Observations included the confirmation of the presence of the liquid phase, the occurrence of swelling, improvement in homogeneity and overall mechanical properties. Figure 26 a) and b) show low and high dissolutive master alloys (as highlighted by white arrows) after being sintered in a 95%N₂-5%H₂ atmosphere. Low dissolutive liquids are said to exhibit rapid, even penetration through pores and around iron grains while

high-dissolutive liquid were able to spread to further distances due to an increased capacity to absorb iron.

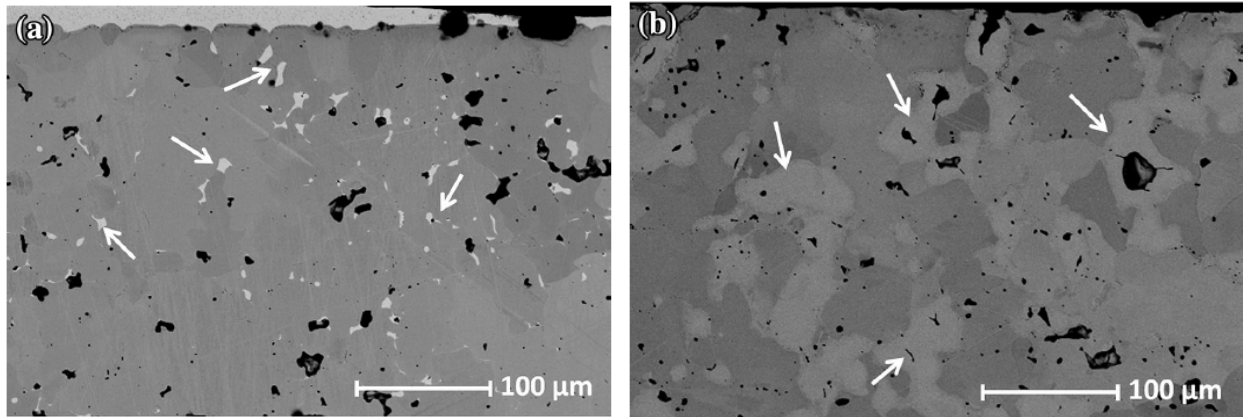


Figure 26: a) Low Dissolutive Master Alloy Behaviour and b) High Dissolutive Master Alloy Behaviour[51]

Chapter 2: Scope and Objectives

This research consists of designing a PM steel with improved chemical homogeneity. A combination of computational thermodynamics (DICTRA, Thermo-Calc and Fortran), sintering experiments, wavelength dispersive spectroscopy (WDS) elemental mapping and quantification paired with mechanical testing presented in this investigation has yet to be carried out by other researchers and serves to be a complimentary advancement to previous work done in the field. The scope of this study is to therefore evaluate the homogenization behaviour of alloying elements in PM steels during sintering as well as investigate liquid phase sintering of master alloy additions to understand and optimize the homogenization behaviour of alloying sources and mechanical properties of PM steels.

WDS analyses on partially and industrially sintered components provide elemental maps that tracked the evolution of alloying elements as they relax to homogeneity. WDS analyses were conducted on an industry-produced automotive component that was sectioned and sintered industrially at 1280°C and 1300°C as well as experimentally at 1280°C for 30 minutes and 13.4 hours.

DICTRA modeling in combination with WDS incremental sintering experiments and scanning electron microscopy (SEM) - (WDS) was used to compare how alloying additions containing Cr, Mn, Fe and C homogenize during sintering in simulation and experimental case. DICTRA simulation results of alloying sources were studied alongside alloying element profiles obtained by compiling point quantification from wavelength dispersive spectroscopy maps for the sintered

automotive component.

As for fabricating master alloy additions, Thermo-Calc software and Fortran, were used to identify multi-component master alloys with promising compositions in Fe-C-Cr-Mn, Fe-C-Cr-Mn-Ni, Fe-C-Mn-Mo, Fe-C-Mn-Mo-Ni and Fe-C-Cr-Mn-Mo-Ni systems for liquid phase sintering. Systems of Fe-C-Cr-Mn-Mo, Fe-C-Cr-Mn-Mo-Ni and Fe-Mn-Mo-Ni were fabricated and tried in practice. Compositional maps and mechanical properties of PM steels made with variations of this specially tailored multi-component master alloys were compared with those for which traditional alloy sources were used. The scope of the mechanical properties included hardness, tensile strength, yield strength, green strength and transverse rupture strength.

Part II: An Experimental and Computational Approach to Understanding the Homogenization Behaviour of Alloying Elements During the Sintering of PM Steel

The purpose of this portion of the study is to combine sintering experiments, electron microscopy techniques and computational analyses to better understand diffusion behaviour of alloying elements including Cr and Mn with an end goal of providing relevant suggestions to industry to optimize PM alloy design and sintering treatments. For this, Thermo-Calc and DICTRA software are used as computational tools to simulate diffusion profiles of alloying elements over various sintering times. Results are compared with elemental WDS (wavelength dispersive spectroscopy) maps of a sectioned industry-produced automotive component that has been both experimentally and industrially sintered. In addition to this comparison, DICTRA is also used as a computational tool to evaluate the behaviour of a pure versus enriched MA (master alloy) and a single versus multi-component MA in order to predict which forms better promote homogenization of alloying elements.

Chapter 3: Sintering Experiments

Sintering Experiments

Experiments involved sintering an industrial automotive component containing Fe, Cr, Mn, Ni and C. Overall composition of the component as well as compositions of alloying element MA sources can be found in Tables 3 and 4.

Table 3: Industrial Automotive Component Composition

Cr	Mn	Ni	C	Fe
0.5	0.6	0.4	0.6	balance

Table 4: Compositions (wt%) and d_{50} (μm) of Cr Master alloy and Mn Master alloy used in automotive component

Cr MA Composition (wt%) and d_{50} (μm) particle size				Mn MA Composition (wt%) and d_{50} (μm) particle size			
Cr	Fe	C	d_{50}	Mn	Fe	C	d_{50}
61.0	30.3	8.7	12.6	76	17.2	6.8	10.1

The component was obtained in industrially sintered and green body form. The green body was sectioned into parallelepipeds, each of which was sintered within a tube furnace with an Ar-5.06H₂ protective atmosphere at 1280°C for times including 30 minutes and 13.4 hours after being de-lubricated for approximately 3 minutes at 1000°C in Ar. After undergoing sintering experiments, the specimens were then subjected to cooling in air outside of the furnace. A schematic of the overall procedure can be seen in Figure 26. The industrial sintering treatment involved heating to 1280°C at a rate of 30°C per minute followed by an isothermal hold at 1280°C for 20 minutes and cooling at a rate of 30°C per minute. All specimens were then cold-mounted, vacuum-desiccated and prepared for microscopy analyses. Grinding was conducted

down to a 1200 mesh followed by ultrasonic cleaning in acetone. The final polishing step was completed with 0.05 μ m alumina.

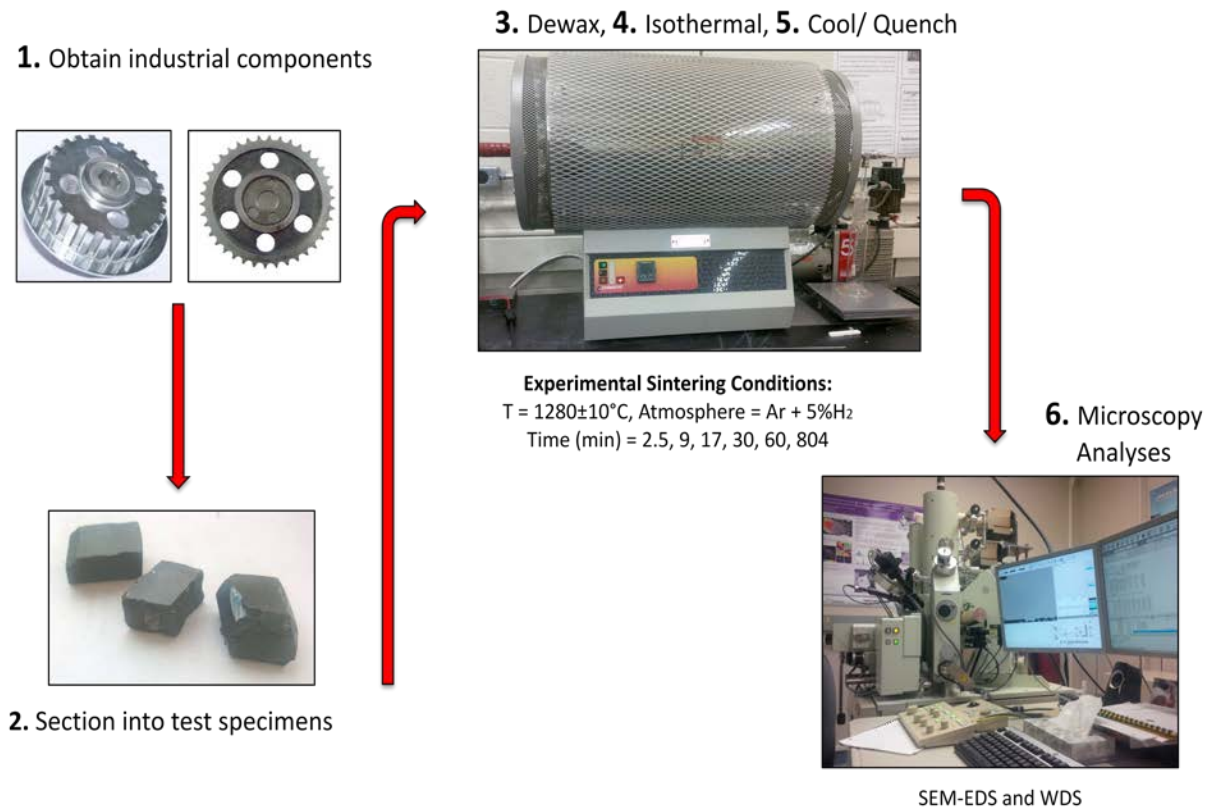


Figure 27: Experimental Summary

Chapter 4: Electron Microscopy: EDS and WDS Investigations

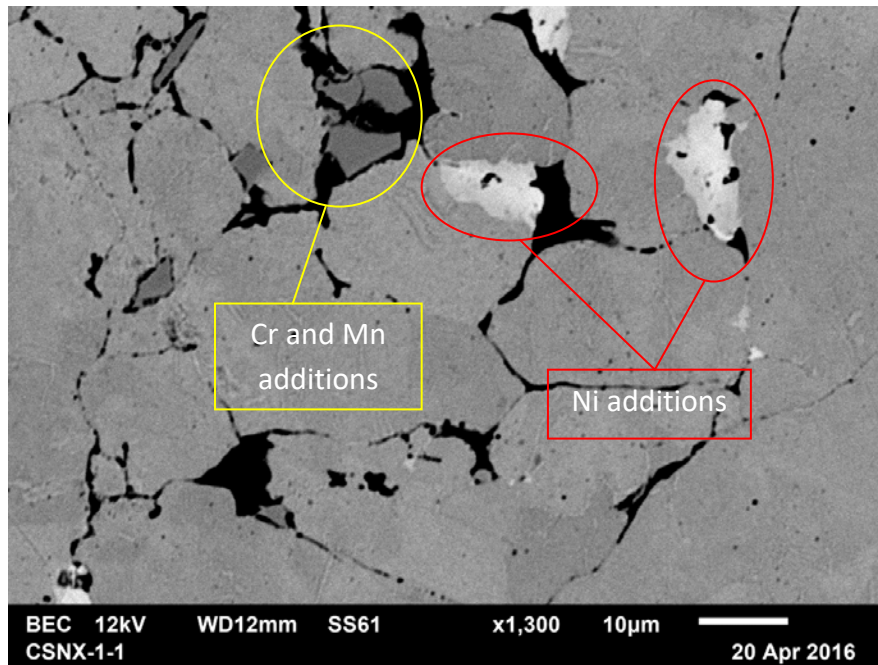


Figure 28: SEM of PM Green Body (Example 1)

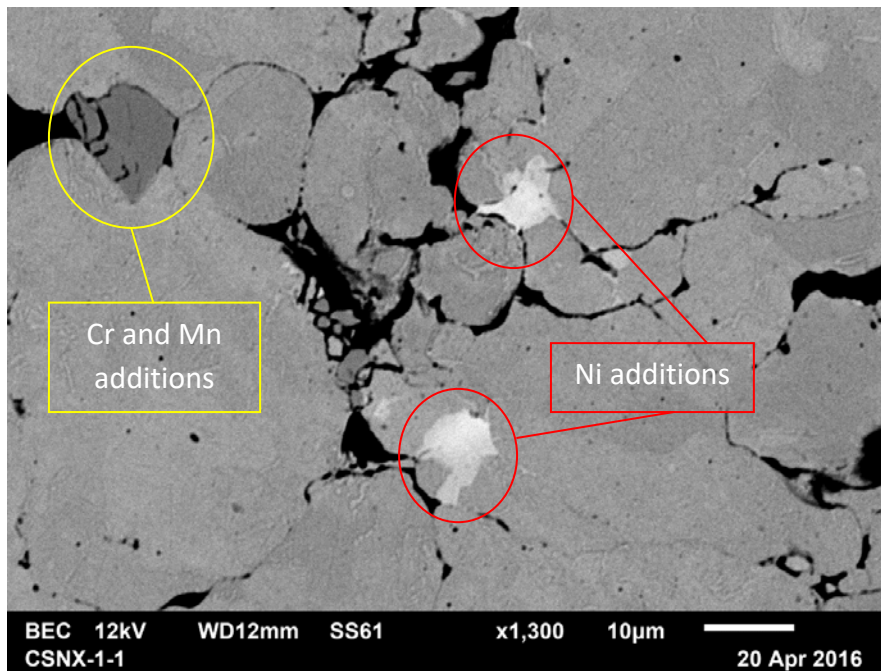


Figure 29: SEM of PM Green Body (Example 2)

Prior to carrying out elemental mapping, a JEOL 6610-LV was used for backscattered electron imaging. The images can be seen in Figure 28 and Figure 29 where brighter regions correspond to Ni additions and darker portions correspond to ferromanganese and ferrochromium sources. The green body was dewaxed at 1000°C for 3 minutes. A JEOL JXA-8530F field emission microprobe was used for electron microscopy analyses which involved WDS (wavelength dispersive X-ray spectroscopy). Analyses were carried out for Cr, Mn and Ni. EDS was used as a preliminary step to carry out point-analyses on arbitrarily selected points throughout the specimens to estimate compositions at various locations. This step was then followed by building WDS compositional maps of Cr, Mn and Ni. WDS maps were constructed for 700 μm^2 areas. Points of high, medium and low alloying element concentrations were selected, quantified and later compiled in the form of lines across alloying element sources. An error of approximately 0.01wt% is estimated to be associated with the analyses conducted on this microscope. Pure metal standards obtained from Astimex Standards Limited (METM25-44) were used for this analysis. Brighter pink regions on elemental maps correspond to regions of higher concentrations while darker purple regions correspond to regions of lower concentrations. Smaller rounded black regions correspond to porosity. As maps are not quantitative in nature, in order to find actual compositions, specific points were quantified to determine concentration values particularly for Cr and Mn. Points for quantification were selected along lines outlined in yellow in Figure 30 and were chosen to pass through regions of low and high colour intensity from the elemental maps.

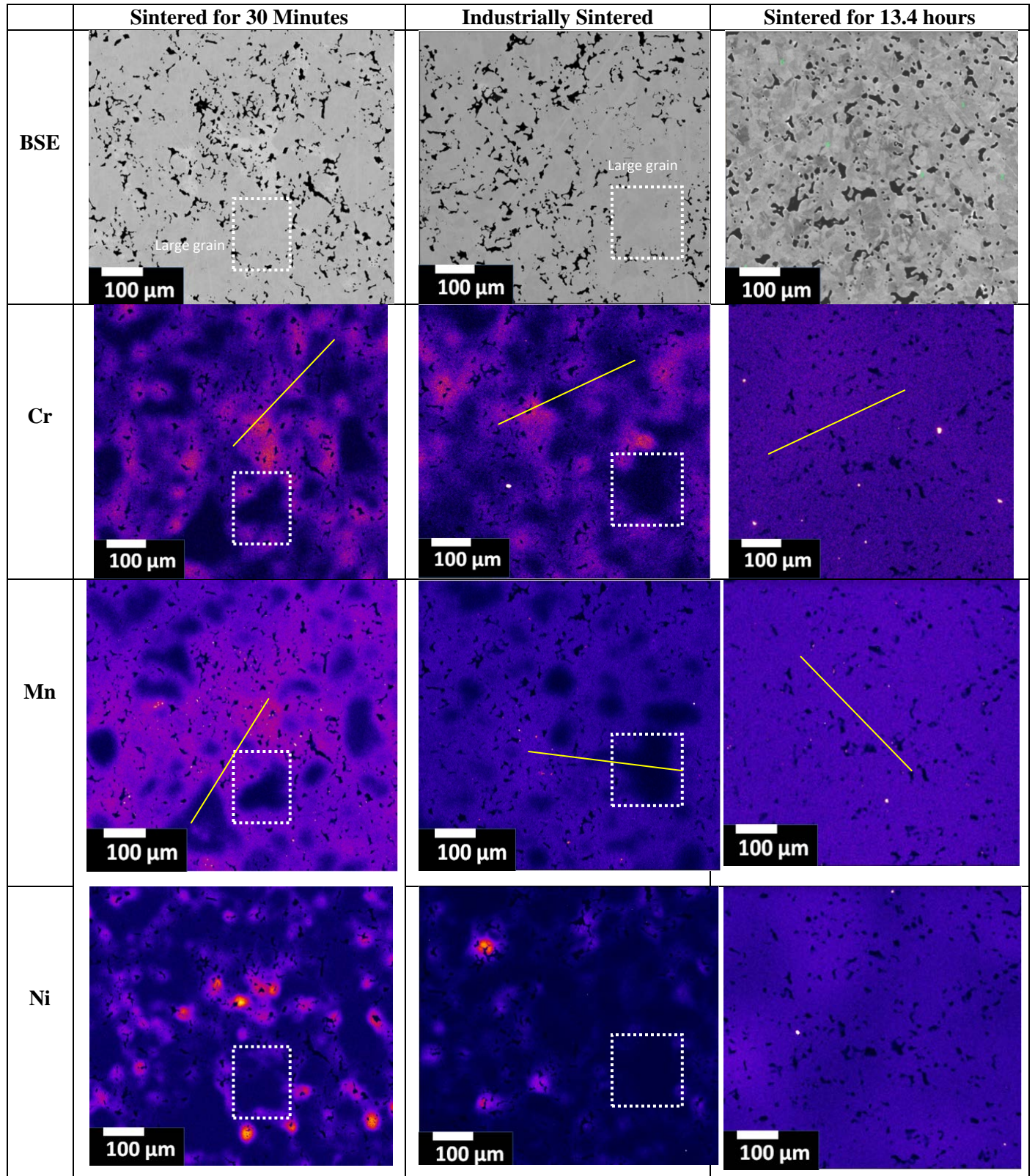


Figure 30: BSE and WDS elemental maps of industrial automotive component (Large grains outlined by white boxes)

Compositional maps obtained through WDS are shown in Figure 30. Images in the first row correspond to BSE (backscattered electron) images and do not display much chemical contrast here. Elemental maps obtained via WDS detect finer variations in chemical content much more effectively. The second, third and fourth rows of Figure 30 contain compositional maps of Cr, Mn and Ni respectively while the first, second and third columns pertain to sintering for 30 minutes, overall industrial treatment and 13.4 hours respectively.

Initial alloying element sources after 30 minutes of sintering can be identified much more easily for Cr and Ni than for Mn. These initial sources are at the centres of the brighter, high intensity spots on the maps. For Mn, not as many alloying element sources can be identified, most probably due to the element's combination of solid-state diffusion with its vapour transport [12]. Researchers have found that sintering with Mn additions results in the formation of Mn vapour at sintering temperatures. The Mn vapour is known to fill pores within PM compacts and deposit on Fe particle surfaces. Once Mn envelops Fe surfaces, it is able to continue diffusing within the Fe particle [12], [52], [53]. Furthermore, through Thermo-Calc calculations, it is also known that at 1280°C, the employed Mn MA composition has a liquid volume fraction of approximately 0.56; as a result, the LPS that takes place can also enhance the homogenization of Mn [3].

At 30 minutes and industrial sintering times, it can be seen that larger iron grains (as outlined by white boxes) are not properly alloyed. The long-term sintering time of 13.4 hours shows that Cr, Mn and Ni were successfully homogenized. The improvement in degree of homogenization can be attributed to the significant increase in time, however, although capable of producing an advantageous chemical homogeneity, it is obvious that a sintering time of 13.4 hours is not industrially feasible. For this purpose, in case study 2, DICTRA was used to investigate whether altering alloying element delivery form, particularly of Cr and Mn (ie. MMA: multi-component

master alloy instead of SMA: single component master alloys) could provide a more practical method of improving alloying element distribution.

Chapter 5: DICTRA Simulations

Thermo-Calc and DICTRA simulations were conducted in two case studies; the first case study simulates the diffusion profiles of Cr and Mn individually when introduced to an iron matrix from a) a Cr MA and b) a Mn MA. Both MAs had compositions similar to those already employed in industry. The purpose of this case study is to evaluate the relevance of DICTRA's prediction capabilities by comparing these results to diffusion profiles of Cr and Mn obtained from WDS. The second case study compares the homogenization behaviour of Cr and Mn when introduced into an iron-carbon matrix in the form of a) a single master-alloy and b) a multi-component master alloy in order to predict which master alloy form proves to better enhance alloying element homogenization during sintering.

TCFE6 (Steels/Fe-Alloys V 6.2) database was used for all Thermo-Calc and DICTRA calculations. MOBFE1 mobility database was also used for DICTRA simulations. DICTRA simulations were carried out using the homogenization model which is suitable for diffusion through a multi-phase system [54]. Flux of a species i is calculated in the homogenization model as follows [55], [56]:

$$J_i = -\frac{1}{V_S} \times M_i \times u_i \times \frac{\partial \mu_i}{\partial z} \quad (1.19)$$

$$\text{where } u_i = \frac{x_i}{\sum_{j \in S} x_j}$$

Here, V_S is the molar volume of substitutional elements and is assumed to be a constant of $1 \times 10^{-5} \text{ cm}^3$ in DICTRA. M_i and μ_i are the mobility and chemical potential of species i

respectively and u_i is the u-fraction commonly used in DICTRA where it is defined as the mole fraction x_i taken over the summation of substitutional elements only.



DICTRA can handle planar, cylindrical and spherical geometries. A planar geometry was chosen as it was the only one allowing two “particles” to be side-by-side and freely transfer matter [54]

All simulations were conducted at 1280°C, which is not too far from sintering temperatures employed by manufacturers of ferrous PM materials. All simulations consisted of a single region which was divided into sub-regions to represent the initial state of MA particle co-existing with an iron or iron-carbon particle. Initial composition profiles for each element were defined as Heaviside functions such that they embodied a sharp step-change at each sub-region boundary in order to represent sharp MA particle | iron or iron-carbon matrix particle interfaces. A geometric grid-spacing [54] was selected for sub-regions in order to focus in on processes occurring at the “pseudo” computational interface between the alloying element addition and the iron/iron-carbon particle. Using a 1280°C isothermal section of appropriate phase diagrams, a list of phases to include in each simulation was compiled; this list included phases given the initial compositions for each system and phases that may potentially form upon diffusion of elements. Table 5 lists all phases used in each simulation. All simulations included FCC as the active matrix phase while all other phases were selected to be active and spheroidal [54]. The simulation set-up for each case study set is depicted and summarized in terms of simulation details and parameters in Table 5. Appendix A contains more information relevant to DICTRA simulations and parameters that are specified here.

It was ensured that each simulation’s overall alloying element content was comparable to respective industrial alloying element content. As for the first case study, the iron matrix

thickness was so selected that it was large enough to permit alloying elements in each MA to contribute to an overall alloying element content of less than 1.0 wt% in the entire system. As for the second case study, alloying element content in each MA particle (single or multi-component) was selected such that they would entail an industrial relevant overall composition.

Table 5: Summary of General DICTRA Simulation Details

Schematic and Point Set-Up								
Case Study	1				2			
Subset	1 a)		1b)		2a)		2b)	
General Description	Cr MA Fe		Mn MA Fe		Cr Mn MA Fe Cr Mn MA		Cr MA Fe Mn MA	
Sub-Regions	MA	Fe	MA	Fe	MA1 and MA2	Fe	MA1 and MA2	Fe
Number of Points	9	99	9	99	9 in each MA	48	9 in each MA	48
Phases Included	BCC $M_{23}C_6$ and M_7C_3	FCC	Liquid, M_5C_2 and M_7C_3	FCC	BCC, Liquid and $M_{23}C_6$	FCC	BCC, Liquid and $M_{23}C_6$	FCC
Phase Type	All spheroidal	Matrix	All spheroidal	Matrix	All spheroidal	Matrix	All spheroidal	Matrix
Thickness	10 μm	990 μm	10 μm	990 μm	5 μm each side	90 μm	5 μm each side	90 μm

Appendix A contains more details about DICTRA and exemplary command-line code used

Individual and overall compositions for each simulation is specified in the results and discussion section.

The following simplifications and assumptions were made:

1. 1-D Planar geometry
2. Constant sintering temperature
3. Exclusion of porosities

4. Inclusion of a limited amount of possible phases that could form during diffusional processes due to degree of difficulty to compute simulations if too many phases are included
5. Exclusion of grain boundary and dislocation-assisted diffusion parameters due to uncooperative nature of the parameters when turned on for simulations particularly containing C

Keeping the mentioned simplifications in mind, below is the methodology used when carrying out DICTRA simulations:

1. Overall system was divided into sub-regions where each sub-region pertained to either a MA particle, iron or iron-carbon particle
2. Composition values of alloying elements within sub-regions were selected. (*As DICTRA experiences computational difficulties dealing with pure elements, approximately 0.0011wt% of each element was included in the iron/ iron-carbon sub-region.*)
3. Mass of each respective sub-region system at sintering temperature was calculated using Thermo-Calc
4. Master-alloy sub-region thickness (master-alloy particle size) was selected based upon approximate MA size employed in industrial practice
5. Overall alloying element compositions were calculated using a simple mass balance
6. Particle size from step 4. was altered until desired overall alloying element composition was obtained
7. Alloying element content in particle was entered into Thermo-Calc to determine starting phase-portrait of system

8. Overall alloying element content was entered into Thermo-Calc to carry out a single-point equilibrium calculation to ensure that this composition fell within a single-phase region
9. System composition and particle size information was entered into DICTRA and simulations were conducted

It must be emphasized that due to ambiguous computational errors, unreasonably long simulation times, and abrupt simulation terminations, it was extremely difficult to produce the DICTRA results that are presented in this study.

Simulation for sintering Cr Master Alloy (Cr MA)

Case Study 1 for investigation a): Cr MA attached to Fe matrix (Cr MA | Fe)

Table 6 contains initial composition details that were entered into DICTRA while Table 7 contains calculated composition values that the entire system should attain upon complete homogenization.

Table 6: Initial Compositions for DICTRA Simulation for Cr MA | Fe Case

	MA Sub-Region			Fe-C Sub-Region	
	Cr	Fe	C	C	Fe
Wt%	61.0	30.3	8.7	0.0011	balance

Table 7: Overall Compositions (wt%) at $T= 1280^{\circ}\text{C}$ for Cr MA-Fe Case for DICTRA Simulation

Fe	Cr	C
99.487	0.449	0.0640

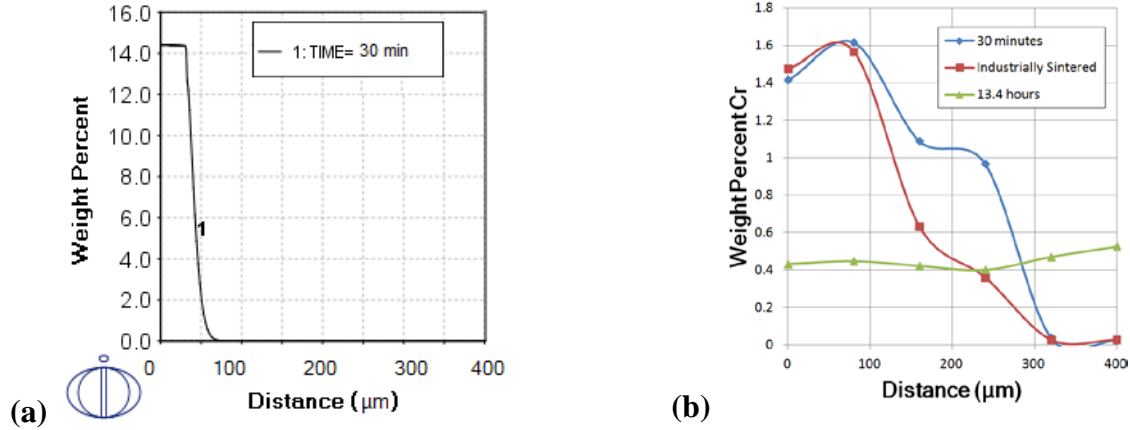


Figure 31: a) Cr Profiles obtained from DICTRA and (b) WDS Point Quantification

Figure 31 a) corresponds to the Cr MA DICTRA concentration profile output while Figure 31 b) corresponds to Cr profiles obtained from compiling WDS point quantification over a distance of 400 μm . As for the WDS profiles, it must be emphasized that across a 400 μm distance, multiple sources of Cr have inevitably been scanned. This can be interpreted as what contributes to the peak that is observed between 175 μm and 225 μm at 30 minutes of sintering. As Figure 31 a) is with respect to a single Cr MA source, a direct comparison cannot be made between the DICTRA simulation output and that of the experimental line data. However, it is interesting to observe that although Figure 31 a) pertains to a single Cr MA source, its concentration profile at 30 minutes is significantly higher than that of the experimental which corresponds to multiple sources. Intuitively, it is thought that by scanning across multiple sources of Cr MAs would produce an overall concentration profile that is higher than scanning across a single Cr MA source, however, quite the opposite is observed. Experimental results in Figure 31 b) show a

more intensified diffusion behaviour as after being sintered for 30 minutes as Cr is detected to be at a peak of just over 1.6 wt% although starting initially at 61 wt%. When observing the simulated results and experimental, the simulated profile is consistently greater than that of the experimental; once again, despite pertaining to a single Cr MA. As for the experimental sintering treatment, after being sintered for 13.4 hours, the Cr concentration fluctuates between 0.4 and 0.55 wt%. DICTRA results for 2.5 hours and 13.4 hours are unavailable as these simulation times could not be completed due to the software taking unreasonably long amounts of time to compute, to the point where the simulation appeared to perhaps have frozen.

Aside from a different number of sources, significant differences exist between experimental plots and computational results obtained through DICTRA. In particular, this corresponds to the much slower diffusion that appears to occur in the simulation case. This can perhaps be attributed to the lack of including diffusion enhancing parameters in DICTRA such as dislocation assisted diffusion and grain boundary diffusion [54]. When grain boundary and dislocation-assisted diffusion parameters were tried and turned on, the simulations would unexpectedly freeze or terminate and as a result, could not be incorporated into the simulation.

Simulation for Sintering Mn Master Alloy (Mn MA)

Case Study 1 for investigation b): Mn MA attached to Fe matrix (Mn MA | Fe)

Table 8 contains initial composition details that were entered into DICTRA while Table 9 contains calculated composition values that the entire system should attain upon complete homogenization.

Table 8: Initial Compositions (wt%) for DICTRA Simulation for Mn MA / Fe Case

MA Sub-Region			Fe-C Sub-Region	
Mn	Fe	C	C	Fe
76.0	17.2	6.8	0.0011	balance

Table 9: Overall Composition (wt%) at T= 1280°C for Mn MA / Fe Case for DICTRA Simulation

Fe	Mn	C
99.3419	0.604	0.0541

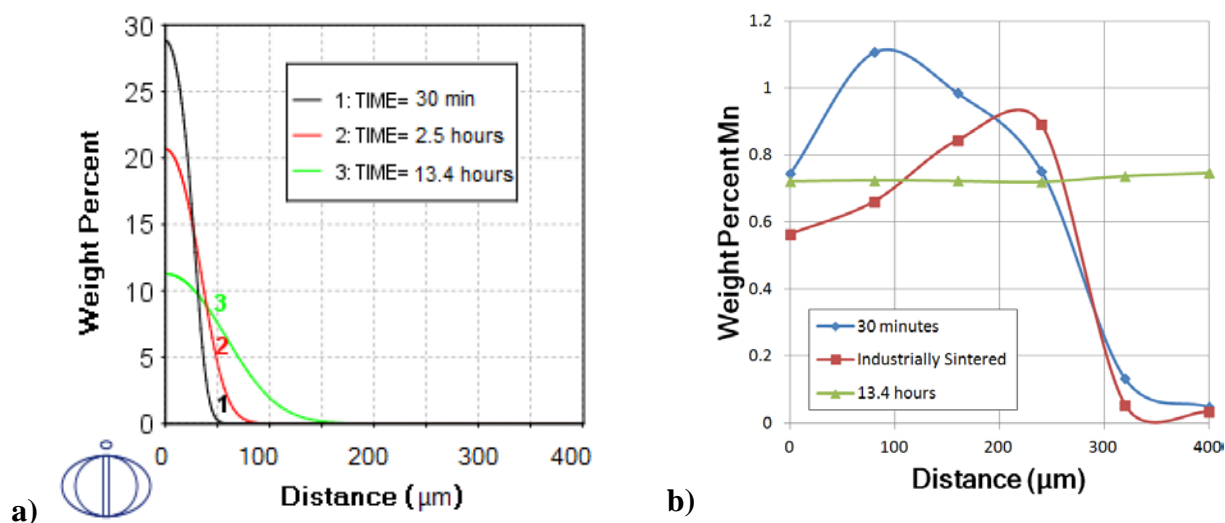


Figure 32: Mn Profiles obtained from DICTRA and (b) WDS Point Quantification

DICTRA results in Figure 32 a) show that 30 minutes into sintering at 1280°C, Mn concentration in the original MA particles drops by more than half, from 76 wt% to a peak of 28 wt%. In Figure 32 b), after sintering for 30 minutes, the initial 76wt% Mn MA particle's concentration has dropped to a peak of 1.1 wt%. After undergoing a full industrial sintering process, the experimental Mn concentration fluctuates up to 0.9 wt% while that of the simulated case still embodies a peak concentration value of just over 20 wt%. After undergoing a sintering time of 13.4 hours, the experimental profile is rather consistent and hovers about 0.7 wt%, a value much

closer to the specified overall Mn composition of 0.6 wt% instead of the single Mn MA profile seen for this time with a peak of 11.5 wt%.

The relationship between computational and experimental results are quite contrary to the SEM-DICTRA comparison of the work of Shykula et. al. [44]. In this case, the simulation portion of the comparison applied to a Fe-40Mn-10Si-C master alloy particle and an Fe particle, both 50 μm in width. Experimental quantification results that were analyzed via EDS agreed well with DICTRA profiles, particularly for Mn despite the fact that at the time, parameters such as grain-boundary and dislocation-assisted diffusion were not included in the simulation [44].

A significant difference exists between DICTRA simulations and WDS plots. This corresponds to how the single MA simulation results are characteristic of overall higher concentration profiles than those of the multiple MA sources. In comparison to DICTRA results, the WDS profile particularly at the industrially sintering time is much more typical of overall Mn content of 0.6 wt% as previously specified. DICTRA can be a powerful tool for PM simulations as it provides a platform to analyze the performance of various MA compositions in terms of chemical homogenization time. However, as seen in cases between DICTRA and experimental analyses via WDS, the unrealistic diffusion profiles of elements in DICTRA prohibit one from quantitatively relying on the software for MA performance prediction.

Simulation for Sintering Cr in Pure vs. Master Alloy (MA) Form

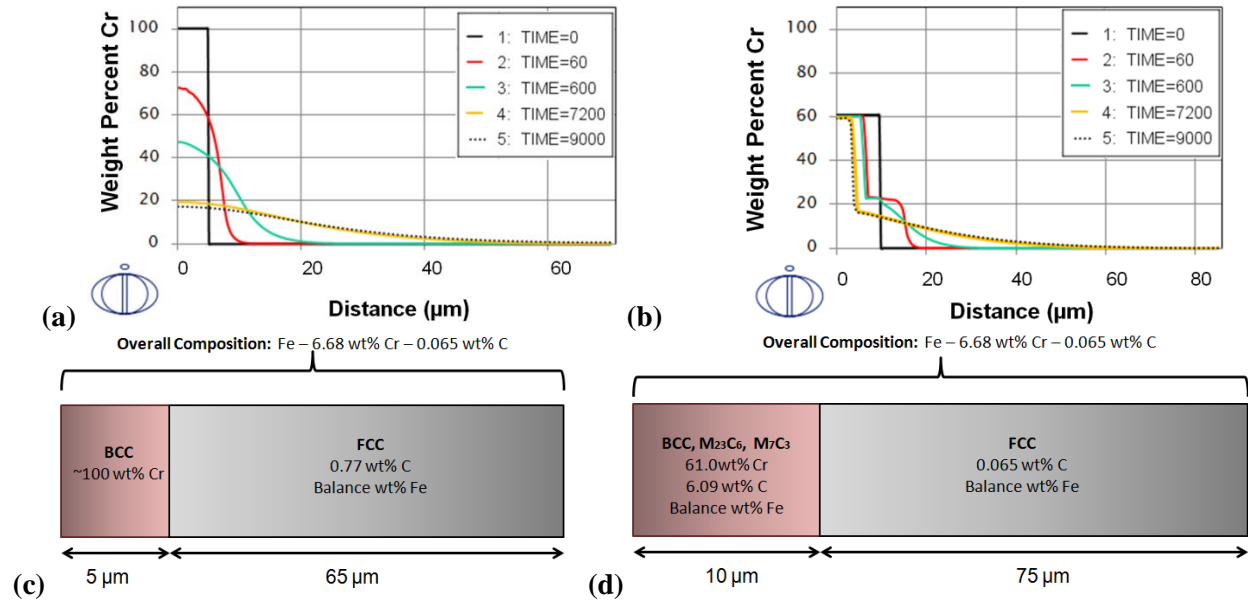


Figure 33: Cr Profiles from (a) Pure Cr / FeC and (b) Cr MA / Fe DICTRA Simulation (all time values are in seconds and sintering $T = 1280^{\circ}\text{C}$). Simulation details: (c) Pure Cr / FeC DICTRA set-up (d) Cr MA / Fe DICTRA set-up

As seen in Figure 33 a) and b), simulation of a pure Cr MA attached to a Fe matrix versus a Cr MA attached to an Fe matrix was also done in DICTRA. Figure 33 c) and d) contain simulation details for each case. Vertical lines seen in composition profiles can be attributed to boundaries between phases. Upon verifying in DICTRA, the vertical boundary seen in the Cr profile at a distance of 5 μm after being sintered for 9000 s (2.5 hours) in Figure 33 b) corresponds to a (M₇C₃ / FCC)-(FCC) interface. This same time in the case of pure Cr is not associated with any phase boundary, instead the entire system had homogenized to FCC. Cr is therefore said to have diffused effectively in pure form, however it is well known that a high affinity of chromium to oxygen would significantly alter this behaviour in an industrial setting [48]. The high affinity of manganese to oxygen is also a reason why Mn is not added into PM steel in its pure form.

Keeping this in mind, other delivery forms were investigated for these alloying elements in this second case study set. Cr and Mn diffusion was observed when being simultaneously delivered in two other forms as seen in Figure 34 and Figure 35.

Simulation for Sintering Multi-component Sources

Case Study 2 for investigation a): Multi-component Master alloy (Cr Mn MA) sandwiching an FeC block (Cr Mn MA | Fe C | Cr Mn, MA)

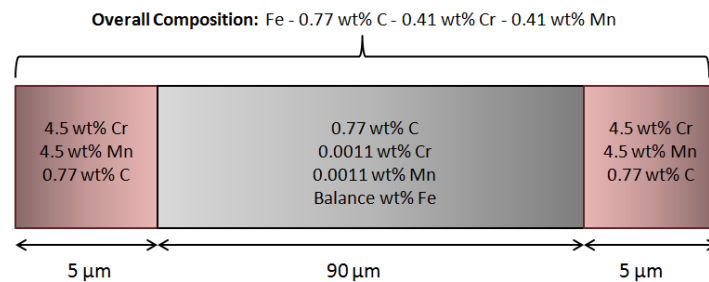


Figure 34: Composition Details for DICTRA Simulation of Cr, Mn MA | FeC | Cr, Mn MA

Case Study 2 for investigation b): Individual Master alloys of Cr and Mn attached to either side of an iron-carbon particle (Cr MA | Fe C | Mn MA)

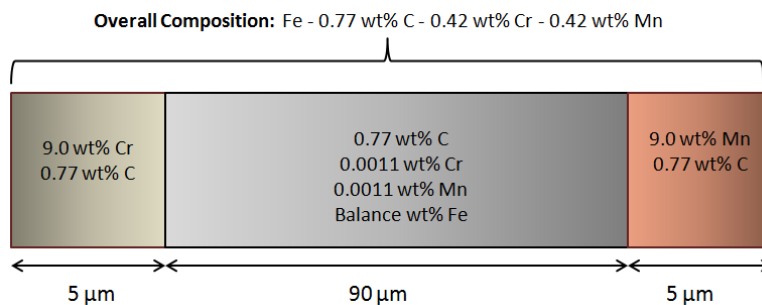


Figure 35: Composition Details for DICTRA Simulation of Cr MA | FeC | Mn MA

Given the significant differences observed between simulation and experimental profiles in case study 1, it is not recommended to rely on DICTRA's exact quantitative values for MA performance prediction. However, from a conservative semi-quantitative perspective, the profile trends can be deemed acceptable.

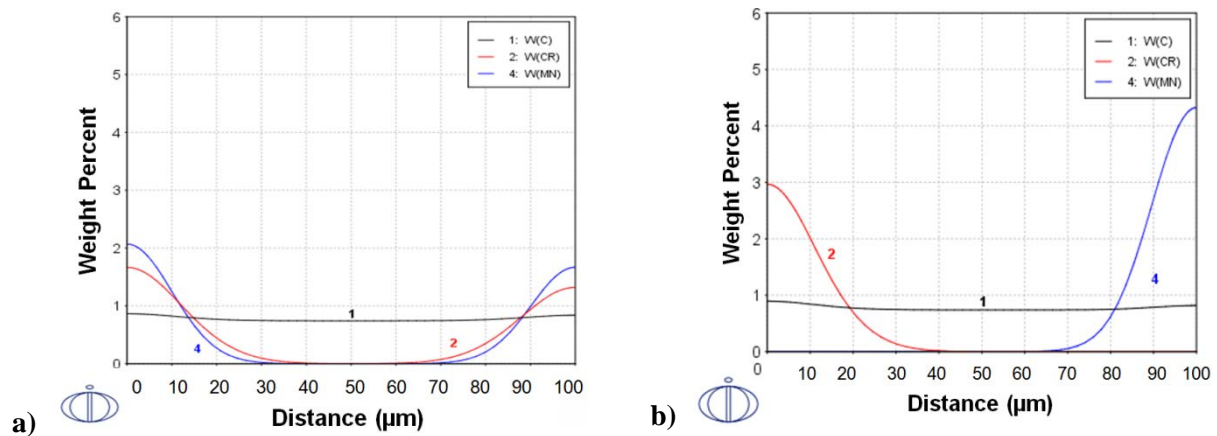


Figure 36: Compositions after being sintered for 30 minutes at 1280°C for a) MMA and b) SMAs sandwiching an Fe-C particle

Figure 36 a) and b) contain concentration profiles for Cr, Mn and C in each MA case after being sintered at 1280°C for 30 minutes. DICTRA results in Figure 36 a) show that after sintering the MMA, the initial particles of 5 μm width originally containing 4.5wt% of Cr and 4.5 wt% Mn reduce in concentration by more than half to just under 2.0 wt% for both elements and extend in the form of a smooth profile to approximately 30 μm inwards on each end. No alloying elements have alloyed the central 20 μm distance (between 40μm to 60 μm). Furthermore, although the initial set-up geometry was symmetrical about the centreline of the system, concentration profiles of the elements no longer exhibit symmetry; this may be attributed to discrepancies in the computational grid. As for Figure 36 b), the same 40μm to 60μm central region remains

unalloyed by Cr and Mn while the first 40 μm of the left side of the system has been affected by Mn and the same distance on the right side of the system has been affected by Cr.

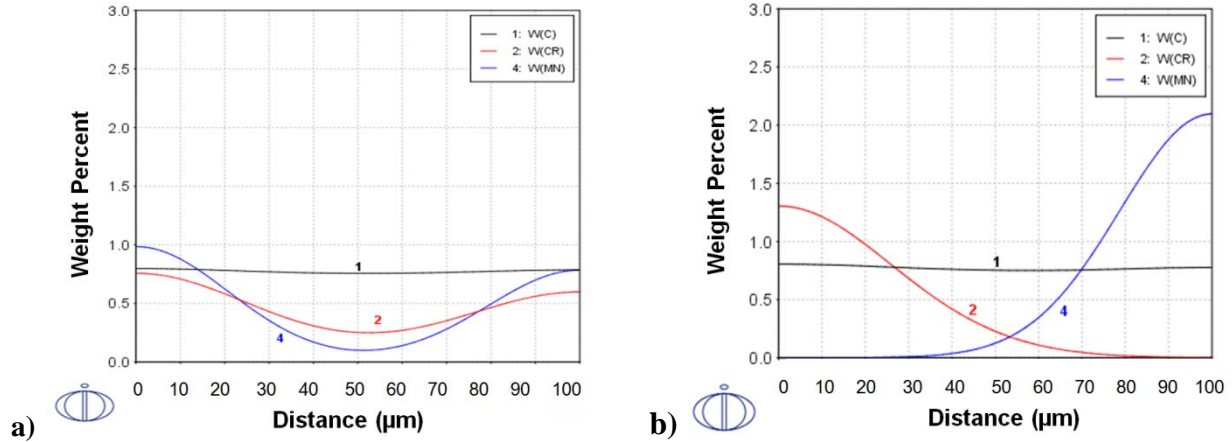


Figure 37: Compositions after being sintered for 2.5 hours at 1280 $^{\circ}\text{C}$ for a) MMA and b) SMAs sandwiching an Fe-C particle

As for sintering at 1280 $^{\circ}\text{C}$ for 2.5 hours, Figure 37 a) shows that the Cr and Mn of the MMA has diffused through the entirety of the system, although not to a completely homogeneous extent. As for Figure 37 b), Cr and Mn have diffused further in on both ends of the system; Cr diffusing to a total distance of approximately 90 μm while Mn reaching a total distance of approximately 80 μm . It is interesting to notice that although Mn appeared to diffuse faster in WDS maps in Figure 30, Mn has a larger modulation than Cr. Based on previous literature, in the case of Mn, it is hypothesized that this larger modulation is due to the fact that the DICTRA simulation does not incorporate manganese's primary method of homogenization (through vaporization, filling of pores, enveloping Fe surfaces and then into grains) [12], [53].

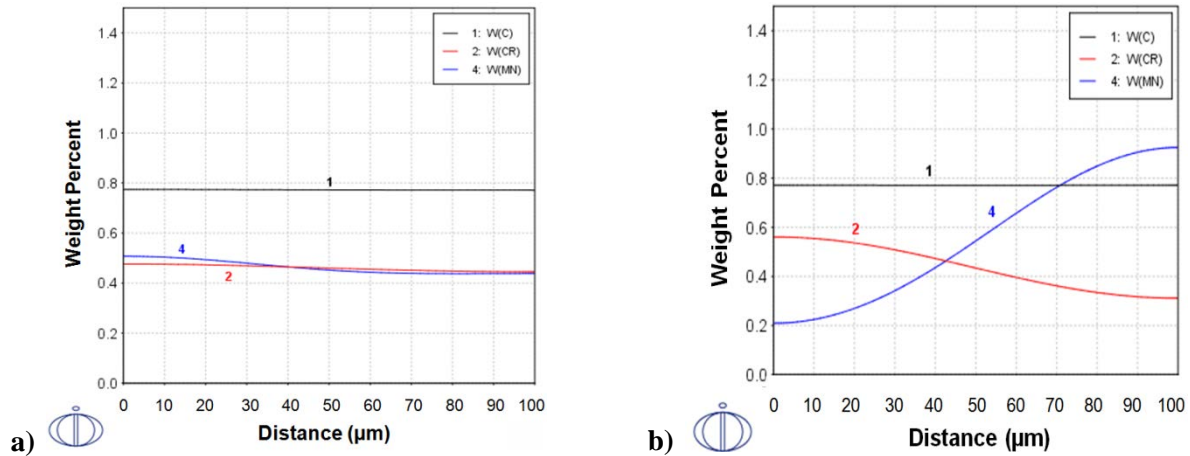


Figure 38: Compositions after being sintered for 13.4 hours at 1280°C for a) MMA and b) SMAs sandwiching an FeC particle

After being sintered at 1280°C for 13.4 hours, Figure 38 a) shows that the MMA system has resulted in a nearly complete homogenization as both Cr and Mn fluctuate between a tight 0.4 wt% to 0.5 wt% range. The entire system has been well alloyed. Once again, the slower diffusion behaviour of Mn is exhibited in both cases, potentially due to exclusion of manganese's vapour transport [53], and is much more noticeable in the case of the SMAs. In the case of Figure 35 b), although the entire system has been alloyed by both Cr and Mn, much larger compositional modulations exist. Cr varies between 0.3 wt% to 0.55 wt% while Mn varies between 0.2 wt% to 0.9 wt%. Keeping this in mind, overall, the use of MMAs are recommended over SMAs as they semi-quantitatively display superior homogenization capabilities for multiple alloying elements.

DICTRA Limitations for Homogenization Studies in PM

Overall, such homogenization simulations require a software package capable of calculating equilibrium in the real-time; with an appropriate partial differential equation (PDE) solver that links to well-equipped thermodynamic databases. In this sense, DICTRA is irreplaceable,

however it is worth discussing the limitations of this software package which were discovered in this research. A 64-bit version of DICTRA software was installed onto a Windows desktop computer with a Pentium 4 processor. Despite meeting and surpassing the criteria of "4 GB of RAM for reasonable performance" [57], DICTRA simulations failed to complete in a reasonable timeframe. Limitations of DICTRA for homogenization studies in the PM realm include an inability to accurately incorporate complexities associated with a typical PM microstructure such as porosity and ranges in particle sizes. In addition to this, other modes of diffusion that are prevalent in PM systems either cannot be included within DICTRA simulations or are included but unambiguously specified as to how they should be incorporated. This includes vapor-transport mechanisms and grain boundary diffusion. For example, as for grain boundary diffusion, DICTRA requires a user to input the fraction of grain boundaries for the system under simulation as well as fraction of activation energy required for grain boundary diffusion. However, the fraction of grain boundaries do not remain constant during sintering and the fraction of activation energy which is suggested to be entered (0.5) is not clearly justified.

Part III: Multi-Component Master Alloys for Low-Temperature Liquid

Phase Sintering

Chapter 6: Computational Algorithm for Selection of Multi-Component Master Alloys for Liquid Phase Sintering (LPS)

Master alloys: equilibrium and as-solidified states

Let us imagine that it is intended to employ PM to fabricate steel containing C, Cr and Mn. In the case of incorporating carbon, a traditional and invariable way is to use a graphite powder. In the case of metallic additions, there are at least three possibilities. Firstly, chromium and manganese can be taken as pure elements. Secondly, iron can be pre-alloyed with them. Thirdly, master alloys (MA) containing Cr and Mn can be utilized. Each approach has its merits and demerits. Manganese and, to a lesser extent, chromium are volatile metals, which may result in losses if sintering is conducted at high temperatures. Pure Mn is very prone to oxidation, which may necessitate expensive protective atmospheres. Since pure iron is a ductile metal, a usage of its powders ensures a good compactability; in contrast, particles made of iron alloyed with Cr and Mn may be less deformable, which may result in an unacceptably low green body density [12], [13], [14]. It is therefore worthwhile to investigate Cr and Mn-rich MAs.

Example 1: Cr-rich master alloy

An advantage of using MAs cannot be sensibly commented upon without specifying their compositions. Let us start with a Cr-rich MA (Cr MA) and assume, for the sake of determinacy and illustrative purposes, that it, in addition to iron, contains 61wt% Cr and 8.7 wt% C. Such a high concentration of carbon suggests that in Cr MA, chromium is present not as a pure metal, but as a carbide or a mixture of carbides. Let us assume that sintering is carried out at 1280°C. According to thermodynamic computations performed using TCFE8 database in Thermo-Calc at this temperature, Cr MA contains 98wt% M_7C_3 and 2wt% FCC. As previously studied using DICTRA one may also similarly model processes happening during sintering with those transpiring in a diffusion couple; one end of which is the two-phase Cr MA while that of the other is pure iron. It should be understood that such an approach is based on an assumption that the Cr MA is in the equilibrium state at 1280°C prior to sintering. A refined approach involves understanding that in industry, MAs are frequently fabricated by solidification of melts. A state of MA after freezing is therefore a non-equilibrium one. As a result, after a MA is heated to a sintering temperature of T_{sint} ; in fact, post-freezing microstructural features will be inherited.

Let us elaborate by considering a slow solidification of a ternary Fe–C–Cr melt containing 61wt% Cr and 8.7 wt% C. A vague term "slow" merely means that no special attempts are undertaken to extract a heat of solidification very quickly, that the melt is either allowed to solidify in a pot or it is poured on a non-chilled surface instead of being atomized or sputtered. Such a mode of solidification, which is natural from the industrial angle, can be realistically modelled using Gulliver–Scheil formalism [38]. An outcome of the modelling is shown in Figure 39.

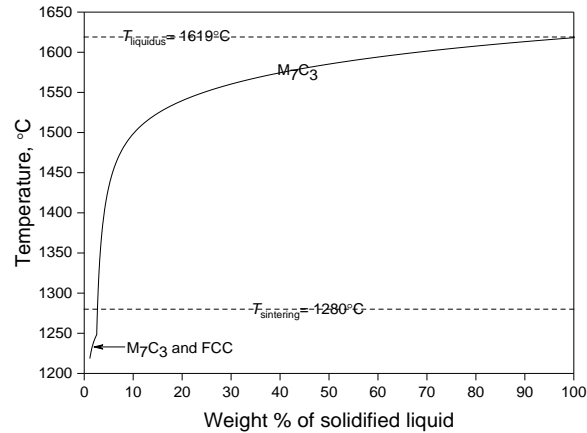


Figure 39: Solidification Path of the Fe-61 wt% Cr - 8.7 wt% C melt

According to Figure 39, solidification commences at 1619°C with M_7C_3 as the primary phase. Remarkably, when temperature decreases to 1280°C, an industrially employed sintering temperature, the system still contains approximately 2.5wt% of the liquid phase.

If Cr MA is gradually heated to 1280°C, it is hypothesized that partial melting will yield the same percentage of liquid that existed in the system when it reached this temperature in the course of Gulliver-Scheil freezing. Since only 2.5wt% of Cr MA melts, subsequent sintering hardly falls into a category of liquid-phase sintering (LPS), but a reappearance of liquid is what this contribution revolves around.

Example 2: Mn-rich master alloy

If Mn-rich master alloy (Mn MA) with 76 wt% Mn, 6.8 wt% C and Fe, then at 1280°C its equilibrium phase portrait is 56 wt% of liquid and 44 wt% of M_5C_3 . If, however, the melt having Mn MA's composition is solidified and then heated up to this temperature, then, as Figure 37 indicates, it will contain 63wt% of liquid.

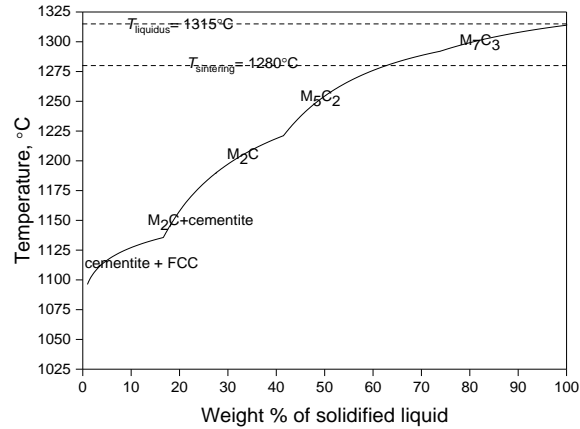


Figure 40: Solidification path of the Fe-76wt% Mn 6.8wt% C melt

These two simple examples emphasize that it would not be as accurate to treat MAs in the beginning of sintering as equilibrium entities. Instead, possible processes within them should be analyzed without forgetting their fabrication history, which frequently and inevitably includes freezing from the liquid state. Chemical compositions of Cr MA and Mn MA chosen for illustrative purposes can be altered. In particular, it can be endeavoured to find such concentrations of C, Cr and Mn that a significant percentage of liquid forms at a sintering temperature. Such an attempt would be justified if, for a specific situation, it is deemed advantageous to trigger LPS.

Certainly, nothing prevents one from trying to alter the compositions of Cr MA and Mn MA to increase the percentage of liquid at a sintering temperature. Also, nothing precludes one from considering a mixed MA (MMA) containing both chromium and manganese and attempting to establish a range of promising compositions facilitating LPS. If such a range exists, and if a fabrication of corresponding MMAs is practical, then Cr and Mn can conveniently be brought into the system at once instead of coming from two individual Cr-containing and Mn-bearing master alloys.

Development of partially or fully melted multi-component master alloys

Since PM steels may include other alloying additions such as Mo, Ni and Si, it is sensible to explore a solidification behavior of a corresponding multicomponent melt for various concentrations of carbon and metallic elements. By repeating Gulliver-Scheil simulations for different compositions using Fortran and computational thermodynamics (Thermo-Calc), a percentage of remaining liquid, f_{sint} , at a sintering temperature¹ can be evaluated.

Thermo-Calc and Fortran Algorithm

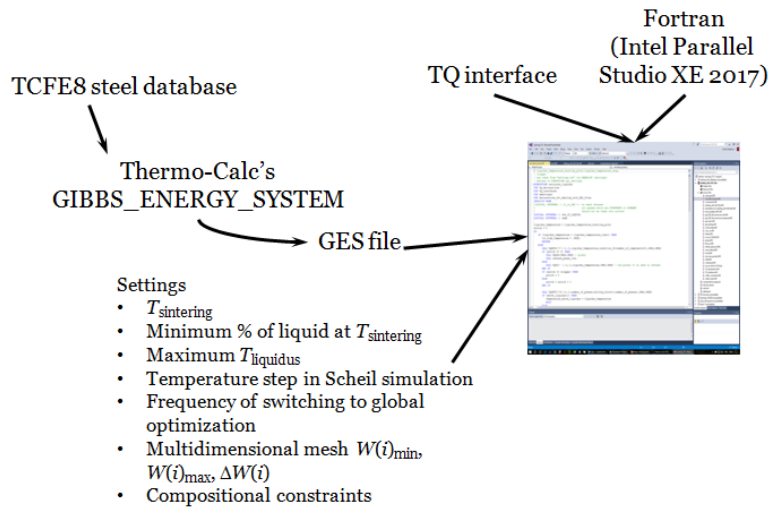


Figure 41: Schematic for Thermo-Calc - Fortran Program

Fortunately, the TC team developed TQ-interface, which is a library of core TC subroutines and functions accessible from within Fortran. An ability to combine a computational might of TC implemented in TQ-interface with a flexibility of a problem-oriented Fortran code enabled the

¹ of course, it may be quite different from 1280°C in the examples considered

development of a program capable of finding promising compositions of multi-component master alloys. Before presenting examples of specific compositions found in various systems, it is warranted to review how the program operates.

1. Once a list of components in a system of interest is defined (the list must include Fe and C plus at least one more component), TC is used to extract data from an appropriate database and save them as a binary (non-editable) file, which, in TC jargon, is called GES file.
2. The program initiates TQ-interface and retrieves information from the GES file.
3. For each component (except Fe), a mesh of weight percentages is defined in an input file by specifying lower and upper limits along with a step. When this is done for all components, there exists a multidimensional grid of knots. Of course, a user can easily re-define this grid by altering limits and steps.
4. It might be senseless to investigate solidification behavior at certain knots, because MMA may not be compositionally balanced at them. For instance, it would be counterproductive to consider knots in which $\text{wt\% Mo} \gg \text{wt\% Mn}$ or in which wt\% Fe is too low or too high. The program allows the user to introduce compositional constraints in an input file using a simple syntax recognized by the program. For instance, the lines

$\text{Mn Mo} > 2$

$\text{Mn Cr} > 0.8$

$\text{Mn Cr} < 1.25$

mean that wt\% Mn should be at least two times greater than wt\% Mo , and that wt\% Mn and wt\% Cr should not be too dissimilar. Of course, it is up to the user how to define

compositional constraints or whether to use them at all. Whatever a decision, it must take into account particularities of the problem in hand. Although the program does not assist the user in making a right choice, it provides a computational freedom to express needs.

5. If compositional constraints are satisfied at a knot, then the liquidus temperature is calculated. If $T_{\text{liq}} > 1600^{\circ}\text{C}$, then a corresponding composition of MMA is inadmissible.
6. If $T_{\text{liq}} \leq T_{\text{sint}}$, then at sintering temperature the master alloy will completely liquefy at sintering temperature, which makes it suitable for LPS. A composition of this MMA is recorded in an output file along with T_{liq} .
7. If $T_{\text{sint}} < T_{\text{liq}} \leq 1600^{\circ}\text{C}$, then the program proceeds with Scheil's simulation and calculates a percentage of remaining liquid at the sintering temperature, f_{sint} . If this fraction is less than a threshold defined in an input file (obviously, a numerical value of the threshold can be effortlessly changed by the user), then a corresponding composition of MMA is unacceptable. Otherwise, a composition of this MMA is recorded in an output file along with T_{liq} and f_{sint} .

The output file generated by the program typically contains multiple entries corresponding to "promising compositions". By tightening compositional constraints and increasing the threshold for f_{sint} prior to executing the program, a number of possibilities can be reduced. This, however, is neither needed nor recommended. Since program's output is an ASCII file with blanks as delimiters, it can be effortlessly exported to Excel or any other software capable of filtering and

ordering worksheets. For instance, one may examine only MMAs for which $T_{\text{liq}} < 1400^{\circ}\text{C}$, wt%

$\frac{\text{Mn}}{\text{Cr}} > 1$, wt% $\frac{\text{Mn}}{\text{Mo}} > 3$ and wt% $\frac{\text{Cr}}{\text{Mo}} > 2$, without repeating the calculations.

Selection Criterion and Results

Since PM steels may include other alloying additions such as Mo, Ni and Si, it is sensible to explore a solidification behavior of a corresponding multi-component melt for various concentrations of carbon and metallic elements. In order to develop these partial and fully melted multicomponent MAs, a series of criterion were formulated. By repeating Gulliver-Scheil simulations for different compositions, a percentage of remaining liquid, f_{sint} , at a sintering temperature² can be evaluated. If it is sufficiently high (this is the **first** criterion to be satisfied), then a number of additional criteria should be considered.

Obviously, a solidification of MA from the liquid state implies that the liquid state exists. Regardless of composition, this state can always be attained by increasing temperature above liquidus temperature, T_{liq} . If T_{liq} is "too high", then it might be technologically and economically challenging to make the melt. Also, a significantly elevated temperature may result in a high vapor pressure of one or several components (Mn, for instance); consequently, an actual composition of the liquid phase may deviate from the target. In order to quantify an ambiguous term "too high", let us recall that a certain temperature, namely 1600°C , is frequently seen in

² of course, it may be quite different from 1280°C in the examples considered

publications on iron and steel making as well as in many exercises and problems in textbooks on thermodynamics and high-temperature materials production. This, of course, is a reflection of the fact that many processes are conducted in the vicinity of 1600°C, that many companies and research facilities deal with this temperature confidently and comfortably. The aforementioned challenges start emerging above this temperature and then transform in serious obstacles when temperature approaches 2000°C. These considerations lead us to the **second** criterion demanding that $T_{liq} \leq 1600^\circ\text{C}$.

Let us take MMA containing 5%C, 10%Cr and 10%Mn. It can be mixed with such amounts of iron and graphite powders that an overall composition of a green body would be 0.5%C, 0.5%Cr and 0.5%Mn. Despite this, the MA in hand should not be seriously considered as the mixture has 5% of MMA. This percentage is unacceptably high, because carbides that MMA is mainly made of are abrasive, which will result in a quick deterioration of tools including compaction dies. Carbides are brittle, but essentially undeformable, which may adversely affect the compactability of the Fe–graphite–MMA mixture. The **third** criterion is that a mixed master alloy must be rich in alloying addition.

Let us recall that the usage of a single MMA implies that all elements³ are put in a blend at once. Imagine that according to specifications, the following inequalities must be enforced: $0.4 \leq \text{wt\% Cr} \leq 0.6$ and $0.4 \leq \text{wt\% Mn} \leq 0.6$. Obviously, MMA containing, for instance, 70% Mn and 15%

³ except of carbon, which can always be added as graphite

Cr cannot be employed. The **fourth** criterion demands that MMA should be so balanced that an overall chemical composition of a PM material is attainable.

To introduce further criteria, it should be realized that a slow solidification results in a large ingot, which must somehow be broken into small particles. Typically, in the production of PM materials, the size of MA particles does not exceed 40 μm . Keeping this in mind, let us consider MMA with 1%C, 30%Cr, 30%Mn, 10%Mo and 5%Si. Even without thermodynamic calculations, it intuitively is clear that a fruit of solidification does not contain much carbides whose abundance would suggest that the ingot is brittle. If so, the **fifth** criterion states that the concentration of carbon should not be so low that the solidified substance is difficult to disintegrate in small pieces. This criterion should not be applied blindly, because a possible formation of intermetallics also makes an ingot brittle. For instance, a solidified MMA with the composition specified above contains 14% of Laves phase and 3% of σ -phase, both of which are known to be brittle. Without an access to specialized software and databases tailored for ferrous systems, it might be difficult to judge what intermetallics form and what their percentages are. In the case of carbon, a simple assumption that if concentration of C exceeds 3%, then an ingot is destructible typically works quite reliably.

The **sixth** criterion stating that the concentration of carbon should be coordinated with percentages of metallic additions rests on a simple fact that while carbon cannot be selectively taken from an already made mixture, graphite powder can always be added to it. For example, an exotic MMA containing 26%C, 28%Cr, 28%Mn, 14%Si and 4%Mo cannot be employed for

fabricating a PM steel with 0.6%**C**, 0.6%**Cr**, 0.6%**Mn**, 0.3%**Si** and 0.1%**Mo**, because the %**C**/%**Mo** ratio in the master alloy is greater than that in steel. Typically, this not-too-demanding criterion is satisfied if $T_{liq} \leq 1600^{\circ}\text{C}$, *i.e.*, if the second criterion is fulfilled.

The **seventh** and the last criterion imposes a non-obvious condition that a percentage of iron in a MMA should be high enough. In order to understand what this requirement originates from, let us imagine that a melt should be prepared in a crucible, and that the crucible is filled with pieces of graphite and pure metals. Let us consider a sufficiently general situation when metallic components are those from Table 10.

Table 10: Melting points of selected elements

Element	Fe	Cr	Mn	Mo	Ni	Si
$T_{\text{melting}}, ^{\circ}\text{C}$	1538	1907	1246	2623	1455	1405

Since **Mn** increases both hardenability and strength, and since it is relatively cheap, its presence is hardly avoidable. It is a safe assumption that **Cr**, as an element enhancing hardenability, is placed into the crucible as well. **Si** is seldom added deliberately, and even if it is made a part of MMA, its concentration is usually lower than those of manganese and chromium. In the past, **Ni** was routinely used in ferrous PM, but nowadays it is much less prevalent due to health and environment concerns. Even if **Ni** is employed, its concentration in MMA is normally less than percentages of **Mn** and **Cr**. Although **Mo** boost hardenability, it is expensive. Due to this reason, not too many PM steels have a high percentage of **Mo**. Since the third criterion dictates that MMA must be rich, it is clear from the qualitative viewpoint that the crucible mainly contains

Mn, Cr and Mo; it may also contain Ni and Si in much smaller amounts. In addition, the melting pot contains Fe. The third criterion suggests that $\text{wt\% Fe} \leq \text{wt\%Cr} + \text{wt\%Mn} + \text{wt\% Mo}$, but it does not specify the lower limit.

A slow industrial-scale heating of crucible's content will trigger the melting of a metal with the lowest fusion point, which is manganese. This is quite unfortunate, because Mn is a highly volatile element, which is readily oxidizable at elevated temperatures. In fact, a noticeable fraction of solid Mn may transform in MnO even before the melting temperature is achieved. The same can be said about Si, whose oxidation above 400°C cannot be ignored. This suggests that a preparation of a melt that then will solidify in a master alloy should be a two-stage process. At the first step, Fe, C and Mo are placed in the crucible, which is then heated to 1600°C.

Examples of promising compositions suggested by the program

Table 11: Solidification behavior of selected master alloys

Composition, wt.%	$T_{\text{liq}}, ^\circ\text{C}$	$f_{1280^\circ\text{C}}, \%$	$f_{1150^\circ\text{C}}, \%$
3.5C–32Cr–40Mn–24.5Fe	1441	81.5	0
3C–32Cr–38Mn–27Fe	1370	85.3	0
3.5C–24Cr–44Mn–8Ni–20.5Fe	1480	80.2	10.5
3.5C–60Mn–12Mo–24.5Fe	1255	100	73.4
4C–56Mn–8Mo–10Ni–22Fe	1271	100	92.4
3.5C–26Cr–38Mn–12Mo–20.5Fe	1444	83.7	73.3

For realistic compositional constraints, not even a single MMA with $f_{1280^{\circ}\text{C}} \geq 80\%$ was found in the Fe-C-Cr-Mn-Si, Fe-C-Cr-Mn-Mo-Si and Fe-C-Cr-Mn-Ni-Si and Fe-C-Cr-Mn-Mo-Ni-Si systems.

Chapter 7: Powder and Test Bar Fabrication

Powder Production

Table 12 contains information about two MMAs, which were the first two synthesized in this research project (labelled NK and DM). NK and DM alloys are untraditional from the compositional angle, because iron percentage in them is rather low.

Table 12: Properties of MMAs used in this work

Master alloy ID	Intended concentration, wt.%					$T_{liq}, ^\circ C$	$f_{1280^\circ C}, \%$
	Fe	C	Cr	Mn	Mo		
NK	16	4	28	26	26	1521	72
DM	1	3	38	38	20	1475	73

A two-stage process was implemented to fabricate the alloys through arc-melting. Firstly, Fe, C, Cr and Mo were melted, and the system was kept in the liquid state for several minutes. Then the melt solidified in a button-like body on the surface of a water-chilled copper hearth, and pieces of Mn were placed near one side of it. Then the arc stinger began melting the ingot from the opposite side; a rapidly forming liquid covered chunks on manganese, melted and dissolved them. Judging by weight losses, that industrially applicable trick resulted in Mn losses due to evaporation not exceeding 2.7 wt.%. After dissolution of Mn, the liquid was homogenized for several minutes before rapidly freezing on the hearth.

NK alloy was brittle, and DM alloy was very brittle. They were impact-broken into irregular pieces with 1-3 mm characteristic dimension, which then were ball-milled into 50-200 μm power

using 1 cm ZrO_2 balls. Then the size of particles was further decreased through ball-milling with 5 mm ZrO_2 balls. Finally, sieving was employed to collect particles with sizes less than 38 μm . An outcome of those manipulations was a fine dark-gray powder, which was utilized for making PM materials. A summary of the alloy fabrication from arc melting to final powder can be seen in Figure 42 a)-e).

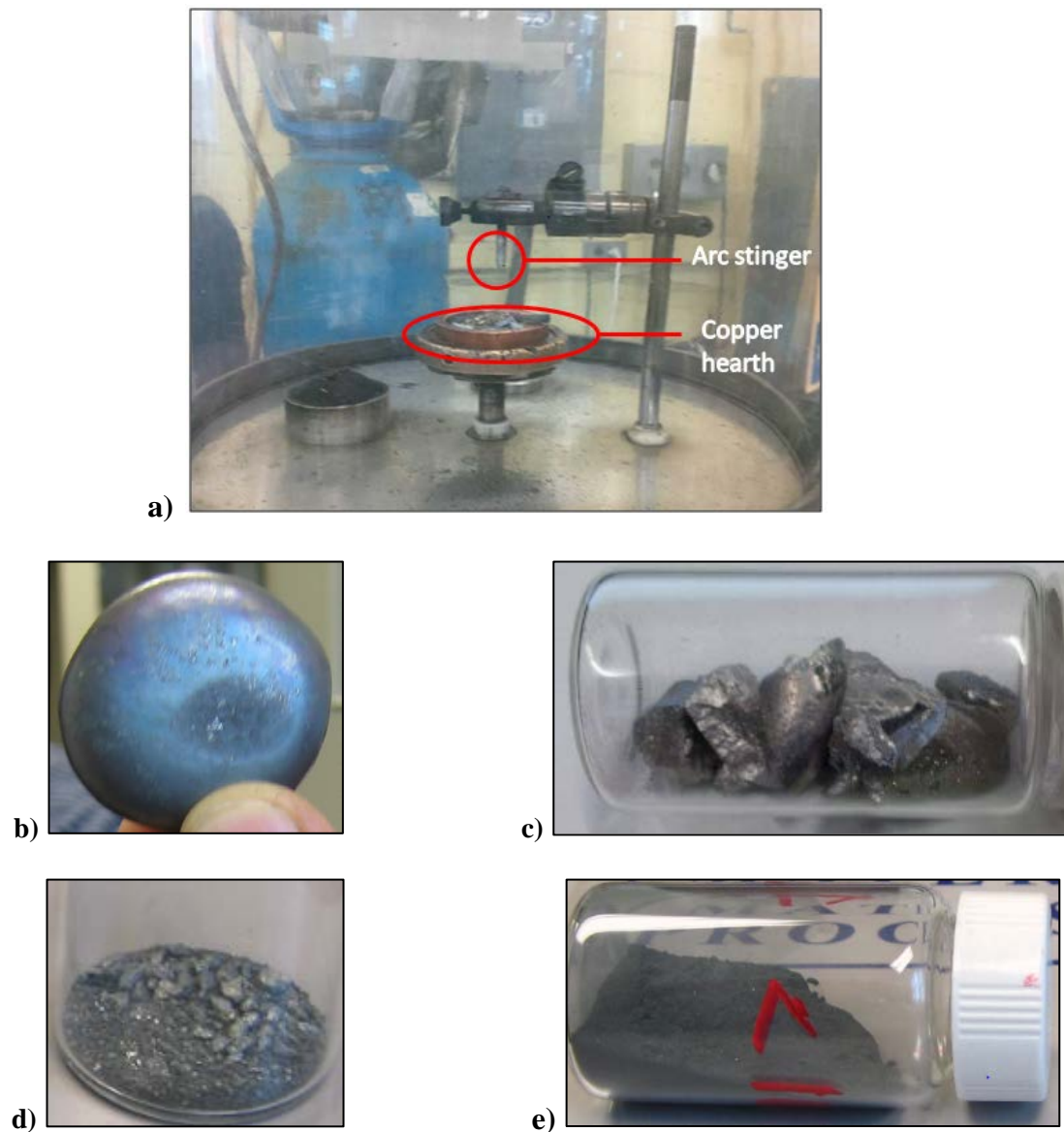


Figure 42: MMA Powder Production: a) arc-melting set-up, b) arc-melted ingot, c) impact-broken ingot, d) particles after preliminary ball milling and e) fine powder after final ball milling

Calorimetric examination

Strictly speaking, the TCFE8 steel database cannot be confidently used to predict thermodynamic properties, in general, and solidification behavior, in particular, of systems with less than 50 wt.% of Fe. A quick calorimetric investigation of NK and DM alloys was therefore undertaken to validate computational results. Ideally, in a differential scanning calorimetry (DSC), a base line should be almost horizontal, which can be achieved by taking such an amount of an inert reference material that its heat capacity will be the same as the heat capacity of the sample.

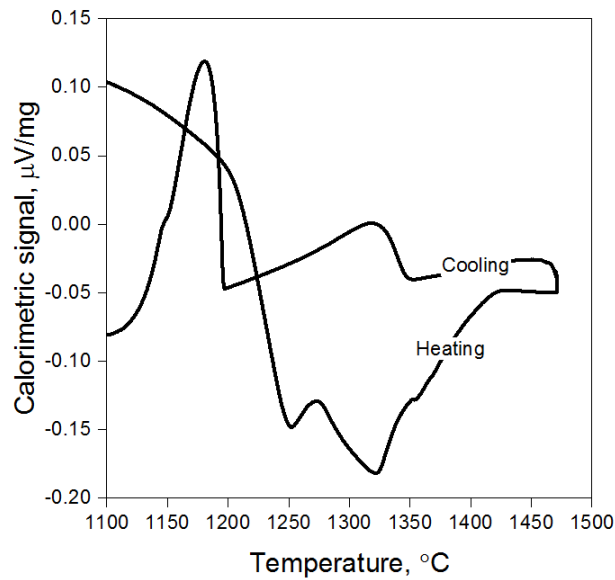


Figure 43: NK, 30°C/min

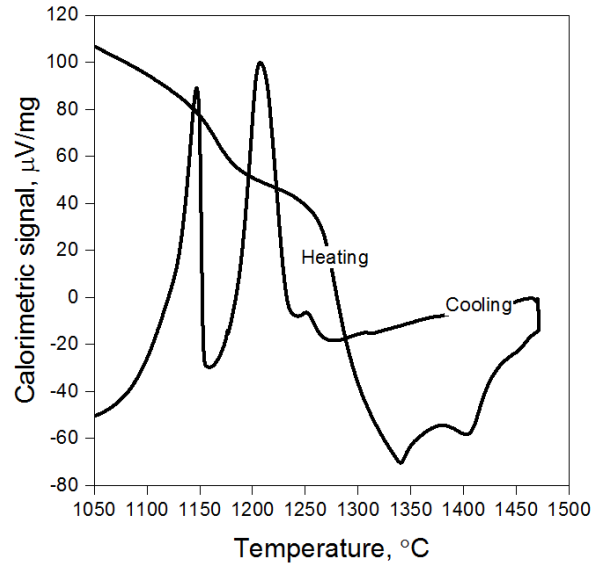


Figure 44: DM, 30°C/min

Base lines (especially those corresponding to heating curves) in Figure 43 and **Error! Reference source not found.** are far from horizontal, but they at least demonstrate regions of regular behaviour. According to the DSC paradigm, an onset of a deviation from a regular pattern should be associated with the beginning of a phase transformation. Apparently, both heating curves hint at thermal events happening below $T_{\text{sint}} = 1280^{\circ}\text{C}$. Since neither carbides nor intermetallic phases are likely to undergo fast transformations, and since a heating rate was deliberately made high to match one typically employed in industrial sintering, these events may correspond to melting. A presence of thermal events above 1280°C suggests that both MMAs melted only partially when T_{sint} had been achieved. As for cooling curves, it suffices to notice that multiple peaks accompanying solidification point to the formation or co-precipitation of multiple phases during freezing.

Test Bar Fabrication

Once NK and DM master alloys were made, they were fabricated into standard TRS (Transverse Rupture Strength) test bars with standard dimensions as outlined in Figure 45. Let us recall that by employing these MMAs, one brings Cr, Mn and Mo into a mixture in a coordinated manner. In order to find whether the usage of a new family of MAs is valid, it was necessary to compare properties of PM steels fabricated in traditional (marked with -T in Table 13) and specialized (-S) fashions.



Figure 45: Sample TRS (Transverse Rupture Strength) PM Test Bar

Table 13: Chemical compositions of PM steels produced in traditional and specialized manners

PM steel ID	Concentration, wt.%			
	C	Cr	Mn	Mo
NK-S	0.75	0.48	0.5	0.07
NK-T	0.73	0.48	0.41	0.37
DM-S	0.73	0.58	0.55	0.27
DM-T	0.73	0.59	0.49	0.25

Chapter 8: Characterization by Microscopy

Scanning Electron Microscopy (SEM) - Wavelength Dispersive X-Ray Spectroscopy (WDS)

As seen in Table 13, although a low concentration of Mo in NK-S should refrain one from its direct comparison with NK-T, compositional maps of Cr and Mn given in the next section are still worth reviewing. Compositional maps obtained through WDS for all PM steels that underwent industrial sintering procedures of sintering at 1280°C are depicted in Figure 46 and Figure 47 respectively. Images in the first row correspond to backscattered electron (BSE) images. The second, third and fourth rows of Figures 43 and 44 contain compositional maps of Cr, Mn and Mo respectively. Upon comparing WDS elemental maps, DM-S displays improved homogenization, particularly for Cr and Mo, in comparison to trends seen in DM-T. As for DM-S, as a lower frequency of unalloyed regions is observed. The larger diffused areas that can be seen in the case of Cr and Mn from original alloying sources in NK-S may be attributed to a slightly larger initial particle size. Areas outlined by a white box highlight large grains that once again are not well alloyed whether by the traditional master alloys or even specialized master alloys. As found by other researchers and as previously discussed in the case of Mn, the element's solid-state diffusion coupled with vapour transport [12], [53] contributes to the better homogenization that is noted in comparison to Mo, Cr and Mn. Poor Mo homogenization that is seen in the WDS maps for NK-T and DM-T can be attributed to the much slower solid state diffusion of Mo in Fe. This also agrees with the Mo diffusivity data seen in Appendix B. Furthermore, in literature, it has been found that Mo homogenizes to a rather small extent with

its lower diffusivity and that Mo-containing particles typically remain undissolved but can be identified as carbides [12].

Although rather unnoticed in NK-S, another phenomena that is hypothesized to be observed in the Mo-map and can be seen in DM-S is the formation of secondary pores at the sites of Mo-containing particles. The formation of secondary porosity is associated with LPS-activating particles. The secondary pores that form are described to be approximately double the diameter of Mo particles from which they originate, as the liquid phase dissolves Fe-matrix material. [12], [58], [59].

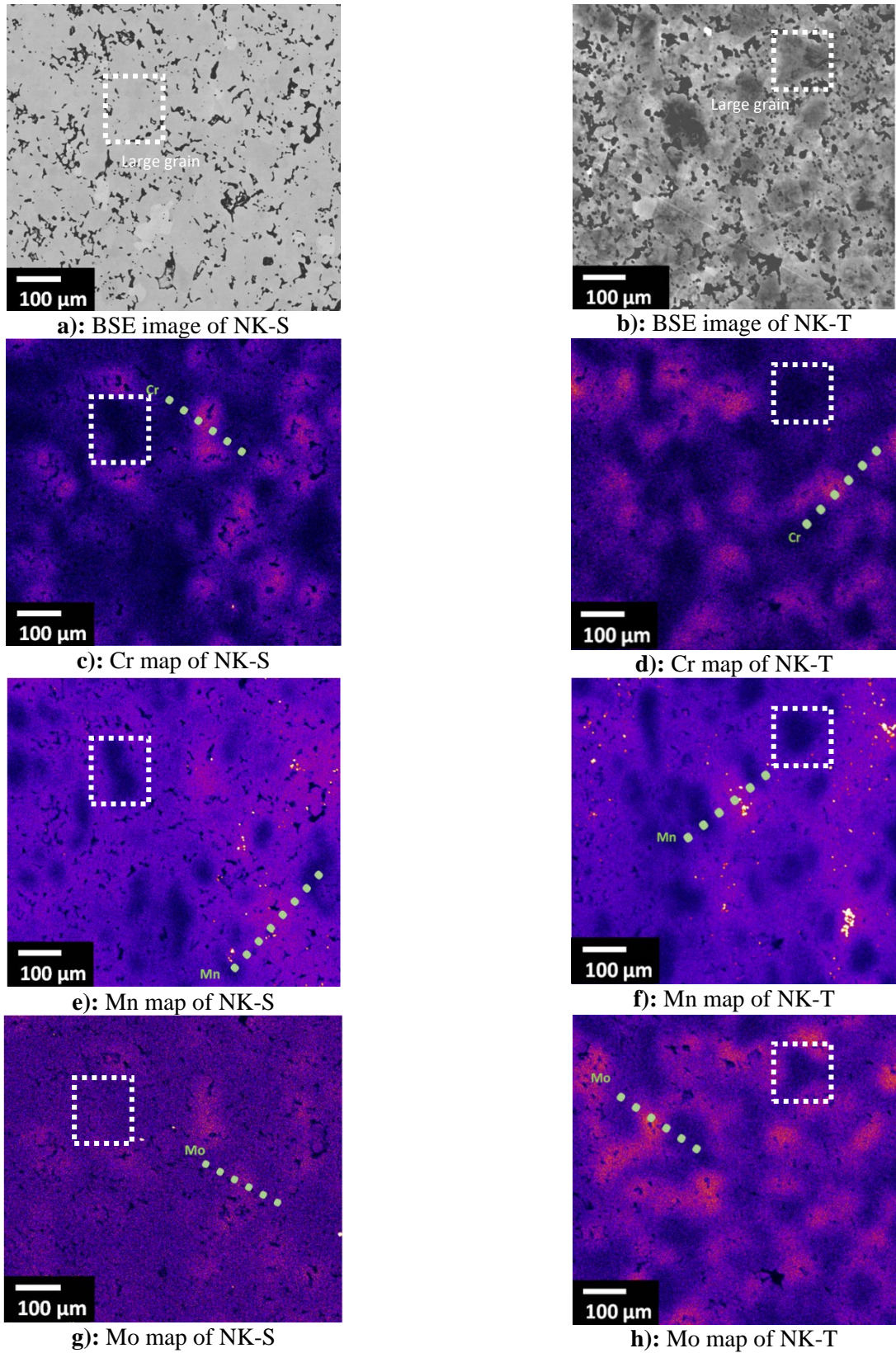


Figure 46: BSE Images and WDS Elemental Maps for NK-S and NK-T (Large grains outlined by a white square)

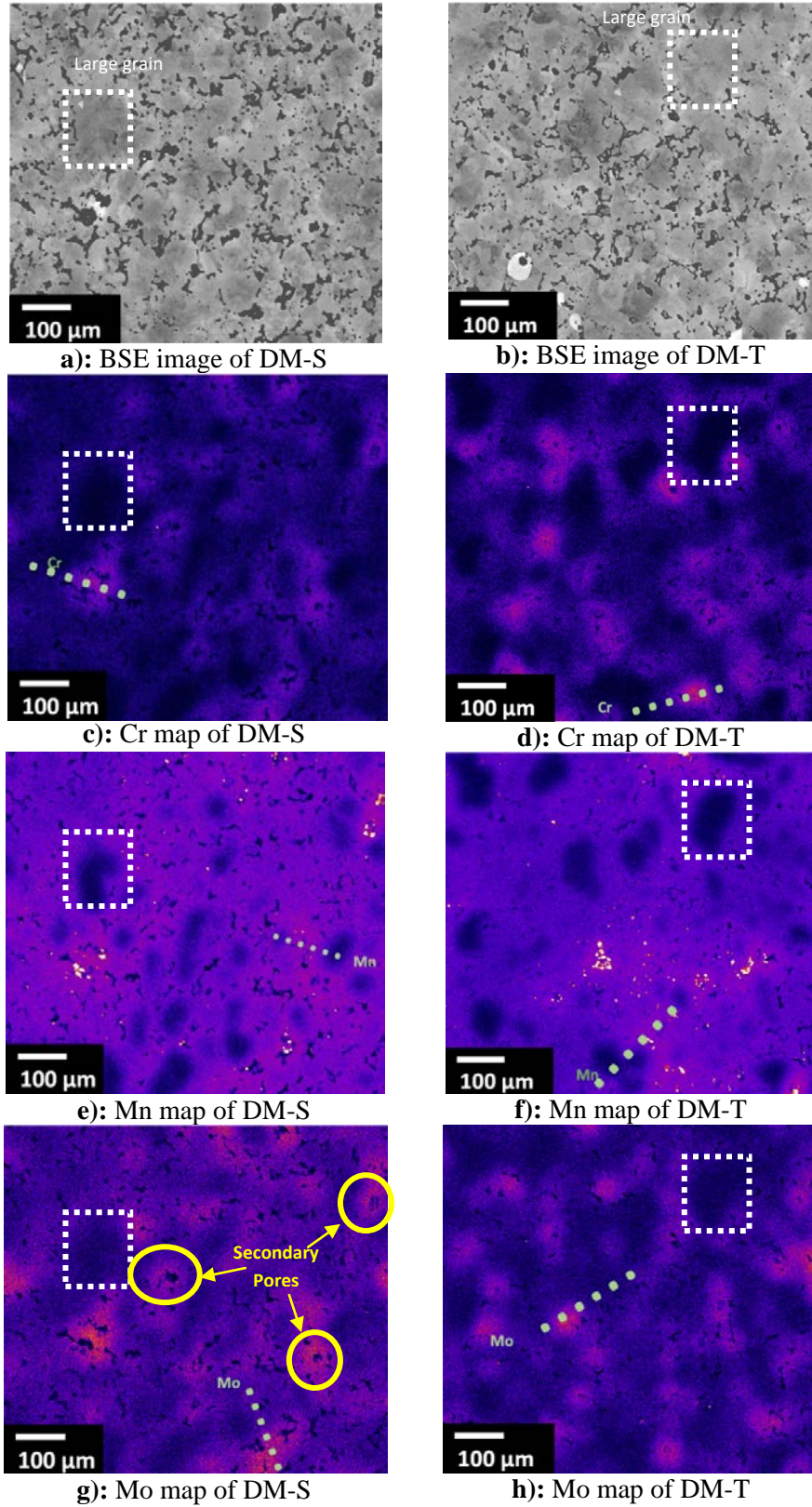
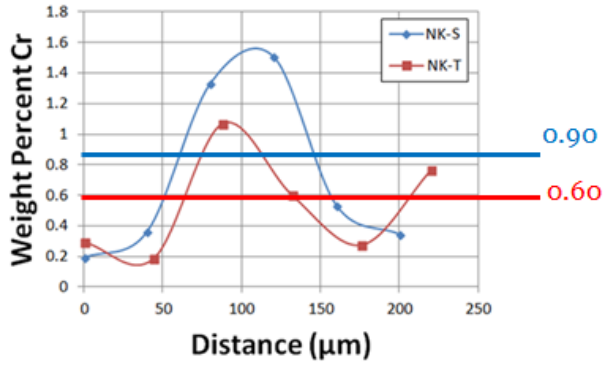
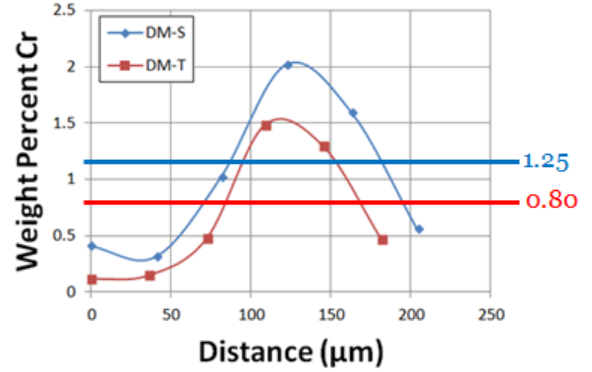


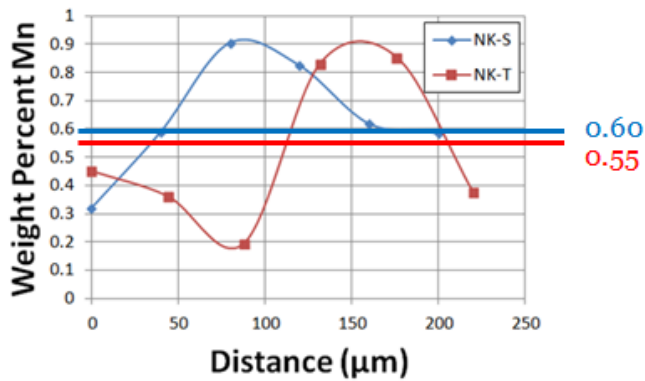
Figure 47: BSE Images and WDS Elemental Maps for DM-S and DM-T (Large grains outlined by a white square)



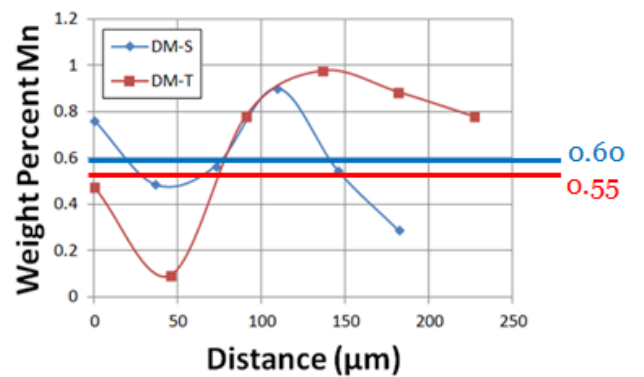
a): Cr quantification of NK-S and NK-T



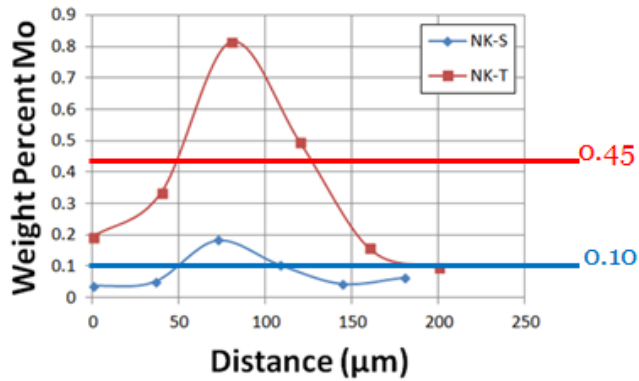
b): Cr quantification of DM-S and DM-T



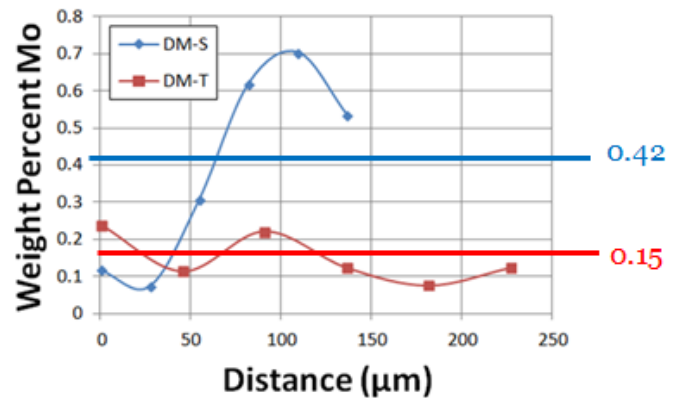
c): Mn quantification of NK-S and NK-T



d): Mn quantification of DM-S and DM-T



e): Mo quantification of NK-S and NK-T



f): Mo quantification of DM-S and DM-T

Figure 48: WDS Point Quantification Plots For NK-S, NK-T, DM-S and DM-T

Figure 48 a) through f) correspond to WDS point quantification data obtained for each line of points as seen in a) through h) of Figure 46 and Figure 47. Lines were plotted from left to right of the end of the line of points which is labeled by either Cr, Mn or Mo for each alloy case. All chemical quantification profiles embody wave-like modulations; indicative compositional inhomogeneities as depicted by WDS maps. Here it must also be emphasized that it is very likely that multiple alloying element sources instead of a single source contributed to profile trends. Due to the wave-like modulations in many of the elemental profiles, a practical approach to analyzing the trends entails examining the midpoint of each line, between the compositional highs and lows. When doing so, one notices that in the case of Cr, superior alloys "homogenize" to an overall slightly higher value than that of traditional alloys, while for Mn, midpoint values are quite close. As for Mo profiles, NK-S appears to have homogenized to a much lesser value however the significant difference may not be a feat of significantly improved homogenization but rather that for NK-S as seen in Table 13 and as detected by ICP, Mo content in NK-S was 0.07 while that of NK-T was 0.37. As previously mentioned, diffusion of Mo in Fe is rather slow during solid-state sintering as Mo has a tendency to homogenize to a small extent and transform to carbides [12] - this can perhaps explain the large amplitude in wt% which exists for Mo in NK-T. Finally, for the case of Mo in DM-S and DM-T, at first glance, it is tempting to conclude that this element achieved better homogenization as for the case of DM-T as the midpoint here is approximately 0.15 while that of DM-S appears to hover in close approximation to 0.30. In this case, it is possible that either the quantification data was detected at locations slightly above the outlined line of points in Figure 48 h), consistently throughout a low intensity region, or if detected in the true location as outlined, Mo did homogenize. However, the latter is not as likely

especially when comparing to Table 4 where DM-S and DM-T alloys were tested to have Mo concentrations of 0.27 and 0.25 respectively.

Mechanical properties

It can be seen in Table 14 that mechanical properties including green strength, TRS and UTS were superior for all specialized alloys in comparison to traditional alloys. However, it must be emphasized that differences are not large enough to strongly conclude that specialized alloys perform significantly better than traditional alloys. Nonetheless, in the case of NK-S which appeared to have a Mo content five times lower than that of NK-T, these slightly superior, if not similar TRS results can be deemed to be quite impressive. As for sintered hardness, it is seen that NK-S performs slightly poorer than NK-T, however once again, the difference is still not drastic enough to draw any bold conclusions. Overall, it can be said that specialized alloys perform at par with alloys fabricated with traditionally produced master alloys.

Table 14: Mechanical properties and densities of PM steels produced in traditional and specialized manners

PM steel ID	Green body [60], [61]		Sintered [60]		Austenitized and quenched [60]		
	Density g/cm ³	Green Strength MPa	Density g/cm	HRB	TRS MPa	UTS MPa	Elongation at fracture
NK-S	6.97	13	6.94	75	1379 ± 15	848±29	1.87 ± 0.19
NK-T	6.96	12	6.96	79	1289 ± 29	830±13	0.47 ± 0.17
DM-S	7.02	14	7.00	80	1300 ± 5	820±4	1.1 ± 0.4
DM-T	7.03	12	7.04	75	1278 ± 25	800 ± 11	0.47 ± 0.17

Chapter 9: Additional Master Alloys

Characteristics of Additional Master Alloys (M1, M2 and M3)

Three additional multi-component master alloy powders (labelled M1, M2 and M3) were fabricated via arc-melting. The selected compositions of these sets met the criterion of having a minimum of 80% liquid present at a sintering temperature of 1280°C as seen in Table 15. Information about the liquidus temperature and weight percent of liquid at two sintering temperatures (1280°C and 1150°C) were obtained via the Fortran-Thermo-Calc program as previously described and were later confirmed again in Thermo-Calc by re-simulating Scheil solidification and plotting mass fraction of liquid on the x-axis as seen in Figure 49, Figure 50 and Figure 51 for M1, M2 and M3. These directly simulated values coincided with those obtained through the program.

Table 15: Master Alloy Characteristics (Compositions, Liquidus Temperature and Weight Percent of Liquid at Various Sintering Temperatures)

	Composition (wt%)						T_{liquidus} (°C)	Weight percent of liquid at selected sintering temperature ($W_{\text{Sintering Temperature}}$)	
	C	Mn	Mo	Ni	Cr	Fe		$W_{1280^{\circ}\text{C}}$	$W_{1150^{\circ}\text{C}}$
M1	3.5	52	8	4	8	24.5	1304	97.3%	85.6%
M2	3.5	36	10	8	22	20.5	1465	80.1%	72.3%
M3	4	58	8	10	0	20	1279	100%	91.4%

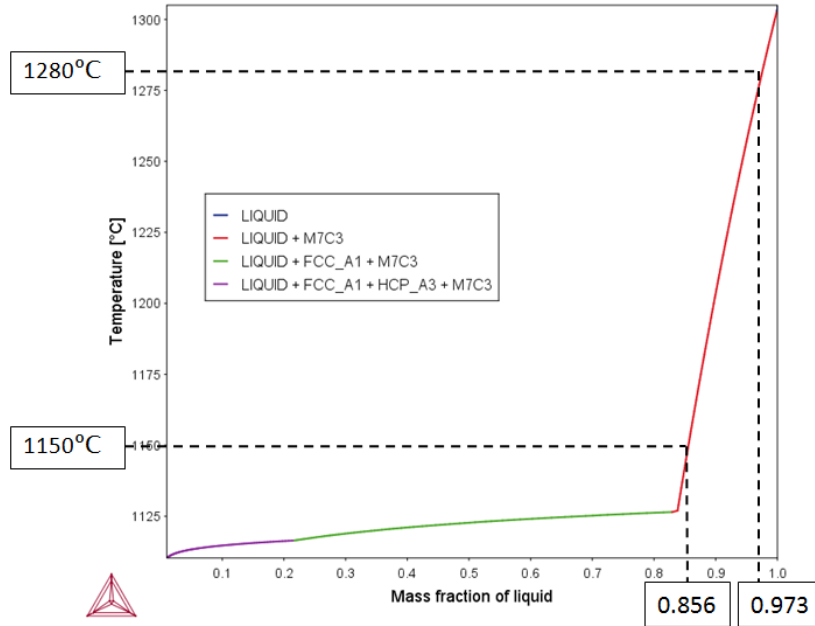


Figure 49: Thermo-Calc Scheil Simulation of M1: 3.5C-52Mn-8Mo-4Ni-8Cr-24.5Fe

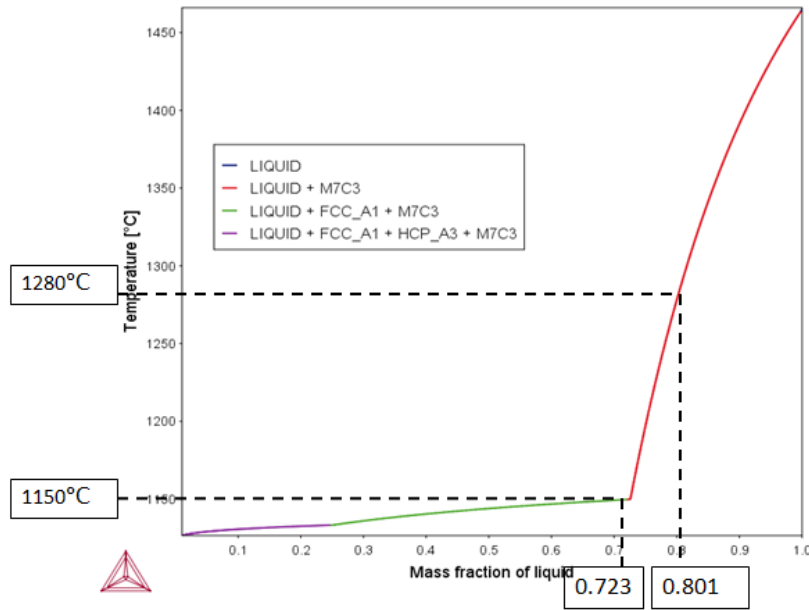


Figure 50: Thermo-Calc Scheil Simulation of M2: 3.5C-36Mn-10Mo-8Ni-22Cr-20.5Fe

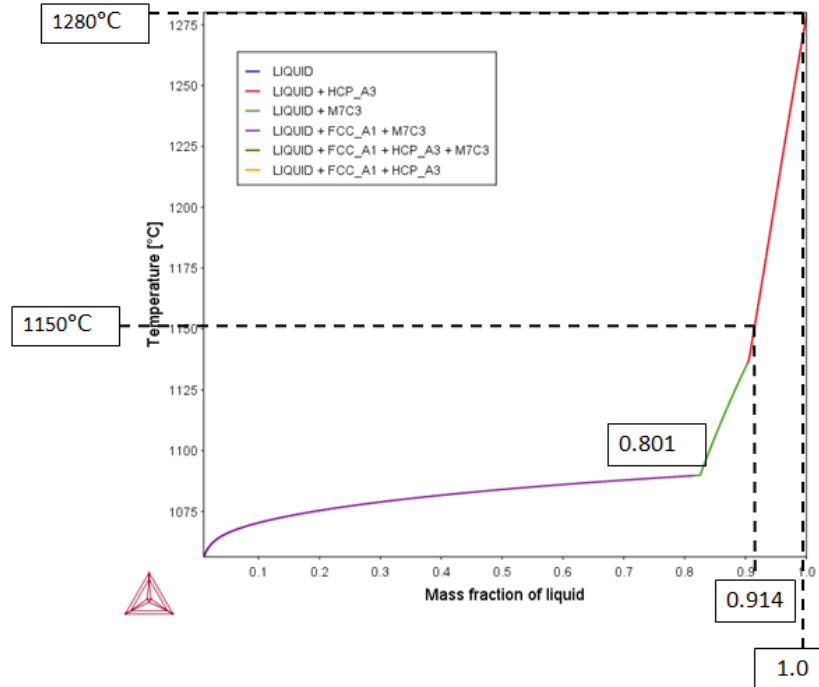


Figure 51: Thermo-Calc Scheil Simulation of M3: 4C-58Mn-8Mo-10Ni-20Fe

Calorimetric Examination

Similar to the previous DSC curves, thermal effects are considered to be distinct deviations from the portions of the curve that are rather straight. The minima of the first peak along the red (heating) direction corresponds to the onset of melting. As seen in a) of Figure 52-51, M1, M2 and M3 display that thermal events begin occurring at approximately 1160°C, 1190°C and 1155°C for coarse particle curves respectively. Enthalpy-temperature plots were created on Thermo-Calc to compare computational predictions of the temperature for an initial solid-liquid phase change with that which is seen in experimental DSC curves. When observing enthalpy versus temperature plots for M1, M2 and M3 (Figure Figure 52b, Figure 53b and Figure 54b), the temperature at the initial spike in each enthalpy curves which can be correlated to a solid-

liquid phase change, is consistently lower (1122°C, 1144°C and 1079°C respectively for M1, M2 and M3). However, as all Thermo-Calc and experimental values are within 100°C of each other, the discrepancies that exist very well may be a result of experimental or equipment-related error.

A distinct difference exists between the DSC curves for coarse and fine particles. In literature, differences that exist in the DSC curves of coarse and fine particles of the same material are justified as a difference in the nucleation rate of each crystal [62], [63]. Although all powders were sieved eventually to less than 38µm, the powders were in fact originally produced via arc melting and ball milling. During the milling process, it was also noted that larger particles came from fragments of the initial ingots that were not brittle enough to quickly be milled into fine powder. This suggests that coarse and fine particles for MMA1, MMA2 and MMA3 in fact have different compositions, resulting in slightly different DSC heating and cooling behaviour.

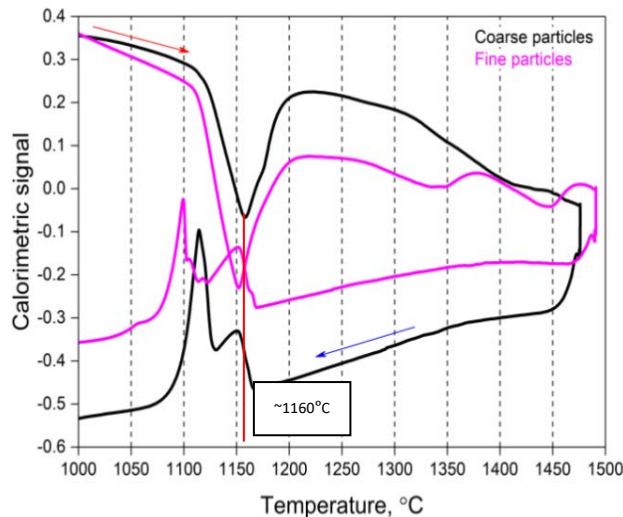


Figure 52 a): DSC Curve for M1(Calorimetric signal: $\mu\text{V}/\text{mg}$)

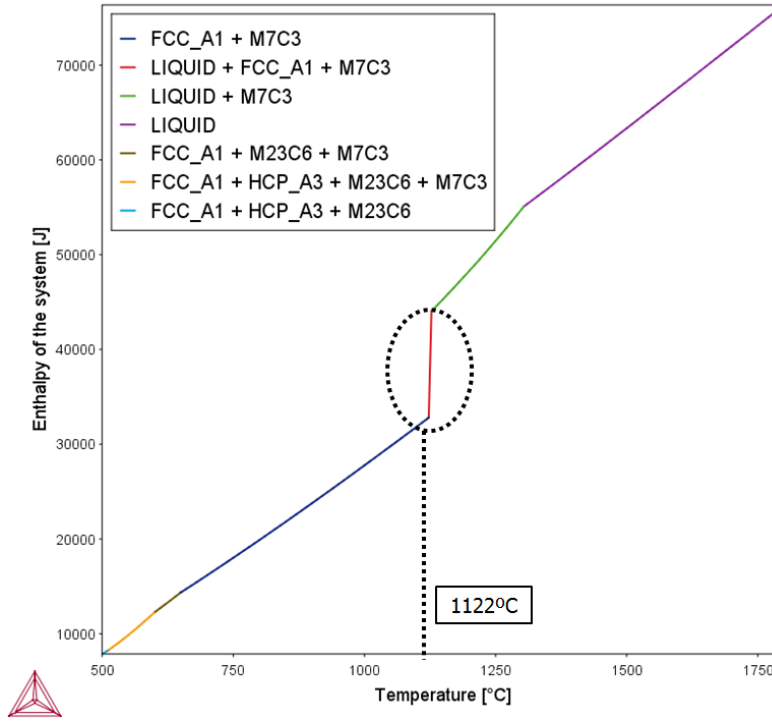


Figure 49 b): Thermo-Calc Enthalpy-Temperature Plot for M1

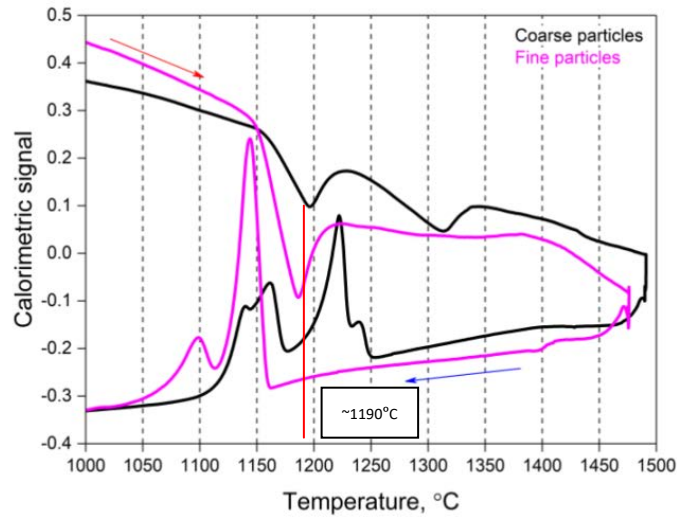


Figure 53 a): DSC Curve for M2 (Calorimetric signal: $\mu\text{V}/\text{mg}$)

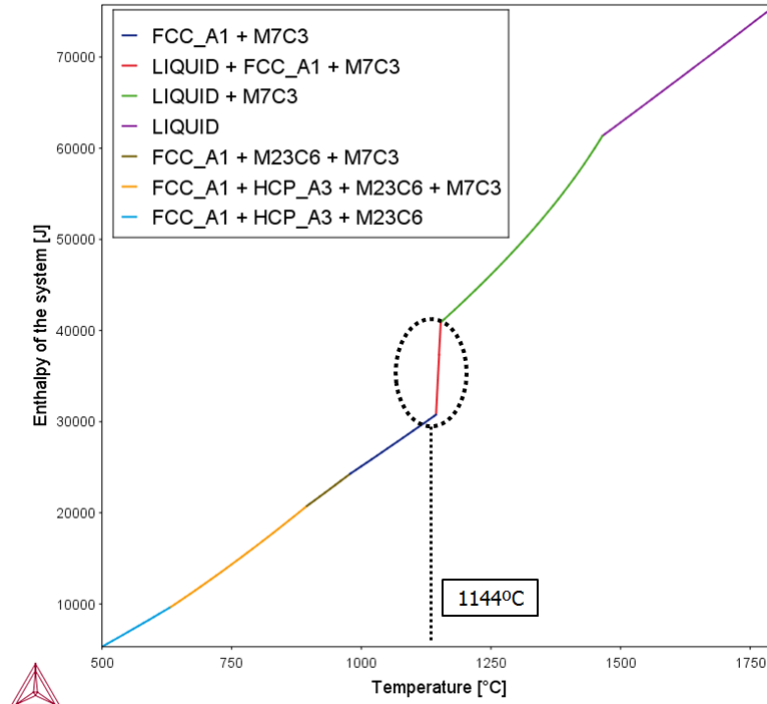


Figure 50 b): Thermo-Calc Enthalpy-Temperature Plot for M2

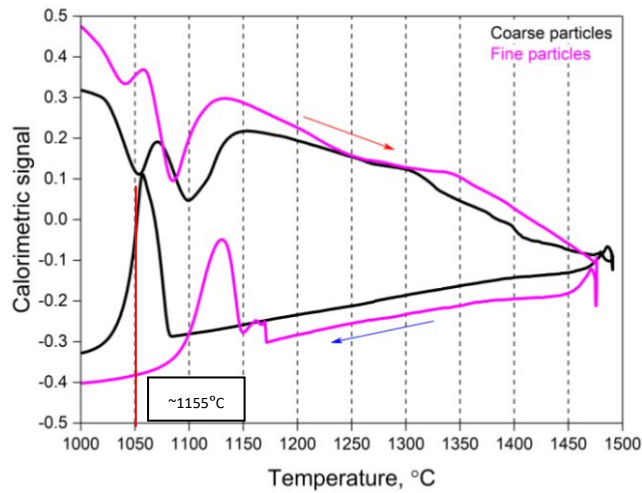


Figure 54 a) DSC Curve for M3 (Calorimetric signal: $\mu\text{V}/\text{mg}$)

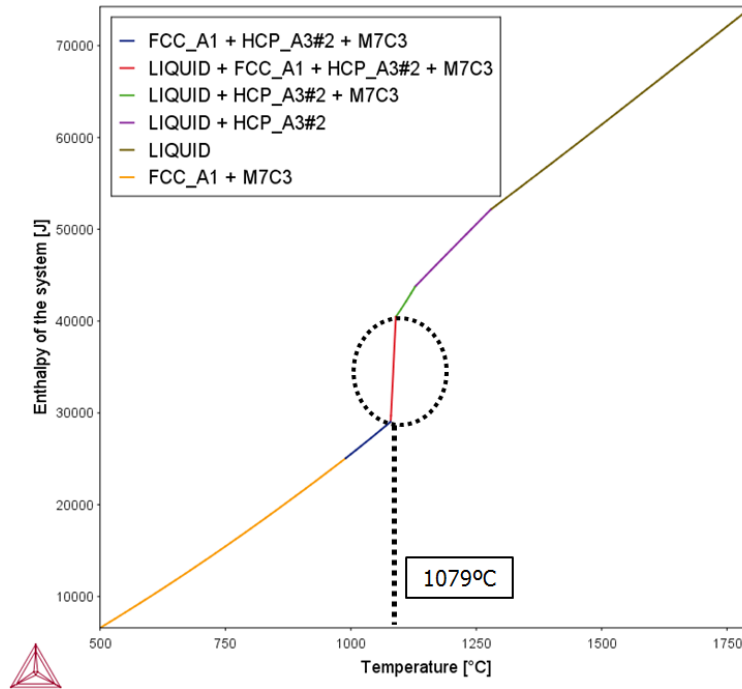


Figure 51 b): Thermo-Calc Enthalpy-Temperature Plot for M3

Overall Compositions for Additional Alloy Blends

Overall compositions were selected to produce an ideal diameter (D.I.), of 4 inches. As D.I. is known to be the largest diameter for which 50% of which will transform into martensite upon quenching [5], given the largest diameter of a section of the clutch hub and sprocket, 4 inches was found to be a reasonable D.I. to design for. SteCal 3.0 software was used to predict the optimal combination of C, Cr, Mn, Mo and Ni as well as C, Mn, Mo and Ni. Selected overall compositions and D.I. results can be seen in Table 16.

Table 16: Calculated Overall Compositions To Achieve a D.I. of 4.0 inches

	C (wt%)	Cr (wt%)	Mn (wt%)	Mo (wt%)	Ni (wt%)
A1	0.61	0.2	1.26	0.2	0.1
A2	0.61	0.55	0.85	0.25	0.2
A3	0.60	0	1.40	0.20	0.26

With an intent to further study the effects of liquid phase sintering by comparing the performance of MMAs that activate LPS to alloying additions that do not readily activate LPS, all 3 compositions were produced in 2 final sets: MAx sets (x=1,2 or 3) corresponding to McMaster Alloys (produced using MMA powders of compositions formulated via the ThermoCalc - Fortran program), and SAx sets (x=1,2 or 3) corresponding to Stackpole Alloys (produced using individual ferroalloy or pure metal powders employed in industrial PM parts.) After creating TRS test bars and carrying out chemical analyses on a bar from each set, the overall compositions and recalculated D.I. can be seen in Table 17:

Table 17: D.I and Overall Compositions As Detected via ICP Chemical Analysis

		A1		A2		A3	
		MA1	SA1	MA2	SA2	MA3	SA3
Composition (wt%)	C	0.62	0.62	0.61	0.70*	0.62	0.77*
	Cr	0.24	0.26	0.58	0.61	0	0
	Mn	1.43	1.57	0.99	1.24	1.68	2.32*
	Mo	0.21	0.21	0.27	0.27	0.23	0.28
	Ni	0.12	0.12	0.21	0.24	0.28	0.27
	Fe	97.38	97.22	97.34	96.94	97.19	96.36
D.I. (inches)		4.7	5.2	4.7	6.2	5.1	8.4

*D.I. was calculated using these values however SteCal 3.0 stated that these values were outside the recommended limits of the methods of calculation used in the program

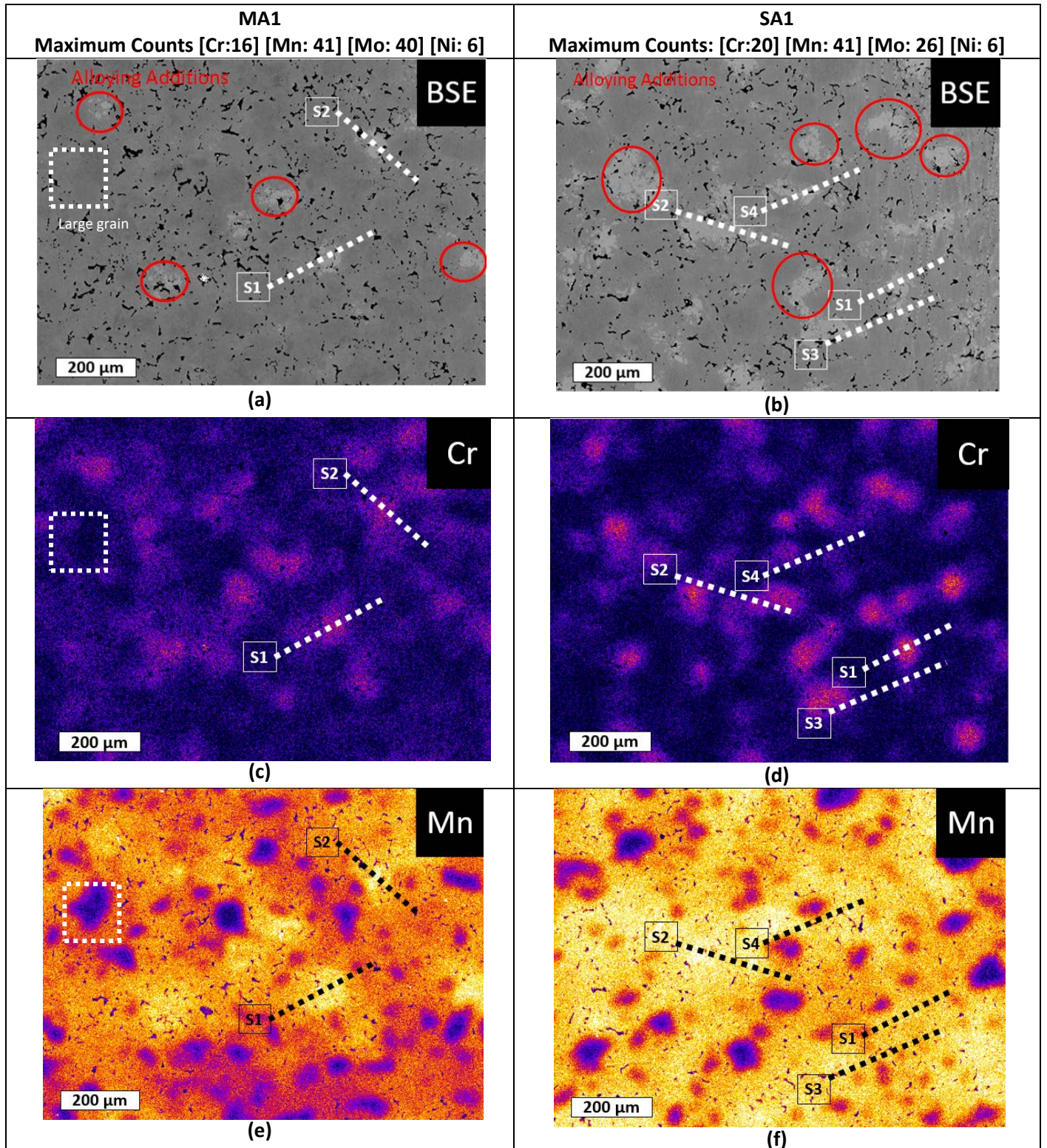
Values in red show a difference of more than 0.2 wt% between compositions. This difference in composition inevitably manifests itself in the large increase in D.I. between MA2 and SA2 (4.7 inches to 6.2 inches) as well as MA3 and SA3 (5.1 inches to 8.4 inches).

Electron Microscopy - WDS Maps and Quantification

Elemental WDS maps were collected for Cr, Mn, Mo and Ni after TRS bars were industrially sintered - this time at 1300°C. Alloying addition sources have been circled in red for BSE images within this section. WDS quantification points were analyzed across lines between 175µm to 300µm in width and were selected by looking at high intensity and relative low intensity regions of each alloying element in WDS elemental maps. However, it should be noted that selected points failed to cross through low-intensity regions for certain elements.

As MA1, MA2 and MA3 were all fabricated with a multi-component master alloy, alloying elements in WDS maps are typically seen to diffuse with their highest concentrations at the same centre of the original multi-component master alloy particle. As a result, a maximum of 2 lines of points were analyzed for quantification purposes in the MAx series. However, as the SAx series were fabricated with different, individual alloy sources (ferrochromium, ferromanganese, ferromolybdenum and pure nickel), high intensity locations of alloying elements vary from one another. As a result, a line of points was drawn for each specific alloying element. A total number of 4 lines were selected for SA1 and SA2 (due to the presence of the four elements: Cr, Mn, Mo and Ni) while 3 were selected for SA3 (due to the presence of only the three elements which include: Mn, Mo and Ni). As the maximum counts for each element, corresponding to the

colour intensities in each map, is different between the MAx and SAx series, a direct qualitative comparison based upon brightness between the maps is not recommended.



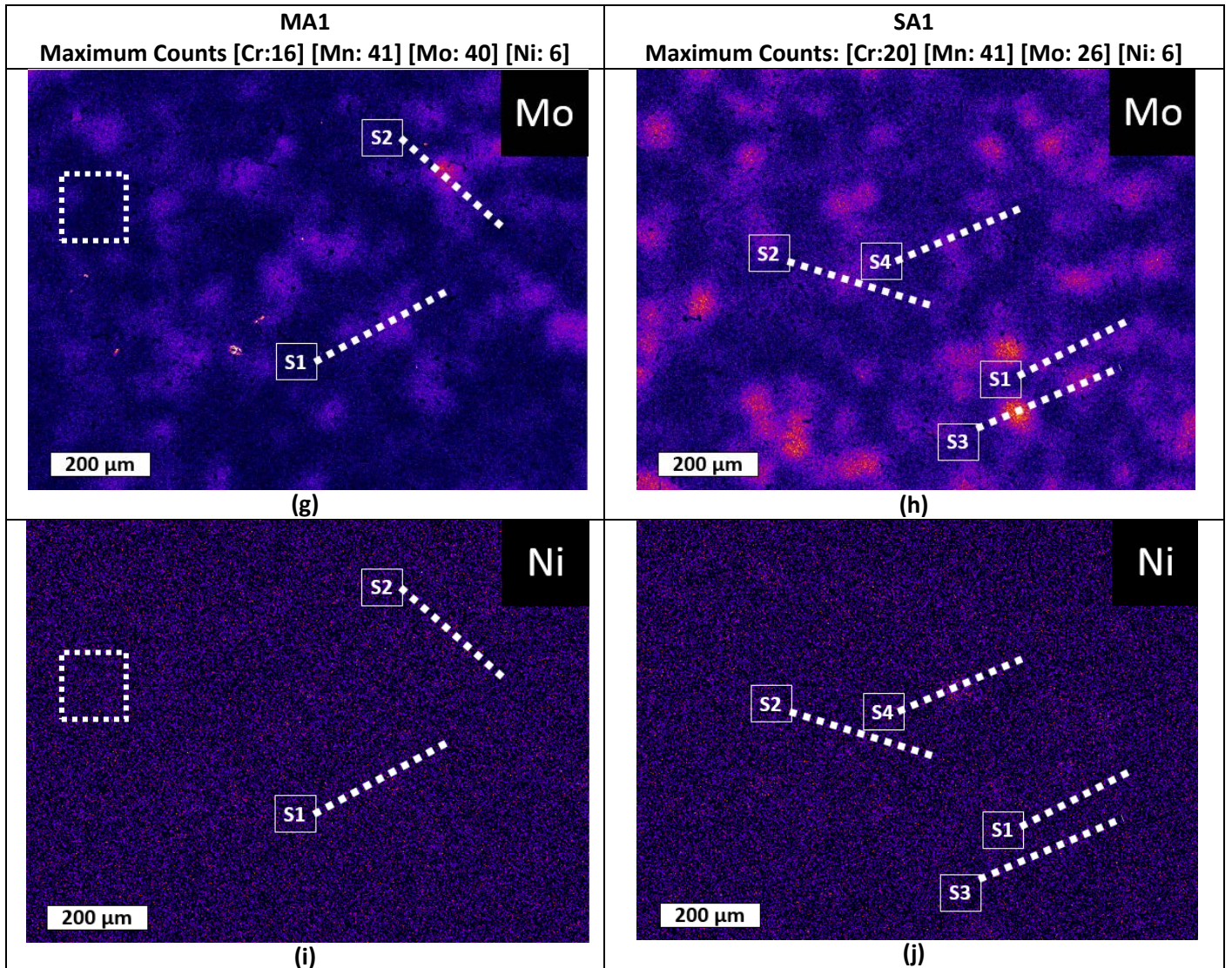
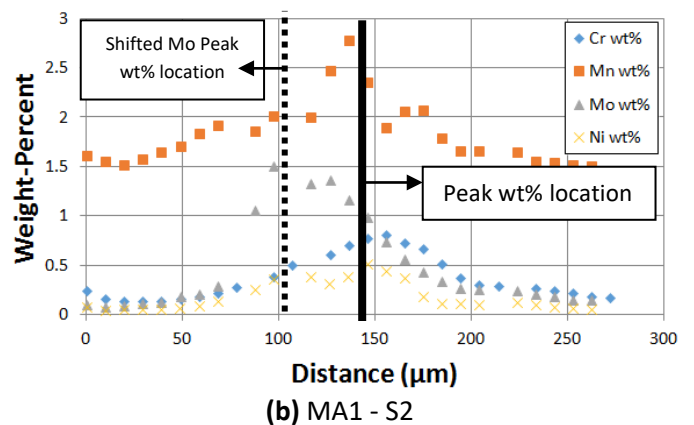
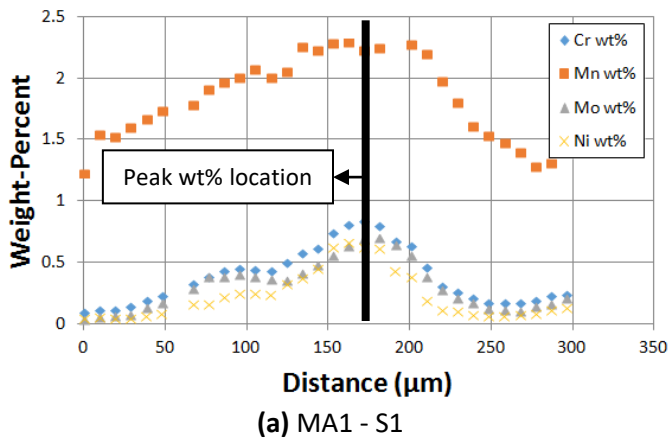


Figure 55: a) BSE image of MA1, b) BSE image of SA1, c) Cr WDS Map of MA1, d) Cr WDS Map of SA1, e) Mn WDS Map of MA1, f) Mn WDS Map of SA1, g) Mo WDS map of MA1, h) Mo WDS map of SA1, i) Ni WDS map of MA1, j) Ni WDS map of SA1 (A Large Grain in MA1 is Outlined in a White Square)

A look at the BSE images for MA1 and SA1 in Figure 55 a) and b) suggests that alloying elements from the multi-component master alloy source (MA1) display improved homogenization as bright white spots corresponding to the heavier alloying elements are not as frequently seen as in the BSE image for SA1. The dissolutive nature of MA1 however cannot be accurately determined through its BSE image. Furthermore, a lack of literature involving WDS investigations for alloy element homogenization, especially for LPS-activating additions in PM

steels, makes it difficult to characterize dissolutive behaviour of particles in this research based upon WDS maps that were collected for this investigation. As for secondary porosity [58] as previously seen in LPS-activating master alloys, in the case of MA1, it is not readily noticed. Finally, the white square in the MA1 BSE image which is overlaid onto WDS elemental maps shows that despite the strategic design to improve alloying element homogeneity, it cannot counteract the detrimental effect of having large Fe grains which are rather difficult to properly alloy [12].

A comparative analysis between the maps of Cr, Mn, Mo and Ni for MA1 and SA1 in Figure 55 does not allow one to conclude upon which alloy performed better (MA1 or SA1), as both maps for each element are quite similar. What is evident in the case of both MA1 and SA1 is that Ni no longer exists in high intensity spots. As for MA1, it is known that the starting MMA had a Ni content of 4.0wt%, a significantly lower amount than that of pure Ni alloying sources employed in SAx alloys. As a result, the dramatic improvement in reduced high-intensity Ni regions is expected.



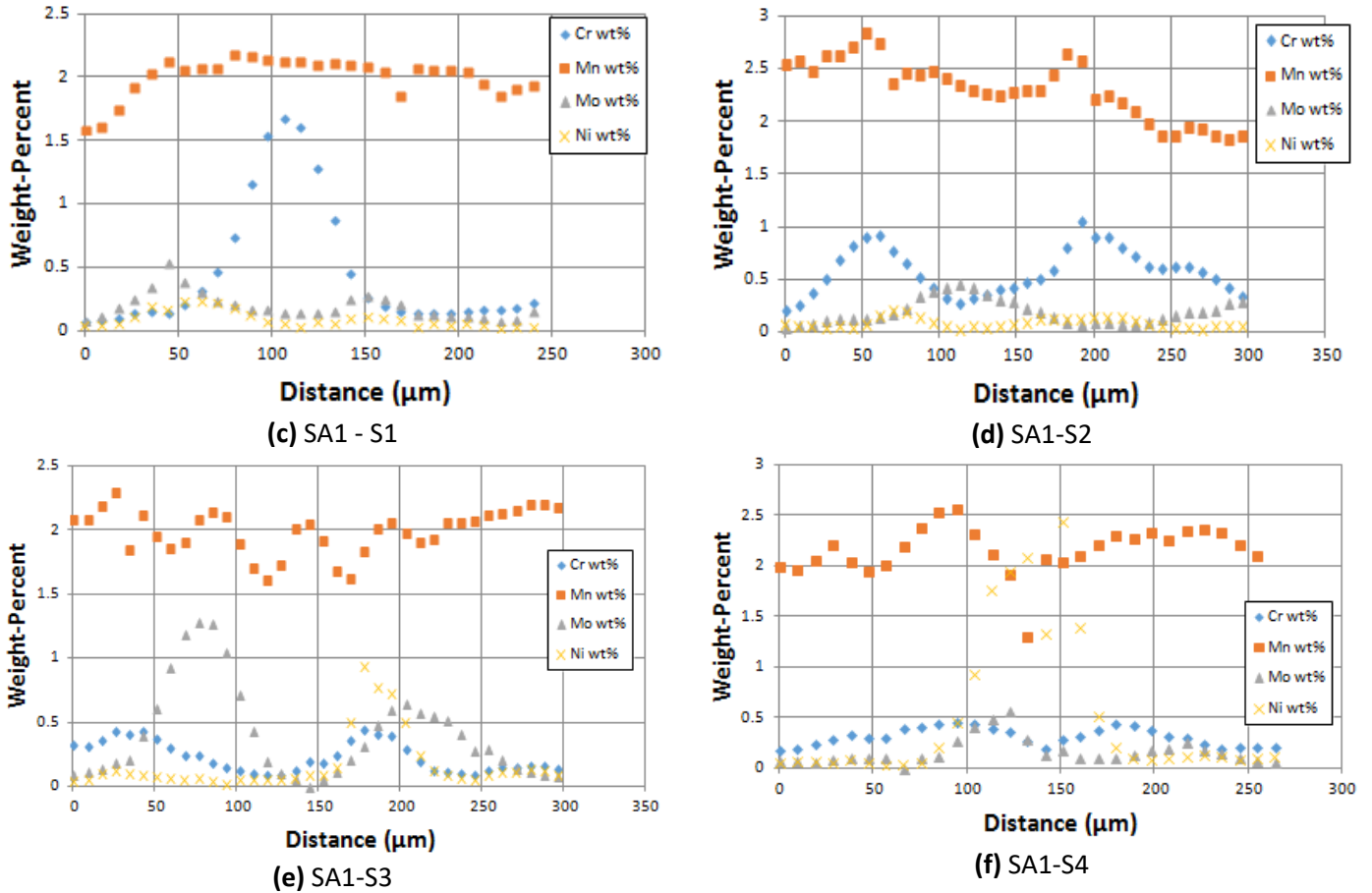
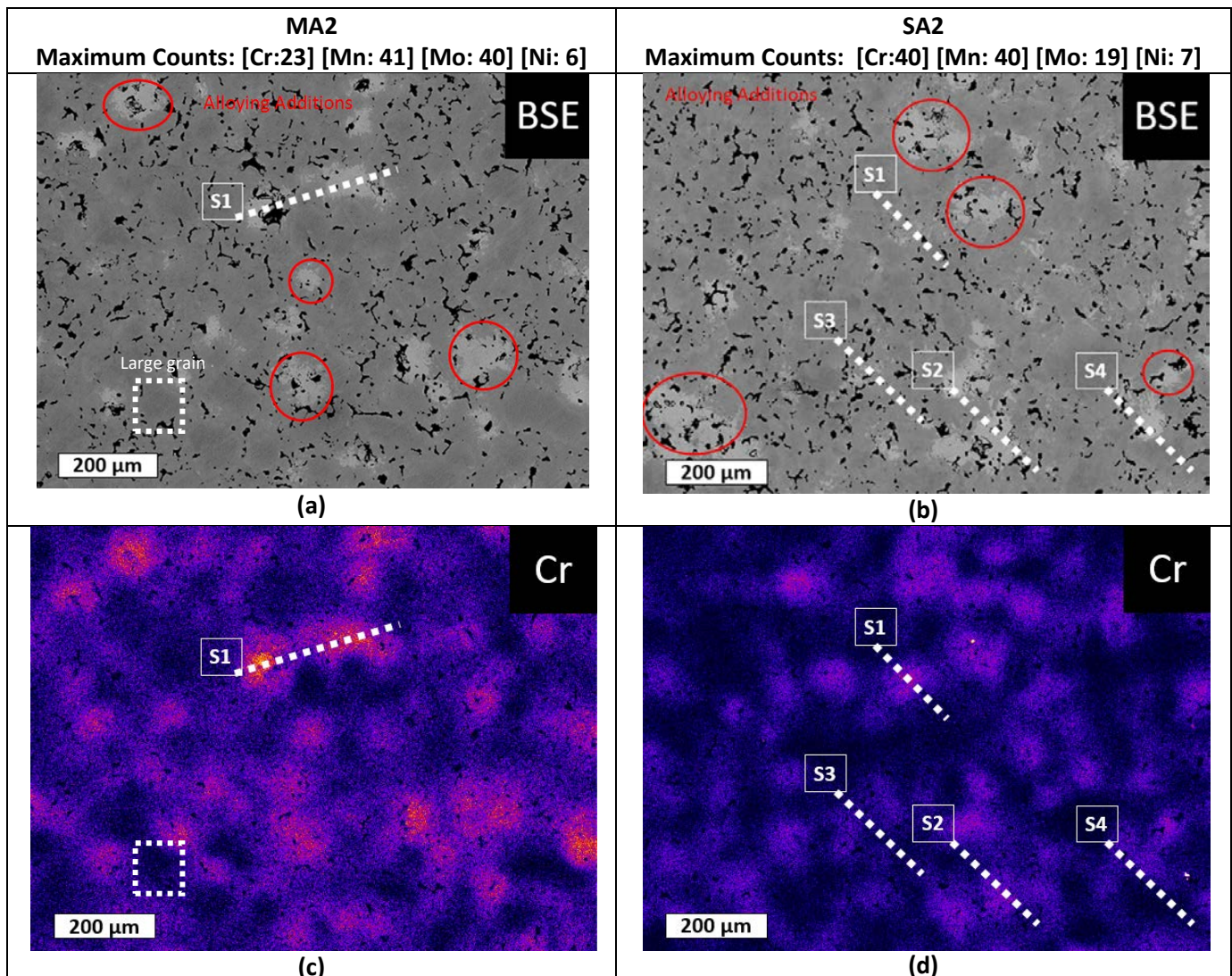


Figure 56: WDS Quantification Plots for a) MA1 - Line S1, b) MA1 - Line S2, c) SA1 - Line S1, d) SA1 - Line S2, e) SA1 - Line S3, f) SA1 - Line S4

Recalling the overall compositions of MA1: 0.24Cr-1.43Mn-0.21Mo-0.12Ni-0.62C, in the case of both "line-scans" S1 and S2, quantified compositions as seen in the WDS plots in Figure 56 do not fluctuate more than approximately 0.70wt% from the overall compositions. Peak locations of all elements for both lines S1 and S2 for MA1 (as marked by a solid black line) have a tendency to coincide with one another as expected due to the nature of element diffusion from the same starting source. The slightly shifted Mo peak in Figure 53 b) either results from a possible error in detection, or is perhaps a fruit of a differently inherited composition in a certain area of the original particle - a possibility due to the arc-melting and milling production

technique that was used to fabricate the multi-component master alloy powder. As for SA1: 0.26Cr-1.57Mn-0.21Mo-0.12Ni-0.62C, peak locations for Cr, Mn, Mo and Ni in fact do not have the same tendency to coincide as alloying sources have an independent source nature since they originate from different powders (ie. Cr from ferrochromium, Mn from ferromanganese, Mo from ferromolybdenum and Ni from pure Ni particles). As a result, despite an absence of a high concentration of Mn as seen in SA1 line S4 at approximately 130 μ m, one can still observe a high concentration of Ni.



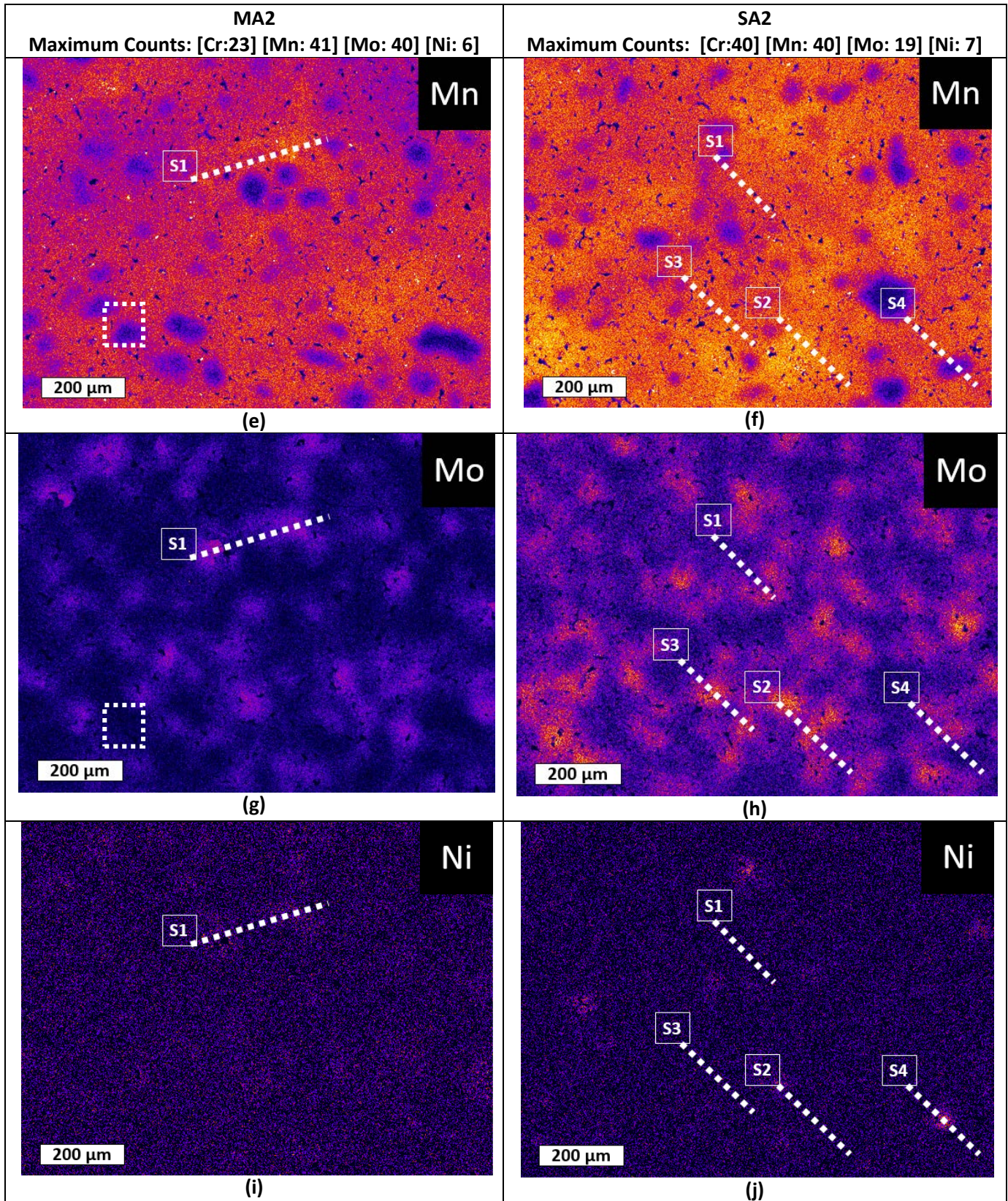
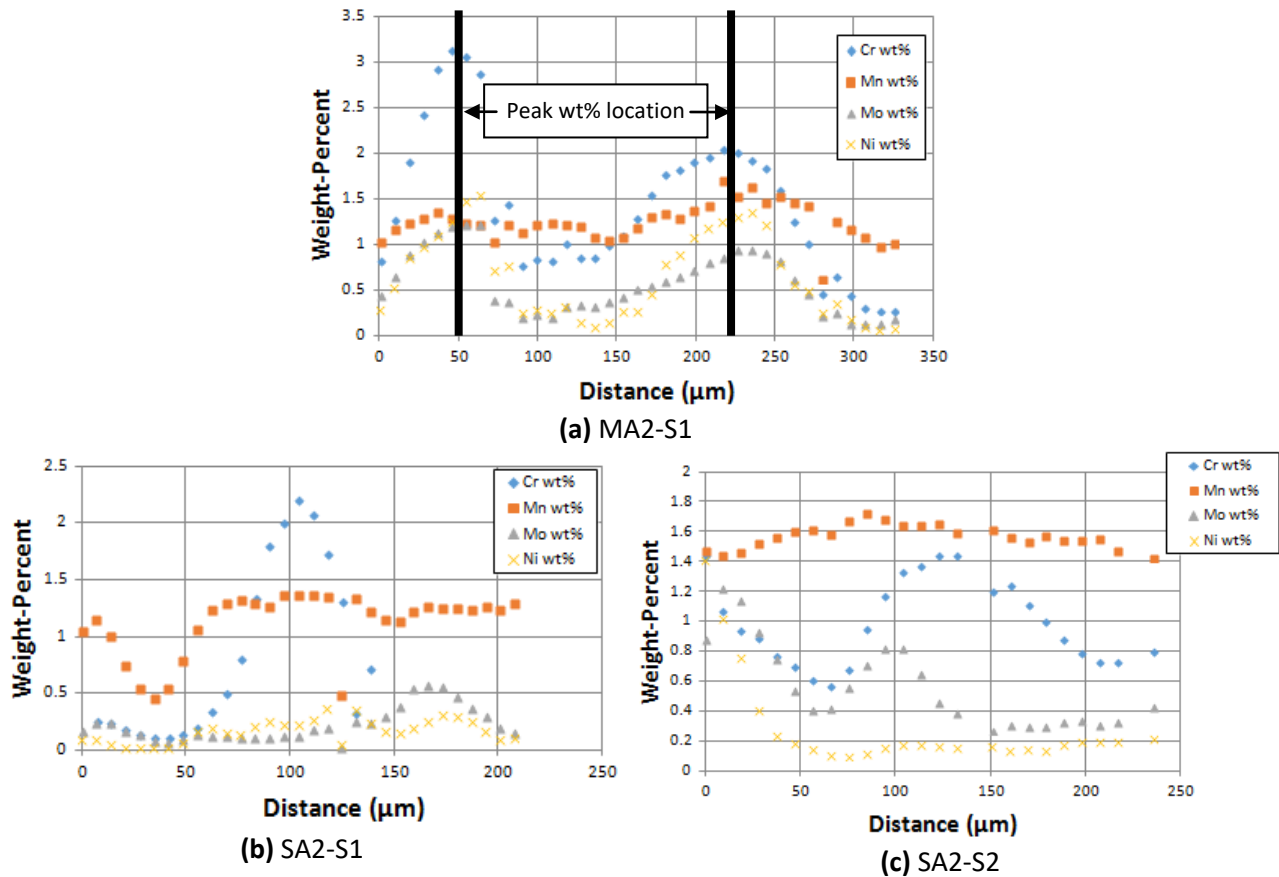


Figure 57: a) BSE image of MA2, b) BSE image of SA2, c) Cr WDS Map of MA2, d) Cr WDS Map of SA2, e) Mn WDS Map of MA2, f) Mn WDS Map of SA2, g) Mo WDS map of MA2, h) Mo WDS map of SA2, i) Ni WDS map of MA2, j) Ni WDS map of SA2

Similar to MA1 and SA1, Cr, Mn, Mo and Ni maps of MA2 and SA2 in Figure 57 are quite similar in appearance. As a result, it would once again be naive to draw any sound conclusions upon a mere visual inspection. In addition to the similarity in visual appearances, the maximum counts for Cr and Mo in particular do vary enough (Cr: 23 vs. 40 in MA2 and SA2 respectively and Mo: 40 vs. 19 for MA2 and SA2 respectively) to once again suggest that quantitative data should be analyzed prior to solidifying any conclusions. What is certain in the two sets of maps however is that large iron grains are consistently improperly alloyed as was noted in the first stages of the project. Furthermore, it is seen once again that despite altering alloying element form (LPS-activating or non-LPS-activating), there does not seem to be a significant improvement on the alloying of large Fe grains.



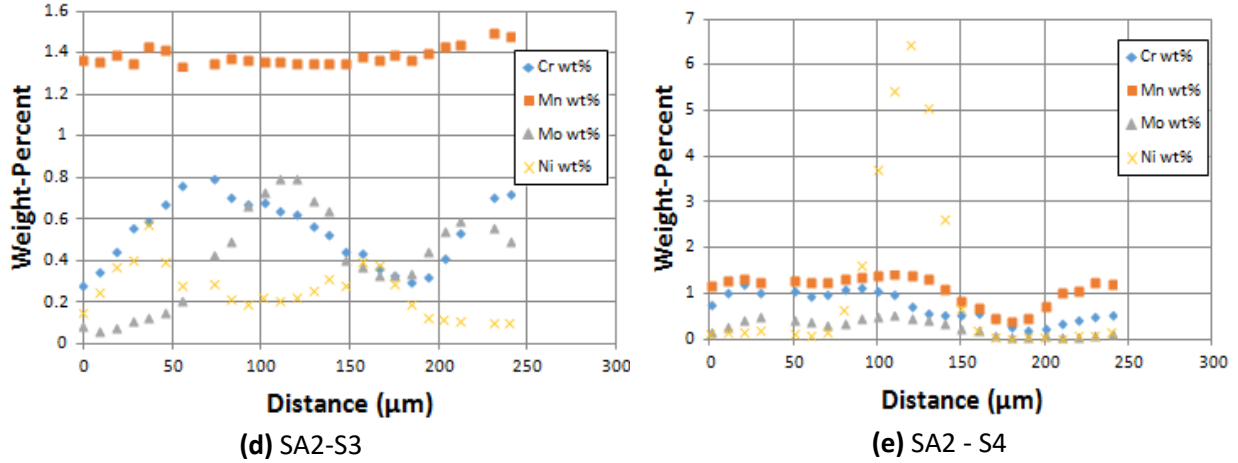
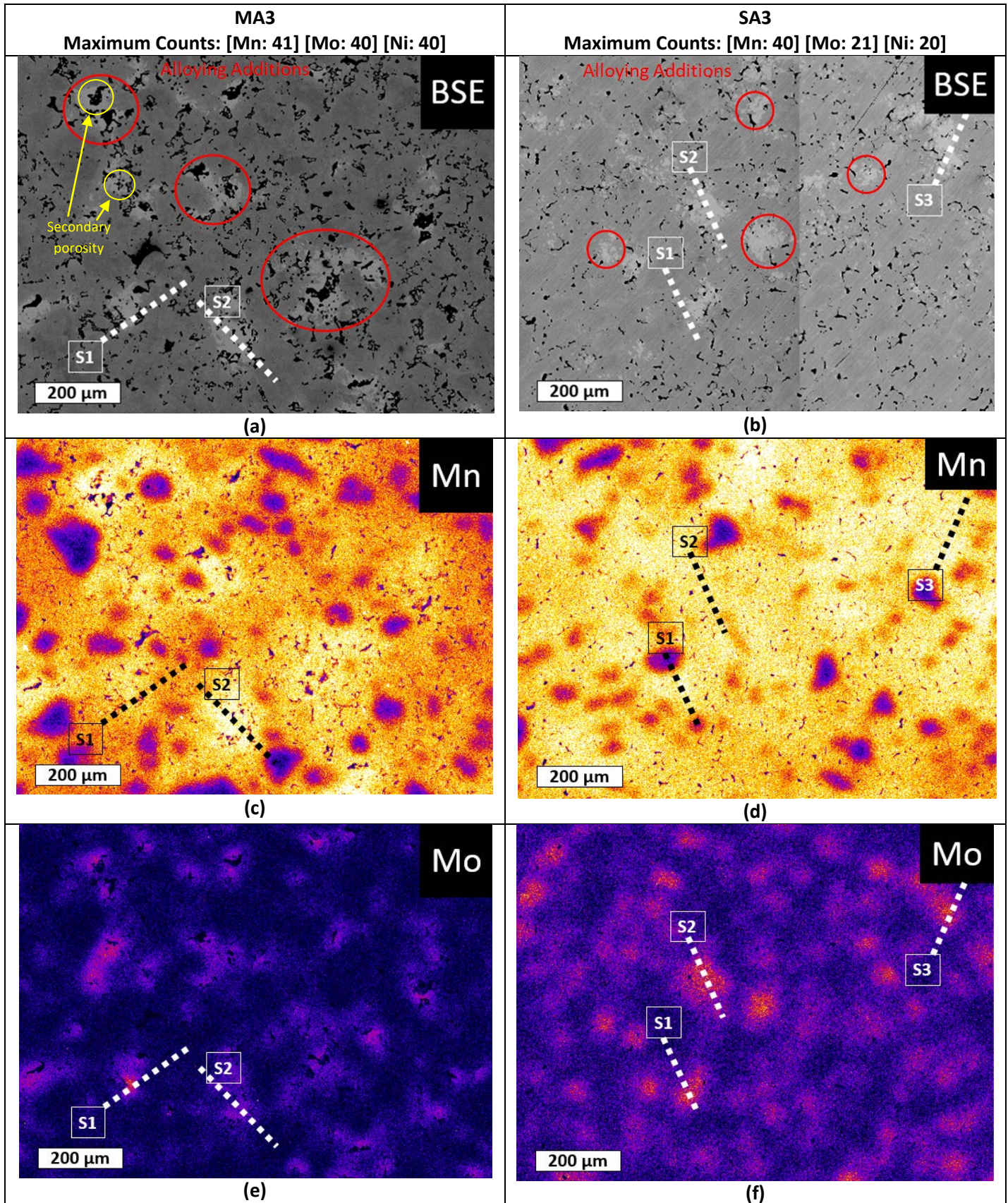


Figure 58: WDS Quantification Plots for a) MA2 - Line S1, b) SA2 - Line S1, c) SA2 - Line S2, d) SA2 - Line S3, e) SA1 - Line S4

Keeping in mind the overall compositions of MA2: 0.58Cr-0.99Mn-0.27Mo-0.21Ni-0.61C and SA2: 0.61Cr-1.24Mn-0.27Mo-0.24Ni-0.7C, it is evident that a direct comparative analysis between MA2 and SA2 in Figure 58 cannot be made for Mn in particular as the overall Mn content varies by 0.25wt% between the two. However, once again approximate peak positions as marked in black, for Cr, Mn, Mo and Ni coincide with one another in MA2 as they should since all alloying elements in this case originate and diffuse out from the same particle source. The same cannot be said for SA2 as the alloying elements have a more independent nature since they do originate from different addition sources.



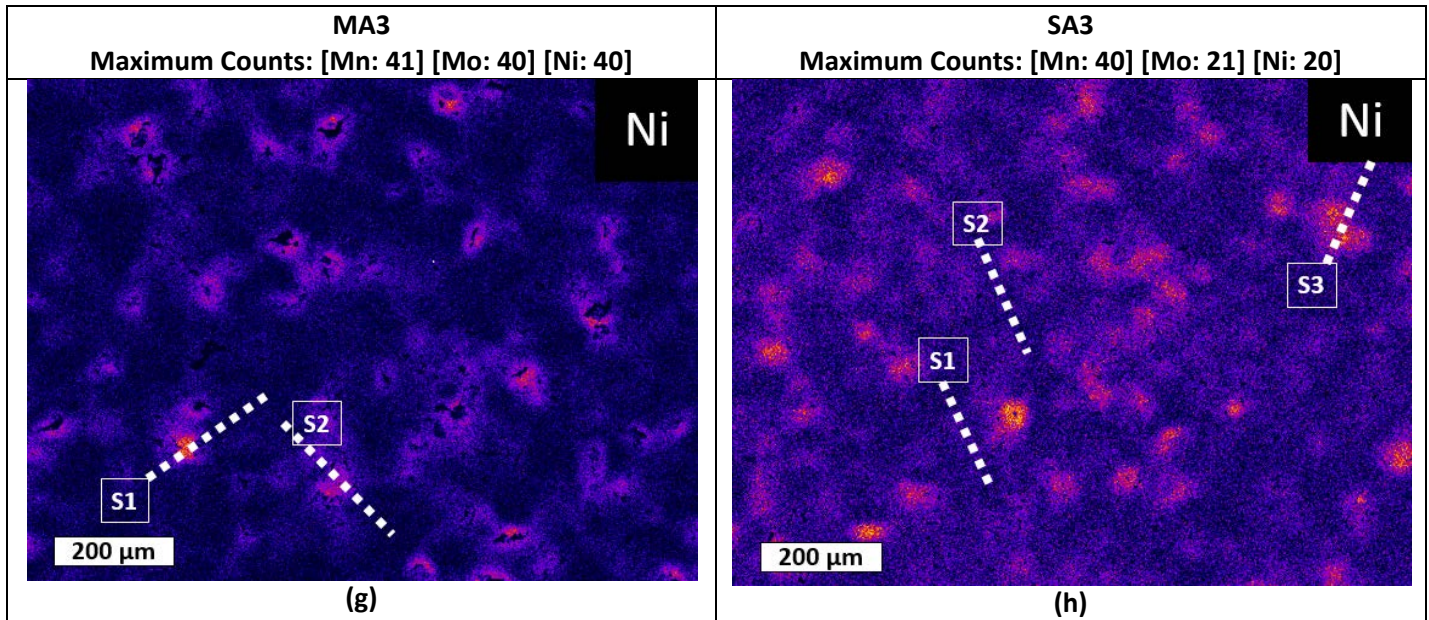


Figure 59: a) BSE image of MA3, b) BSE image of SA3, c) Mn WDS Map of MA3, d) Mn WDS Map of SA3, e) Mo WDS Map of MA3, f) Mo WDS Map of SA3, g) Ni WDS map of MA3, h) Ni WDS map of SA3

BSE images for MA3 and SA3 in

Figure 59 a) and b) do not show strikingly different dissolution behaviour in the presence of brighter alloyed spots. It is also difficult to conclude whether or not the liquid MA3 was able to properly wet and envelope the surfaces of iron grains. What can be seen however is that brighter diffused spots are readily observable around pores in MA3 in comparison to SA3. As previously discussed, this is potential evidence of secondary pore formation, characteristic of liquid phase sintering, and previously identified with Mo-rings surrounding these pores [12], [58].

Different from MA1 and MA2, what can be immediately noticed are the brighter-Ni rich regions that are present. The increased visibility between low and high Ni-concentration regions however

can be related to the higher maximum count intensity for MA3 and for SA3. Similar to MA1, SA1, MA2 and SA2 maps Mn, Mo and Ni resemble in appearance and therefore deserve a look into quantification data to draw any conclusions.

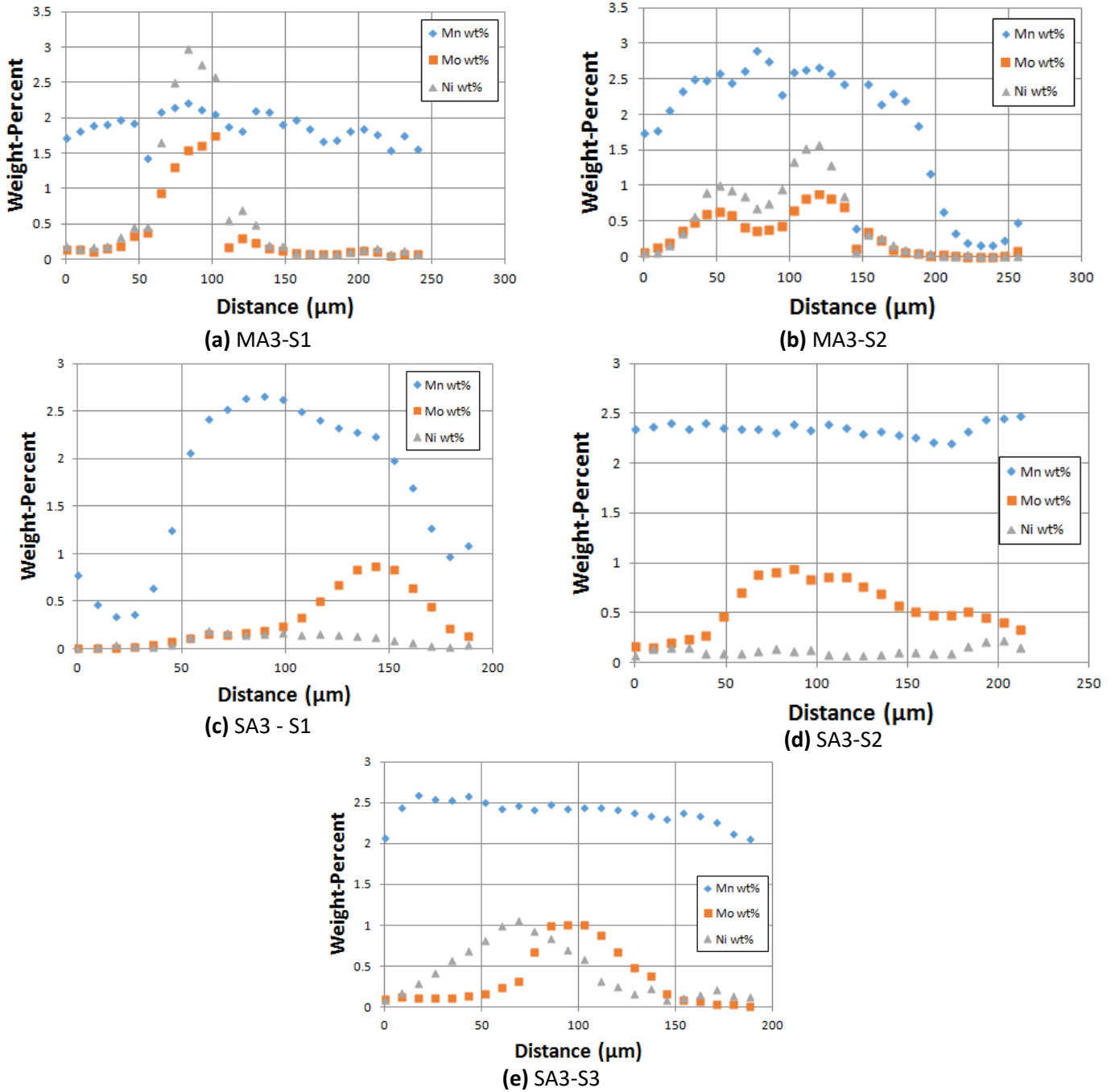


Figure 60: WDS Quantification Plots for a) MA3 - Line S1, b) MA3 - Line S2, c) SA3 - Line S1, d) SA3 - Line S2 and e) SA3 - Line S3

Recalling the overall compositions of MA3: 1.68Mn-0.23Mo-0.28Ni-0.62C and SA3: 2.32Mn-0.28Mo-0.27Ni-0.77C, Mn profiles in Figure 60 should not be compared between the two. However, when comparing individual profiles to their respective overall composition, significant fluctuations do not exist. Again, in the case of MA3, when a peak is seen for Mn, it is anticipated and seen for Mo and Ni as well whereas for SA3 this cannot be said. When reviewing element diffusivities as seen in Appendix B, Mn is expected to homogenize faster than Mo and Ni. When reviewing the plot of SA3 - line S3, where the points are quantified across a significant modulation in Ni (according to the corresponding WDS map), the Mn profile does appear to be much smoother than that of Ni and Mo. Here it is also worth recalling that Mn diffusion is also enhanced by vapour transport [58] which is not accounted for in its diffusivity in FCC-Fe from Appendix B.

It is interesting to note a significantly higher peak Ni concentration of just under 3.0wt% at its maximum in the case of MA3-S1. Despite the overall concentration of Ni for MA3 being 0.28 wt%, Ni in the original MA3 form was the highest at 10 wt% in comparison to MA1 and MA2 which had 4.0 wt% Ni and 8.0 wt% Ni respectively. Nonetheless, this amount is significantly lower than Ni when being added in pure form and it can perhaps be concluded that in the absence of Cr, Ni embodies a reduced diffusivity. A particular hypothesis for this behaviour can be found in the previous work of *Wu et al.*, which mentions a repelling behaviour between Ni and C - for which Cr powder was therefore alloyed with Ni due to chromium's strong tendency to form carbides, such that Ni could better diffuse throughout the PM component under study [48].

Mechanical Properties

Table 18: Green Strength and TRS for A1, A2 and A3 Alloy Sets

	A1 Alloy Set		A2 Alloy Set		A3 Alloy Set	
	MA1	SA1	MA2	SA2	MA3	SA3
Green Strength (MPa)	15.4±1.7	12.2±0.4	13.6±1.6	11.9±0.6	13.2±0.4	11.5±1.4
TRS (MPa)	1431±255	1168±151	1551±100	1088±312	1393±142	1198±117

As seen in Table 18, MAX mechanical properties of green strength and TRS are superior to those of SAX in all cases despite having lower total alloying element content and correspondingly lower D.I. values as previously calculated via SteCal 3.0. In the cases of A2 and A3 alloy sets, particularly MA2 and MA3 alloys, they had considerably lower C and Mn content in comparison to their respective SA2 and SA3 counterparts, indicating that the SA2 and SA3 alloys would have higher TRS values [64], however quite the opposite was observed. It is also interesting to see that the TRS values for the most comparable alloy set based on chemical analysis: MA1 and SA1, hold a notable difference of 367 MPa between their maximum possible values of 1686 MPa and 1319 MPa respectively. The larger differences that are present between the specimens made with LPS-activating additions and traditional alloy addition powders may be attributed to a higher fraction of liquid phase present at the increased sintering temperature in comparison to previous alloys that were investigated (NK-S and DM-S). Furthermore, despite the fact that the degree of homogeneity between MAX and SAX alloys were not extremely different as seen in WDS maps and quantification data, a potential cause of the improvement in mechanical properties as seen in the TRS values for MAX values may be due to an interplay between the multiple alloying elements existing at common locations throughout the specimen. Overall, the slight increase in sintering temperature of A1, A2 and A3 (from 1280 °C to 1300 °C) coupled

with a higher fraction of liquid phase and interplay of alloying elements when being delivered from a common multi-component master alloy source proved to be noticeably beneficial in terms of improving TRS values.

Chapter 10: Conclusions and Future Work

1. WDS was found to be an extremely useful yet significantly overlooked technique for homogenization studies in ferrous PM alloys.
2. WDS elemental maps highlighted that despite employing specialized alloys for LPS, the existence of large Fe grains severely impedes homogenization in ferrous alloys. It is therefore recommended that Fe powder is screened to remove all particles that are unreasonably large.
3. Long-term sintering displayed a high degree of chemical homogeneity for all alloying elements but is nonetheless unfeasible for production purposes.
4. If it is absolutely necessary to use DICTRA for homogenization studies, it is solely recommended to be used as a conservative semi-quantitative tool due to significantly over-estimated times that were associated with all diffusion profiles in this research.
5. DICTRA was not found to be a convenient piece of software to study diffusion of elements in carbon-containing ferrous alloys. It is anticipated that novice users will experience significant difficulty in successfully simulating cases that are similar in nature to those presented in this investigation (ie. due to ambiguous computational errors, abrupt freezing and program termination)
6. DICTRA comparison of multi-component alloy sources versus single-component alloy sources showed that the use of multi-component sources for Cr and Mn resulted in a more homogeneous alloy across an FeC particle. The use of MMAs are therefore recommended for industrial practices.

7. A combination of Thermo-Calc and Fortran proved to be a powerful and efficient system for computationally identifying compositions for master alloys that are suitable for liquid phase sintering.

8. Although mechanical properties including green strength, TRS and UTS were superior for all specialized alloys in comparison to traditional alloys, differences for specialized alloys with multi-component master alloys forming less than 80% of liquid phase are not large enough to strongly conclude that specialized alloys perform significantly better than traditional alloys. Instead, it suggests that these newly developed alloys performed at minimum on the same level as alloys using traditionally produced master alloys, despite being coarser in size.

9. A 20 °C increase in sintering temperature (from 1280°C to 1300 °C) for PM steels made with multi-component master alloys forming greater than 80% of liquid phase at the sintering temperature proved to be noticeably beneficial for improving TRS

Future work should investigate the performance of LPS-activating master alloys in comparison to traditional master alloys by producing an actual component such as a sprocket or clutch hub. As for the realm of PM simulations; although DICTRA was not such a suitable software to carry out diffusion simulations for PM materials, it is recommended that other software still be investigated. If it can be correctly implemented, an accurate ability to predict homogenization behaviour of alloys from the computational standpoint would serve as a key advancement in alloy design and in the sintering of PM steels.

References

1. James, W.B., *Powder Metallurgy Methods and Applications*. ASM Handbook, 2015. 7.
2. Kipouros, G.J., W.F. Caley, and D.P. Bishop, *On the advantages of using powder metallurgy in new light metal alloy design*. Metallurgical and Materials Transactions A, 2006. **37**(12): p. 3429-3436.
3. Šalák, A., *Ferrous Powder Metallurgy*. 1995, England: Cambridge International Science Publishing.
4. German, R.M., *Sintering Theory and Practice* 1996: Wiley.
5. America, S.F.s.S.o., *Hardenability and Heat Treatment Steel Castings Handbook*, (5th).
6. Kingery, W.D., *Sintering from Prehistoric Times to the Present Solid State Phenomena*, 1992. **25-26**: p. 1-10.
7. German, R.M., *History of sintering: Empirical phase*. Powder Metallurgy, 2013. **56**(2): p. 117-123.
8. Hoganas, N.A., *Powder Production - Presentation*, N.A. Hoganas, Editor. 2016: PM School.
9. de Oro Calderon, R., C. Gierl-Mayer, and H. Danninger, *Master alloys in powder metallurgy: the challenge of exploring new alloying compositions*. Powder Metallurgy, 2017. **60**(2): p. 86-96.
10. Lindsley, B., James W. B., *PM Steels that Contain Manganese*. 2010.
11. International, A., *Alloying: Understanding the Basics*, D.J.R.D. Associates, Editor. 2001.
12. Danninger, H., et al., *Comparison of Mn, Cr and Mo alloyed sintered steels prepared from elemental powders*. Powder Metallurgy, 2005. **48**(1): p. 23-32.
13. Bain, E.C. and H.W. Paxton, *Alloying elements in steel*. 1961: American Society for Metals.
14. Lindsley, B.a.R., H. *Effect of Mo Content in PM Steels*. in *POWDERMET2008*. 2008. Washington: MPIF.
15. Schneider, C.A.R., W. S., Eliceiri, K. W. , *NIH Image to ImageJ: 25 years of image analysis*. Vol. 9. 2012, Nature methods.
16. Gaskell, D.R., *Introduction to the Thermodynamics of Materials*. 5th ed. 2008: Taylor & Francis Group, LLC.
17. Zang, L., *Lecture 3: Diffusion: Fick's first law* Utah Engineering - College of Engineering
18. Wilkinson, D.S., *Mass Transport in Solids and Fluids*. 2000: Cambridge University Press.
19. Zhigilei, L.V., *Thermodynamics of Diffusion*. University of Virginia.
20. Bangalore, N.-I., *Grain Boundary Diffusion*. 2012.
21. Garimella, N., *Multicomponent Interdiffusion in Austenitic Ni-, Fe-Ni-Base Alloys and L12-Ni3Al Intermetallic for High-Temperature Applications*, in *Engineering and Computer Science* 2009, University of Central Florida: Orlando, Florida.
22. Oro, R., M. Campos, and J.M. Torralba, *Study of high temperature wetting and infiltration for optimising liquid phase sintering in low alloy steels*. Powder Metallurgy, 2012. **55**(3): p. 180-90.
23. Oro, R., Campos, M., Torralba, J M . and Capdevila, C., *Lean alloys in PM: from design to sintering performance*. Powder Metallurgy, 2012. **55**(4): p. 294-301.
24. Tahir, A.M., et al., *Behaviour of master alloy during sintering of PM steels: redistribution and dimensional variations*. Powder Metallurgy, 2015. **58**(2): p. 133-41.
25. Demetrio K. B., et al., *Sinterability and microstructure evolution during sintering of ferrous powder mixtures*. Materials Research, 2013. **16**(5): p. 1030-1038.
26. Tahir, A.M., Amberg, G., Hedstrom, P., Bergman, O., Chasoglou, D. and Frisk, K., *Behaviour of master alloy during sintering of PM steels: redistribution and dimensional variations*. Powder Metallurgy. **58**(2): p. 133-141.
27. German, R.M., *Applications for Liquid Phase Sintering*, in *Liquid Phase Sintering*. 1985, Springer US: Boston, MA. p. 223-236.

28. Magee, B.E., *Mechanisms of Liquid Phase Sintering In Fe-Cu Mixtures*, in *Metallurgy*. 1975, University of British Columbia.
29. Cavdar, U., Unlu, B. S., Atik, E., *Effect of The Copper Amount in Iron-Based Powder-Metal Compacts*. *Materials and Technology*, 2014(48): p. 977-982.
30. Sam, H. and Y.K. Ku, Won, L. K., Jae, M. D., *Swelling behaviour of Cu-coated Fe powder compacts in Fe-Cu system*. *Journal of the Korean Institute of Metals and Materials*, 1992. **30**(10): p. 1205-10.
31. Ayaad, A., Aqra, F., *Application of Young's Equation to Two Immiscible Liquids Resting on a Solid Substrate*. *Russian Journal of Physical Chemistry* 2010. **84**(13): p. 2290-2292.
32. De Oro Calderon, R., et al., *Liquid phase sintering control based on effective alloying design*. Vol. 1. 2012.
33. De Oro Calderón, R., et al., *Tailoring master alloys for liquid phase sintering: Effect of introducing oxidation-sensitive elements*. *Powder Metallurgy*, 2016. **59**(1): p. 31-40.
34. Bernardo, E., et al., *Design of Low-Melting Point Compositions Suitable for Transient Liquid Phase Sintering of PM Steels Based on a Thermodynamic and Kinetic Study*. *Metallurgical and Materials Transactions a-Physical Metallurgy and Materials Science*, 2014. **45A**(4): p. 1748-1760.
35. Gomez-Acebo, T., M. Sarasola, and F. Castro, *Systematic search of low melting point alloys in the Fe-Cr-Mn-Mo-C system*. *Calphad-Computer Coupling of Phase Diagrams and Thermochemistry*, 2003. **27**(3): p. 325-334.
36. Mocarski, S., et al., *Master Alloys to Obtain Premixed Hardenable Powder Metallurgy Steels*. *Powder Metallurgy*, 1996. **39**(2): p. 130-137.
37. Schaffnit, P., et al., *A Scheil-Gulliver model dedicated to the solidification of steel*. *CALPHAD: Computer Coupling of Phase Diagrams and Thermochemistry*, 2015. **48**: p. 184-8.
38. Porter, D.A., Easterling, K. E., Sherif, M. Y., *Phase Transformations in Metals and Alloys*. 2009: CRC Press, Taylor & Francis Group, LLC.
39. Goodhew, P.J., Humphreys, J., Beanland, R., *Electron Microscopy and Analysis*. 3rd ed.: Taylor and Francis Books UK.
40. Goldstein, J., Newbury, D.E., Joy, D.C., Lyman, C.E., Echlin, P., Lifshin, E., Sawyer, L., Michael, J.R., *Scanning Electron Microscopy and X-ray Microanalysis*. 2003: Springer US.
41. Scientific, T. *Wavelengthdispersive (X-ray) Spectroscopy*. 2016.
42. Neves, G.O., et al., *Application of computational thermodynamics to Fe/Ni, Fe-3%Si/Ni and 316L/Ni systems produced by powder metallurgy*. *Powder Metallurgy*, 2017: p. 1-8.
43. Oro, R., et al. *Liquid phase sintering control based on effective alloying design*. in *European International Powder Metallurgy Congress and Exhibition, Euro PM 2012, September 16, 2012 - September 19, 2012*. 2012. Basel, Switzerland: European Powder Metallurgy Association (EPMA).
44. Shykula P., D.E., Frykholm R., Bengtsson S., *Application of Computational Software for Design and Study New Alloys*. *Powder Metallurgy Progress*, 2013. **13**(1): p. 1-10.
45. Lindwall, G., et al., *Experimental and theoretical investigations of hot isostatically pressed-produced stainless steel/high alloy tool steel compound materials*. *Metallurgical and Materials Transactions A: Physical Metallurgy and Materials Science*, 2011. **42**(5): p. 1165-1172.
46. Benedet Dutra, G., M. Mulser, and F. Petzoldt, *Interface formation and diffusion of alloying elements during cosintering of MIM 316L/17-4PH stainless steel parts: Experiments and simulation*. *Powder Metallurgy*, 2011. **54**(5): p. 614-619.
47. Gauthier, M., et al. *Improved sinter-hardenability of prealloyed Fe-Cr-Mo steels by extra-fine nickel additions*. in *European International Powder Metallurgy Congress and Exhibition, Euro PM 2009, October 12, 2009 - October 14, 2009*. 2009. Copenhagen, Denmark: European Powder Metallurgy Association (EPMA).

48. Wu, M.W. and K.S. Hwang, *Improved homogenization of Ni in sintered steels through the use of Cr-containing prealloyed powders*. Metallurgical and Materials Transactions A (Physical Metallurgy and Materials Science), 2006. **37A**(12): p. 3577-85.
49. Sparber, B.A., et al. *A study of additive diffusion in ferrous powder metal compacts using scanning electron microscopy and energy dispersive x-ray spectroscopy*. in *2011 International Conference on Powder Metallurgy and Particulate Materials, PowderMet 2011, May 18, 2011 - May 21, 2011*. 2011. San Francisco, CA, United states: Metal Powder Industries Federation.
50. Oro, R., et al., *New Alloying Systems for Sintered Steels: Critical Aspects of Sintering Behavior*. Metallurgical and Materials Transactions A, 2015. **46**(3): p. 1349-1359.
51. Bernardo, E., et al., *Design of Low-Melting Point Compositions Suitable for Transient Liquid Phase Sintering of PM Steels Based on a Thermodynamic and Kinetic Study*. Metallurgical and Materials Transactions A, 2014. **45**(4): p. 1748-60.
52. Šalák, A. and M. Selecká, *Adverse effect of high purity atmosphere on sintering of manganese steels*. Powder Metallurgy, 2010. **53**(4): p. 285-294.
53. Šalák, A., Selecká, M., *Manganese in Powder Metallurgy Steels*. 2012: Cambridge International Science Publishing Ltd.
54. Andersson J.O., H.T., Höglund L., Shi P.F., and Sundman B., *Thermo-Calc and DICTRA - Computational tools for materials science*. Calphad, 2002. **26**: p. 273-312.
55. Larsson, H. and L. Höglund, *Multiphase diffusion simulations in 1D using the DICTRA homogenization model*. CALPHAD: Computer Coupling of Phase Diagrams and Thermochemistry, 2009. **33**(3): p. 495-501.
56. Larsson, H. and A. Engstrom, *A homogenization approach to diffusion simulations applied to + Fe-Cr-Ni diffusion couples*. Acta Materialia, 2006. **54**(9): p. 2431-9.
57. Software, T.-C., *Diffusion Module (DICTRA) Quick Start Guide - Console Mode 2017*, Thermo-CalcSoftware AB.
58. Danninger, H., *Homogenization and Pore Formation During Sintering With Transient Liquid-Phase Powder Metallurgy International*, 1988. **20**(1): p. 21-25.
59. de Oro Calderon, R., et al., *Master alloys for liquid phase sintering: Some key points for the design*. Metal Powder Report, 2016. **71**(3): p. 184-192.
60. B09-04, A.C., *Standard Test Methods for Density of Compacted or Sintered Powder Metallurgy (PM) Products Using Archimedes' Principle; B962-15*. ASTM International.
61. B09, A.C., *Standard Test Method for Transverse Rupture Strength of Powder Metallurgy (PM) Specimens, B528-16*. ASTM International, 2016.
62. UserCom, *Information for Users of Mettler Toledo Thermal Analysis Systems - Interpreting DSC Curves*. 2000.
63. McKinnon, M., *Thermogravimetric Analysis (TGA) & Differential Scanning Calorimetry (DSC)*. 2014.
64. Šalák, A. and M. Selecká, *Effect of manganese content and manganese carrier on properties of sintered and sinter hardened hybrid Fe-3Cr-0.5Mo-xMn-0.24C steel*. Powder Metallurgy, 2008. **51**(4): p. 327-339.
65. Software, T.-C., *Diffusion Module (DICTRA) Documentation Set 2017*, Thermo-CalcSoftware AB.

Appendix A: DICTRA

DICTRA is a software package that can be used for diffusion-controlled transformations in multi-component systems. It is capable of carrying out a variety of simulations that include one-phase simulations, moving boundary problems and cooperative growth.

A sample explanation as to how DICTRA calculates flux in a single-phase system [57]:

Flux of a component k in the z -direction of a system can be given by:

$$J_k = \sum_{i=1}^n L_{ki} \frac{\partial \mu_i}{\partial z}$$

L_{ki} represent a matrix of kinetic coefficients and μ_i is the chemical potential of component i

$$J_k = L_{kk} \frac{\partial \mu_k}{\partial z} = M_k c_k \frac{\partial \mu_k}{\partial z}$$

c_k is the concentration and M_k is the mobility of component k

When combining the flux equation with that of continuity in a planar domain, the local evolution of the concentration of k can be related to the divergence of the flux as such:

$$\frac{\partial c_k}{\partial t} = \frac{\partial}{\partial z} (-J_k)$$

The flux expression can be expanded for concentration gradients:

$$J_k = - \sum_{i=1}^n M_k c_k \frac{\partial \mu_k}{\partial c_j} \frac{\partial c_j}{\partial z} = - \sum_{i=1}^n D_{kj} \frac{\partial c_j}{\partial z}$$

Where the diffusion coefficient of component k with respect to the concentration gradient of component j

$$D_{kj} = -M_k c_k \frac{\partial \mu_k}{\partial c_j}$$

Parameters mentioned in thesis:

Region:

A region is an area of specified thickness or radius that contains at least one phase. Each region can only contain a single matrix (primary) phase. Other phase types include spheroid and lamellar. Spheroid can be used for one or more dispersed phases within a matrix phase while lamellar can be used to simulate the growth of either a eutectic or eutectoid. A sub-region can be used to separate a single region into two parts.

Grid Points:

Each region must contain a specified number of grid points. Compositions are only known at each grid point or "knot."

Grid Type and Spacing:

Depending on the grid type which is selected for the region radius/thickness and number of grid points, a user is able to alter the spacing between points. Options for grid spacing include linear, geometric and double-geometric. As seen in the Figure below, a linear grid entails that all grid points are equidistant. Geometric grids will have grid points that increase in number density toward the left or right of a region. To specify the side of the region that has and double geometric grids, one must enter in a particular "R" value into DICTRA. $R < 1$ will result in a grid with a higher density of points on the right while $R > 1$ will result in a grid with a higher density of points on the left. Double geometric can be used to create a grid with a high density of points in for example, the central area of a region.

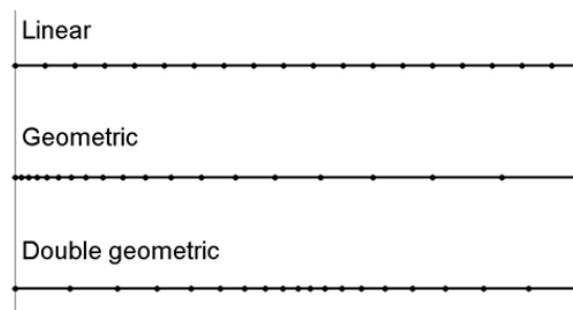


Figure 61: DICTRA Grid Types

Geometry:

DICTRA is solely capable of handling 1-D simulations where composition varies along a single spatial coordinate. The geometry of the system can be selected as planar, cylindrical or spherical. Planar represents an infinitely wide plate of a specified thickness which the user can select. Cylindrical represents an infinitely long cylinder of a specified radius while spherical corresponds to a sphere of a specific radius.

Example:

An example of DICTRA command line to create a region with 2 sub-regions that have a double-geometric grid is summarized below. A corresponding schematic is included at the end of the sample command-line.

DIC>

DIC>enter_grid

REGION NAME : Test-Area

WIDTH OF REGION : 100e-6

TYPE /LINEAR/: sub-region

END COORDINATE IN SUB-REGION: 25e-6

NUMBER OF POINTS : 17

TYPE /LINEAR/: geo

VALUE OF R IN THE GEOMETRICAL SERIE : 0.95

END COORDINATE IN SUB-REGION : 100e-6

NUMBER OF POINTS : 40

TYPE /LINEAR/: geo

VALUE OF R IN THE GEOMETRICAL SERIES : 1.05

DIC>

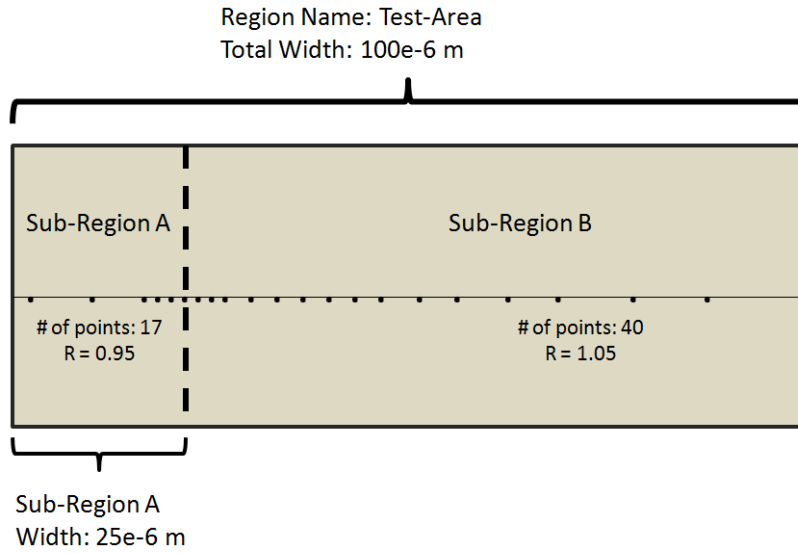


Figure 62: DICTRA Schematic Example

For other variables and parameters that must be specified in a typical DICTRA simulation, one can refer to the DICTRA console guide and documentation set [57], [65].

DICTRA Code Example for Individual Master alloys attached to an iron-carbon particle

go da

tcf6

def_sys

fe cr mn c

rej

PHASES

*

res

ph

bcc liq m23c6 fcc

get

app

mobfe1

def_sys

fe cr mn c

rej

PHASES

*

res

ph

bcc liq m23c6 fcc

get

go d-m

set-cond

GLOBAL

t

0

1553;

N

enter-region

femncrc

enter-grid

FEMNCRC

100e-6

sub-region

10e-6

17

geo

0.95

100e-6

40

geo

1.05

enter-phase

ACTIVE

FEMNCRC

MATRIX

fcc#1

enter-phase

ACTIVE

FEMNCRC

sph

m23c6

enter-phase

ACTIVE

FEMNCRC

sph

liq

enter-phase

ACTIVE

FEMNCRC

sph

bcc#1

enter-comp

FEMNCRC

fcc#1

fe

w-p

cr

function

$(4.5)+(-4.49989)*hs(x-(10e-6));$

c

linear

0.77

0.77

mn

function

$(4.5)+(-4.49989)*hs(x-(10e-6));$

enter-composition

FEMNCRC

liq

y

enter-composition

FEMNCRC

m23c6

y

enter-composition

FEMNCRC

bcc#1

y

s-s-c

1

1

2

yes

ACTIVITIES

no

yes

1

2

NO

YES

NO

ho

y

n

n

y
10000
log
1000
n
n
y
save
set-sim-time
.1
YES
.01
1E-07
1E-07
sim
post
s-d-a
x
dist
GLOBAL
s-d-a
y
w-p
cr
s-p-c
TIME
LAST
plot

Appendix B: Thermo-Calc Diffusivities

Thermo-Calc diffusivities of Mn, Cr, Mo and Ni in FCC-Fe.

Y Axis label: LOGDT (FCC, Alloying Element) = $10\log$ of the tracer diffusion coefficient of an alloying element in FCC-Fe

X Axis label: FUNCTION INVT = Temperature ($1/T$)

MOBFE1: FE, MN
P=1.01325E5, X(MN)=1., N=1.

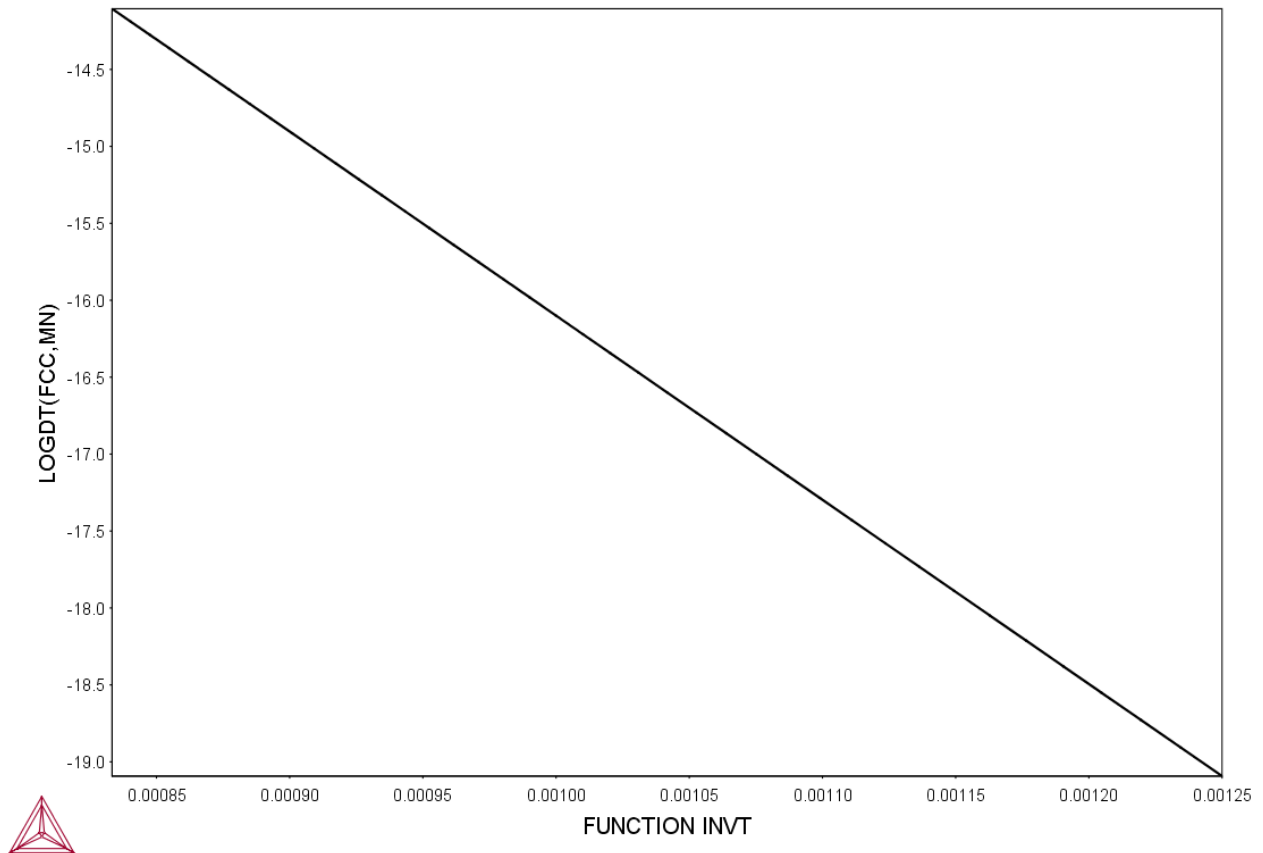


Figure 63: Mn Diffusivity in FCC-Fe

MOBFE1: CR, FE
P=1.01325E5, X(CR)=1., N=1

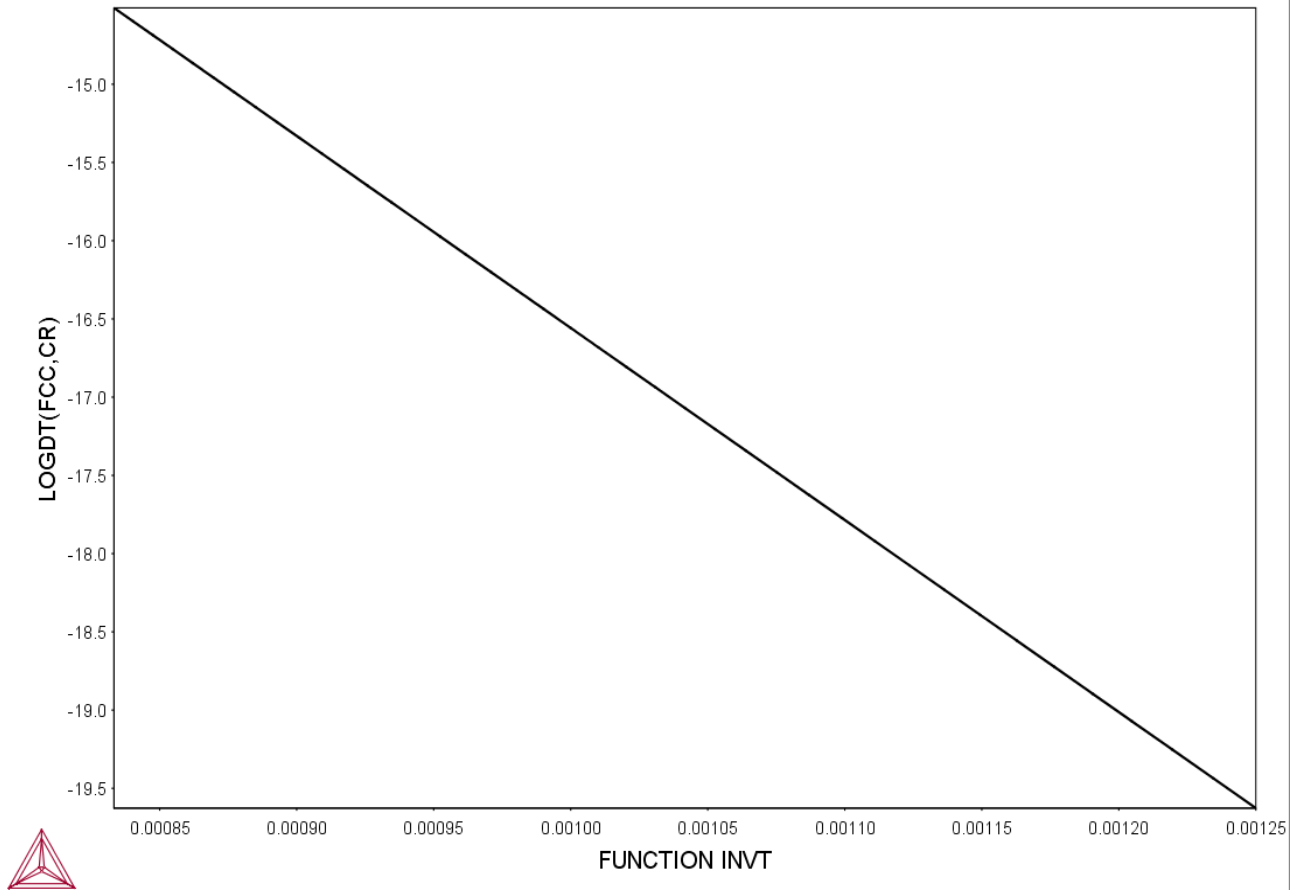


Figure 64: Cr Diffusivity in FCC-Fe

MOBFE1: FE, MO
P=1.01325E5, X(MO)=1., N=1.

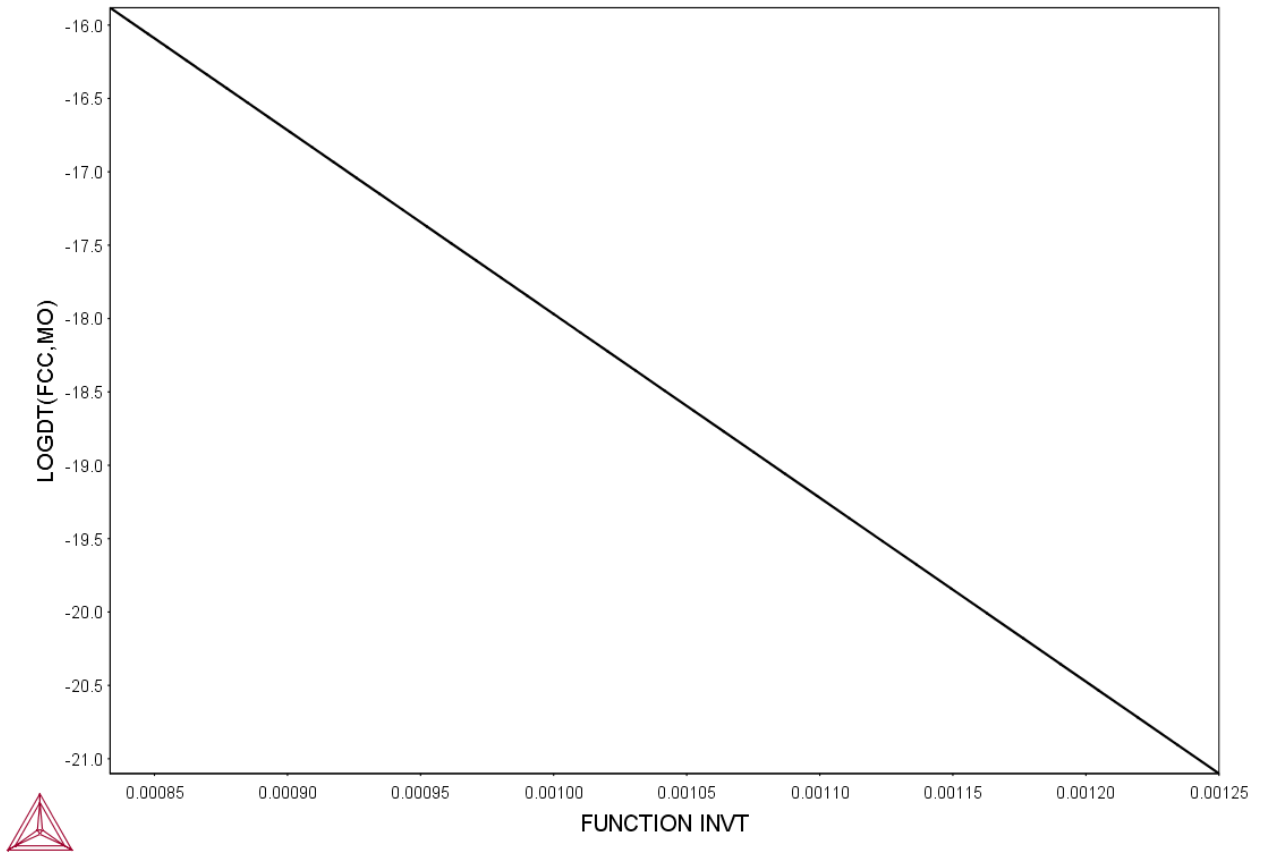


Figure 65: Mo Diffusivity in FCC-Fe

MOBFE1: FE, NI
P=1.01325E5, X(NI)=1., N=1.

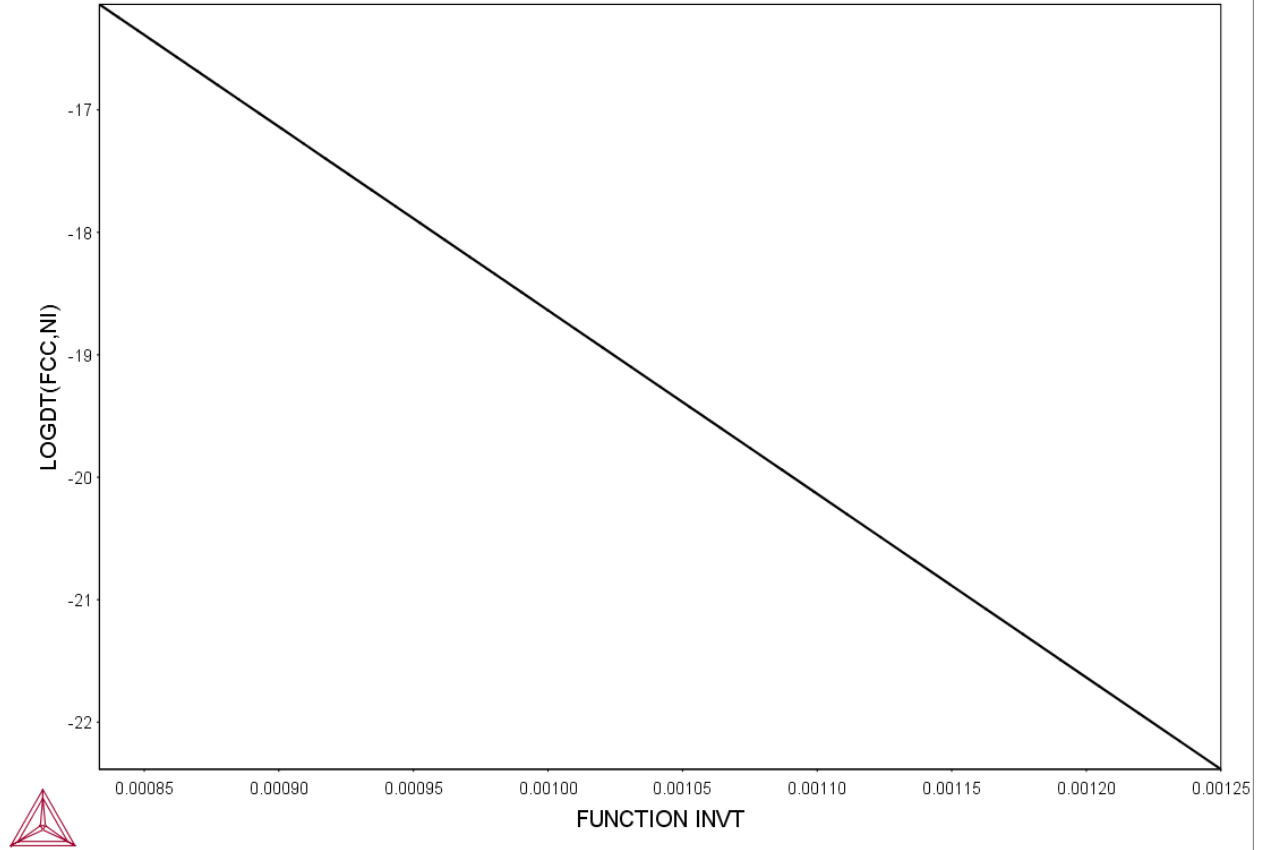


Figure 66: Ni Diffusivity in FCC-Fe